AD-A162 866 GRAIN REFINING AND MICROSTRUCTURAL MODIFICATION DURING SOLIDIFICATION(U) FLORIDA UNIV GAINESVILLE DEPT OF MATERIALS SCIENCE AND ENGINE G J ABBASCHIAN ET AL 1/1

UNCLASSIFIED 25 OCT 85 N00014-81-K-0730 F/G 11/6 NL

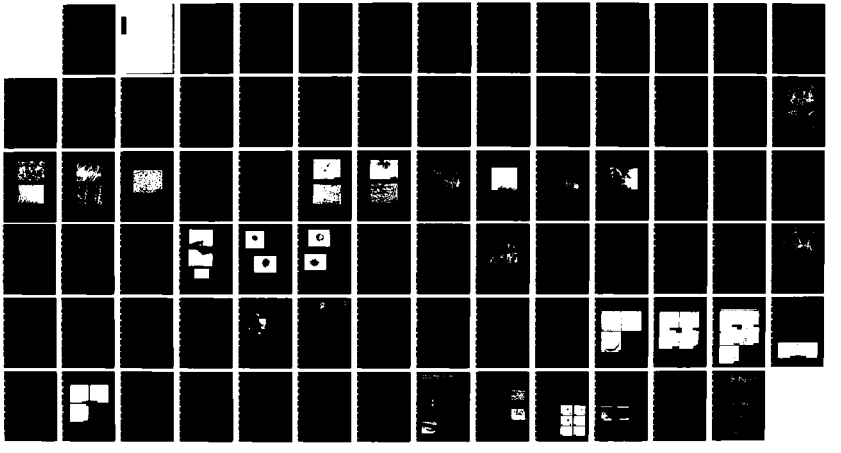

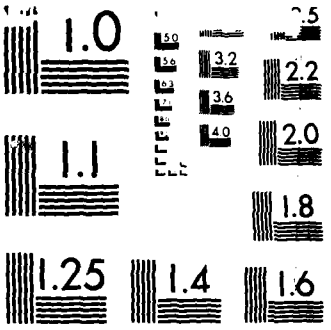

MICROCOPY RESOLUTION TEST CHART
NATIONAL BUREAU OF STANDARDS 1963-A

Unclassified

SECURITY CLASSIFICATION OF THIS PAGE (When Data Entered)

REPORT DOCUMENTATION PAGE

READ INSTRUCTIONS BEFORE COMPLETING FORM

1. REPORT NUMBER: 4	2. GOVT ACCESSION NO.: AD-A162 866
3. RECIPIENT'S CATALOG NUMBER:	
4. TITLE (and Subtitle): Grain Refining and Microstructural Modification During Solidification	5. TYPE OF REPORT & PERIOD COVERED: Annual Report September 1984-August 1985
	6. PERFORMING ORG. REPORT NUMBER:
7. AUTHOR(s): G.J. Abbaschian, J.A. Patchett, R. Russell S.P. Abeln and R. Schmmes	8. CONTRACT OR GRANT NUMBER(s): N00014-81-K-0703-NR031-836
9. PERFORMING ORGANIZATION NAME AND ADDRESS: Materials Science and Engineering University of Florida Gainesville, FL 32611	10. PROGRAM ELEMENT, PROJECT, TASK AREA & WORK UNIT NUMBERS:
11. CONTROLLING OFFICE NAME AND ADDRESS: Office of Naval Research-Materials Division 800 North Quincy Street Arlington, VA 22217	12. REPORT DATE: October 25, 1985
	13. NUMBER OF PAGES: 78
14. MONITORING AGENCY NAME & ADDRESS(if different from Controlling Office):	15. SECURITY CLASS. (of this report): Unclassified
	15a. DECLASSIFICATION/DOWNGRADING SCHEDULE:

16. DISTRIBUTION STATEMENT (of this Report)

Approved for public release; distribution unlimited. Reproduction in whole or in part is permitted for any purpose of the United States government.

17. DISTRIBUTION STATEMENT (of the abstract entered in Block 20, if different from Report)

18. SUPPLEMENTARY NOTES

19. KEY WORDS (Continue on reverse side if necessary and identify by block number)

Grain refining, microstructure, solidification, phase diagrams, electromagnetic stirring, Cu-Fe alloys, Cr-Ni alloys, Ar-Ni alloys, and Al-Li-Mg-Zr alloys.

20. ABSTRACT (Continue on reverse side if necessary and identify by block number)

This report summarizes progress during the 1984-1985 fiscal year of a research program to study grain refining and microstructural modification during solidification, as affected by supercooling, solidification rate and/or innoculation. The report covers results of the current investigations on the kinetics of peritectic reactions during solidification of binary Al-Ni alloys, and high termperature phase transformations in binary Cr-Ni alloys. In addition, the report contains

DD FORM 1 JAN 73 1473 EDITION OF 1 NOV 65 IS OBSOLETE S/N 0102-014-6601

Unclassified

SECURITY CLASSIFICATION OF THIS PAGE (When Data Entered)

results of three other completed projects related to grain refining in Cu-Fe alloys, thermomechanical processing of rapidly solidified Al-Li-Mg-Zr alloy powder, and purification of Nb by electromagnetic levitation melting.

TABLE OF CONTENTS

I. Abstract

This report summarizes progress during the 1984-85 fiscal year of a research program to study grain refining and microstructural modifications during solidification, as affected by supercooling, solidification rate, and/or innoculation. The report covers results of the current investigations on the kinetics of peritectic reactions during solidification of binary Al-Ni alloys, and high temperature phase transformations in binary Cr-Ni alloys. In addition, the report contains results of three other completed projects related to grain refining in Cu-Fe alloys, thermomechanical processing of rapidly solidified Al-Li-Mg-Zr alloy powder, and purification of Nb by electromagnetic levitation melting.

II. KINETICS OF PERITECTIC REACTIONS IN AL-NI

Peritectic reactions play an important role in determining structure and properties of many commercial alloys. In spite of the fact that peritectic reductions occur as frequently as eutectics, they have received less attention than the eutectic reactions. This is in part due to the complexity of the peritectic reaction; a peritectic reaction involves dissolution and growth, whereas a eutectic reaction involves only growth. Another difficulty in studying peritectic reactions is due to the fact that the nucleation behavior of the peritectic phase is affected not only by the thermal conditions but also by the amount, morphology, and nucleation potency of the primary (properitectic) phase. If the peritectic phase is not easily nucleated on the properitectic phase, the latter may continue to grow and suppress the peritectic reaction to lower temperatures. If, on the other hand, growth of the primary phase is incomplete, which might be the case during rapid solidification or solidification of facet forming intermetallics, the nucleation of the second phase could occur at a composition and a temperature different than the equilibrium. An example of this type of behavior is found in the Al-Ti system [1].

The major goal of this program, therefore, is to study the microstructure, volume fractions and compositions of peritectic alloys as a function of cooling rate and surface area of the properitectic phase. The peritectic systems currently being studied involve $NiAl_3$, Ni_2Al_3, and NiAl intermetallics by the following reactions:

$$\text{Liquid} \longrightarrow NiAl$$

$$\text{Liquid} + NiAl \longrightarrow Ni_2Al_3$$

$$\text{Liquid} + Ni_2Al_3 \longrightarrow NiAl_3$$

The phase diagram for the system is shown in Figure 1 [2]. NiAl phase has an ordered BCC (CsCl type) structure, whereas Ni_2Al_3 has a hexagonal structure, which can be formed by introducing and ordering of vacancies in the BCC lattice. $NiAl_3$, on the other hand, has an orthorhombic structure of Fe_3C type.

Experimental Procedure

Samples with nominal compositions of 30, 35, 39.6 or 42 wt.% Ni, each weighing about one gram, were prepared from 99.999% pure Ni and 99.999% pure Al by arc melting in an inert atmosphere on a water cooled copper hearth. The inert atmosphere consisted of titanium "gettered" helium and argon. Each sample was then levitated in an inert atmosphere in an electromagnetic levitation apparatus described previously [3]. In order to achieve different cooling rates and surface area of the primary phase, the samples were solidified by one of the following techniques:

a) The levitated samples were solidified at the levitated state by increasing the gas flow rate, or by dropping in water or molten Pb-Sn-Bi eutectic held at 96°C. Some samples were also dropped in a copper cup rotating at 30,000 rpm, or were splat cooled in a hammer-anvil type splat cooling device.

b) The levitated and molten samples were cooled to about 40°C above the peritectic temperature (855°C). The primary solid plus liquid was held at this temperature for a period up to 7 minutes, then quenched through the peritectic transformations by one of the above mentioned techniques.

The cooling rates in the samples were determined by constructing a dendrite arm spacing versus cooling rate master curve. To achieve this, an ingot with a water-cooled copper chill was prepared with thermocouples

positioned at 1, 10, 20, and 40 mm from the chilled surface. After solidification, the ingot was sectioned, polished and the dendrite arm spacings were determined at the location of thermocouples. The cooling rate was determined from the slope of the output of the thermocouples versus time.

The microstructure of the as-quenched samples were analyzed using optical microscopy and SEM. The volume fractions of Ni_2Al_3, $NiAl_3$, and $NiAl_3$ + Al eutectic were determined by an image analyzer interfaced to the SEM operating in the backscattered mode. The volume fractions determined from the image analyzer were also checked by using a quantitative x-ray diffraction technique of the powdered samples. The x-ray technique adopted in this work is based on the method of "direct comparison" where the volume fraction of each phase is determined by comparing the ratio of the integrated intensities to those of standard samples [4]. The standard samples were prepared by annealing known compositions at 600°C for 336 hours. The curves relating the ratio of the corrected integrated intensities to the $Ni_2Al_3/NiAl_3$ and $Al/NiAl_3$ ratios in the standard samples are shown in Figures 2 and 3, respectively. These curves were utilized to determine the volume fractions in the as-quenched samples.

Results

Cooling Rate Determinations

The dendrite arm spacings for both the primary and peritectic phases versus cooling rate are shown in Figure 4. The equations correlating the secondary arm spacing to the cooling rate for these phases were determined to be:

$$DAS = 76\varepsilon^{-0.37}$$

$$DAS = 23\varepsilon^{-0.13}$$

where DAS is the arm spacing in μm, and ε is the cooling rate in °C/s. As can be seen, the peritectic phase does not lie on the same line as the primary phase. The reason for this is that in the case of primary Ni_2Al_3 the dendrite arm spacing is governed by the morphological instability of the interface behind the dendrite tip and subsequent coarsenings of the arms. The spacing of the peritectic dendrites, on the other hand, depends, in addition to the above mentioned factors, on the nucleation kinetics of the peritectic phase on the primary arms. The present arm spacings versus the cooling rate results generally agree well with those of the previous investigators [5,6]. They, however, have not distinguished the difference between the primary and peritectic spacings.

The measured dendrite arm spacing of each sample and Figure 4 were used to determine the cooling rate during solidification. In general, the cooling rate during solidification of the levitated samples by passing He gas was in the range up to 30°C/s. The cooling rates were in the range 4×10^2 to 6×10^2, and 5×10^3 to 8×10^3 °C/s for water quenched and molten Pb-Sn-Bi quenched samples, respectively. For the samples solidified in the rotating cup the cooling rate ranged from 10^3 to 10^4 °C/s, depending on the sample thickness, and for splat cooled samples from 10^5 to 10^6 °C/s.

Microstructures

A typical microstructure of a 42 wt.% Ni sample solidified using helium gas is illustrated in Figure 5, where three phases can be identified; the light colored Ni_2Al_3 primary phase is surrounded by the faceted $NiAl_3$ phase followed by the dark regions corresponding to the Al-$NiAl_3$ eutectic. The effect of cooling rate on the microstructure can be seen in Figures 6, 7 and 8 for three samples solidified at 5×10^2, 5×10^3 and 10^6 °C/sec, respectively.

It can be seen that in this alloy, despite the high rate of cooling, the faceted $NiAl_3$ still forms peritectically on Ni_2Al_3 and there is no evidence of independent nucleation of the $NiAl_3$. The higher cooling rates, however, reduce the amount of the primary phase with a corresponding increase in the amount of the peritectic phase. The volume fractions of the constituent phases at the various cooling rates determined by the image analysis are summarized in Figure 9. As the cooling rate increases, the reduction in the volume fraction of the primary phase is balanced by the increase in the secondary phase, and the amount of eutectic remains approximately constant.

Figure 10 compares the volume fractions determined by x-ray analysis to those of the image analysis. Considering just the Ni_2Al_3 and $NiAl_3$ phases, the agreement between the two measuring techniques is very good. The data points fall on a 45 degree line slightly offset from the origin. The offset is such that when the image analyzed sample indicates zero volume fraction, the x-ray analysis would suggest approximately 4.5 percent of material present. The discrepancy can be traced to the inability of image analysis technique to distinguish between porosity and eutectic structure. This in turn also explains the poor correlation of the aluminum content measurements since all the porosity, and hence the error, is associated with this phase.

The reduction of the primary phase content by increasing the cooling rate can be seen more clearly in Figures 11-13 for 30 wt.% Ni samples. The slowly cooled sample, Figure 11, contains approximately 14% Ni_2Al_3 as compared with approximately 6% in the water quenched sample shown in Figure 12. The primary phase completely disappears, as shown in Figure 12, when the cooling rate is further increased by quenching in molten Pb-Sn-Bi eutectic. The cooling rate necessary to completely suppress the formation of the primary Ni_2Al_3 depends on the composition of the alloy. The higher the nickel content, the larger is the required cooling rate. For example, with a composition of 35.6 wt.%, the

cooling rate during solidification in the rotating copper cup is insufficient to suppress the formation of the primary, as shown in Figure 14. However, increasing the cooling rate by solidifying in the splat cooling device completely suppresses the primary phase formation in this alloy. The absence of Ni_2Al_3 in this sample was also confirmed by x-ray analysis which detected only the presence of aluminum and $NiAl_3$. Increasing the composition to 39.6 wt.% Ni, on the other hand, results in the reappearance of the Ni_2Al_3 phase even in the splat cooled samples.

Surface Area Effects

Photomicrographs in Figure 15 and 16 show the effects of holding time at 890°C on the shape and particle size of the primary phase. As the holding time increases, the primary Ni_2Al_3 phase particles coarsen and become rounded. Some particles also coalesce, as shown in Figure 16. The surface area of the primary phase per unit volume of the sample decreases from 0.068 to 0.047 $\mu m^2/\mu m^3$ as the holding time increases from 1/2 to 5 minutes. It should be noted that the isothermal holding not only produces different surface areas, but also increases the volume fraction of the primary phase.

The influence of surface area of the primary phase on the amount of peritectic phase is illustrated in Figure 17 for samples cooled at approximately 5000°C/sec. To take into account differences in the volume fraction of the primary, the volume fraction of the peritectically formed $NiAl_3$ was normalized with respect to the volume fraction of liquid remaining after solidification of the primary. The normalized volume fraction of the second phase is plotted versus the surface area of the primary phase in Figure 18. For surface areas less than 0.07 $\mu m^2/\mu m^3$, Figures 17 and 18 show that a change of only 0.015 $\mu m^2/\mu m^3$ in the surface area of the primary phase is

sufficient to almost double the amount of peritectically formed $NiAl_3$. This indicates the strong effect of nucleation kinetics on the amount of the peritectic phase.

The effect of quenching medium on the normalized second phase content is shown in Figure 19 for surface areas less than 0.10 $\mu m^2/\mu m^3$ for samples quenched from the primary solid plus liquid region. It is important to note that in addition to the holding time, the quenching media is influencing the surface area of the primary phase. This is due to the effect of fluid flow during solidification from 890°C to the eutectic temperature on the existing solid particles. Our recent experiments on binary Cu-Fe alloys (see section IV of this report) have demonstrated the ability of fluid flow to break up the dendrite arms providing grain refinement. The dendrite fragmentation also manifests itself by an increase in the surface area of the primary phase. In the case of the water quenched samples, the interaction between the molten aluminum-nickel and the water has apparently provided vigorous stirring, and considerable dendrite fragmentation. The surface area of the Pb-Sn-Bi quenched samples is comparable but slightly less than that of the helium quenched samples.

Figure 20 plots the volume fraction of the peritectically formed $NiAl_3$ to the surface area of the primary phase for samples quenched from completely liquid at cooling rates of 5×10^3, 10^4, and 10^5 °C/sec. Normalizing the volume fraction measurements, Figure 21, shows insensitivity of the normalized volume fraction to the surface area of the primary phase.

Combining the normalized volume fractions versus surface area measurements for the Pb-Sn-Bi quenched samples (Figure 18) and those quenched from the completely liquid state (Figure 21) produces Figure 22, which shows the influence of surface area over a range of 0.03 to 0.9 $\mu m^2/\mu m^3$. From this figure, two regions can be described: At surface areas less than 0.07

$\mu m^2/\mu m^3$, a small change in the surface area produces a very drastic increase in the amount of second phase material indicating that nucleation of the peritectic phase in dominating the peritectic reaction. At higher surface areas the normalized amount of the peritectic phase becomes almost independent of the surface area. In this region the growth rates are dominating the formation of $NiAl_3$. A theoretical model is being developed to predict the extent of the peritectic reactions from the nucleation and growth kinetics.

Electron Microscopy

Transmission electron microscopy was used to investigate the $Ni_2Al_3/NiAl_3$ interface and determine the possible orientation relationships between the primary and the peritectic phases. Interference fringes were imaged under two beam conditions in bright and dark fields, as shown in Figure 23. The spacing of the fringes was measured to be approximately 154 Å. As can be seen, the fringes are symmetric in the bright field mode, (i.e., there are an even number of light and dark bands) while in the dark field mode they are asymmetric. This arrangement of fringes is typical of delta boundaries, indicating good atomic matching at the interface and the existence of stacking faults. Within the fringes, dislocations produced by the mismatch of the two crystal lattices normally should be visible. In these samples, however, interface dislocations were not found and attempts to image the dislocations in different diffracting conditions were also unsuccessful.

The closest matching at the boundary was found for the conditions of the $[0\bar{1}2]$ zone axis of $NiAl_3$ being 3 degrees from the $[\bar{4}041]$ zone axis of Ni_2Al_3. Figure 24 gives the $[0\bar{1}2]$ zone axis of the $NiAl_3$ and the corresponding diffraction pattern of the Ni_2Al_3 showing the slight misconfiguration of the zone axis. A tilt of approximately 3 degrees,

shown in Figure 25, brings the Ni_2Al_3 to its [$\bar{4}041$] zone axis and moves the $NiAl_3$ slightly off its zone axis. This suggests that complete epitaxial matching is not occurring at the interface but the misorientation between the crystal lattices is not large.

III. High Temperature Phase Transformation in Cr-Ni Alloys

The results of our current investigations during solidification of high purity Cr-Ni alloys indicate that the commonly accepted simple eutectic diagram of the binary system is incorrect. Microstructural results of samples solidified in an inert gas containing very low oxygen of about 10^{-15} ppm indicate the existence of an additional peritectic transformation in the range of 60 to 70% Cr. The peritectic temperature has been determined by a two-color pyrometer to be around 1445°C. The preliminary results of this project were published in the MRS Proceedings 1984 (see Appendix A), and another paper is now being prepared for publication. The summary of some of the current results is given below.

Thermal arrest points obtained during non-equilibrium solidification of 12 samples in the composition range 51 to 75 wt.% Cr are shown in Table 1. The data, which agree well with the previous results given in Appendix A, have been superimposed on the currently accepted simple eutectic diagram [7] and the diagram proposed by Yukawa et al. [8] in Figures 26 and 27, respectively. The highest thermal arrest point of each sample corresponds to the liquidus temperature, while the other arrest points correspond to some form of liquid to solid or solid state transformation. The alloys containing 51 and 60 wt.% Cr show only two thermal arrest points; one belonging to the liquidus and the other to the eutectic temperature where the last liquid solidifies. When the chromium content of the alloy is 62 wt.% or higher, additional arrest points

are observed above the eutectic temperature. Microstructure of the quenched samples indicates the existence of a peritectic transformation when the alloys contain more than 62 wt.% Cr, see Figure 28. The peritectic temperature lies between the liquidus temperature of alloys with 60 and 62 wt.% Cr, i.e., between 1445 to 1458°C. These findings, combined with our previous results, place the peritectic temperature at 1445 $\pm$ 26°C. The peritectic liquid composition is in the range 60 to 62 wt.% Cr. STEM analysis of the quenched samples indicates the composition of the peritectic phases from 60 to 70 wt.%. Other features of the diagram or the exact phase boundaries are yet to be determined.

Attempts to preserve the high temperature phases by various rapid solidification techniques have not been successful so far, as the phases go rapidly through solid state phase transformations and/or precipitation. We are currently utilizing a high temperature x-ray diffraction camera to determine the crystalline structure of the high temperature phases in the alloys. The x-ray unit, capable of heating the samples to 2200°C using a Ta strip heater, can be operated in vacuum or inert atmosphere.

Diffraction patterns of samples containing 51 wt.% Cr quenched from the liquid state shows the presence of only α-Cr and γ-Ni phases. The lattice parameters of the phases are 2.89 and 3.62 Å, respectively, indicating that both phases are supersaturated. When these samples are heated to around 1000°C, extra peaks appear that do not belong to α-Cr or γ-Ni. The extra peaks, however, disappear when the sample is held at 1300°C for approximately 2 hours, leaving only α-Cr and γ-Ni peaks. Figures 29 and 30 show an x-ray scan of the 51 wt.% Cr sample after holding at 1300°C for 20 minutes and for 2 hours, and Table 2 summarizes the x-ray data for the sample. The table also includes d scapings of the σ phase given by Yukawa [8] and β phase given by Grigor'ev et al. [9]. The latter investigators indicate five allotropes of

Grigor'ev et al. [9]. The latter investigators indicate five allotropes of chromium as:

$$(\overset{\alpha}{BCC}) \xrightarrow[930]{} (\overset{\beta}{FCC}) \xrightarrow[1300]{} (\overset{\gamma}{BCC}) \xrightarrow[1650]{} (\overset{\delta}{HCP}) \xrightarrow[1830°C]{} (\overset{\varepsilon}{BCC})$$

They have proposed a phase diagram which contains four eutectoids in addition to the eutectic transformation. The extra peaks agree very well with those given by Yukawa for σ phase. However, based on Yukawa's diagram, the σ phase should form around 1200°C, and should be stable as temperature is increased. Our results show that they form around 1000°C and disappear at 1300°C.

At this time it is not clear whether the extra peaks truly represent the σ phase of Yukawa or some form of allotropic transformation similar to that of Grigor'ev. It should also be noted that the peaks may also belong to a defective oxide layer forming on the surface of the samples. This is conceivable because at 10^{-15} ppm partial pressure of oxygen, thermodynamic possibility of some chromium oxide formation at low temperatures exists. When the temperature exceeds a certain limit, the oxides may become thermodynamically unstable and therefore disappear. It is also possible that with the prolonged heating, some oxygen is diffusing into the bulk sample, causing the σ phase to dissolve.

Current efforts are concentrated in further reducing the oxygen content in the system. Experiments are also being conducted to melt the eutectic alloy in situ in the x-ray camera, and investigate the formation of the peritectic phase during solidification. The existence of phase changes in pure chromium is also being investigated.

IV. Grain Refining of Copper by the Addition of Iron and by Electromagnetic Stirring

This research, which was initiated earlier in our program, shows that the addition of iron at concentrations as low as 0.57 wt.% causes considerable grain refinement in Cu, and the average grain size decreases with increasing the iron content in water quenched samples. Electromagnetic stirring, on the other hand, has beneficial effect on refining of the grains only when the iron content is less than 2.8 wt.%. This composition corresponds to that of the peritectic liquid. Beyond this composition, electromagnetic stirring has a detrimental effect because it agglomerates the primary iron particles which act as heterogeneous nucleation sites for the copper matrix.

The experiments clearly show that, contrary to the commonly accepted wisdom, the usefulness of fluid flow in refining the microstructure strongly depends on the alloy composition and the nature of solid-liquid transformation. A paper based on this work, given in Appendix B, was published in the Metallurgical Transactions.

V. Thermomechanical Processing of Rapidly Solidified Al-Li-Mg-Zr Alloy Powder

In this spin-off project, rapidly solidified Al-3% Li-5.5% Mg-0.2% Zr powder was hot extruded in vacuum, and subjected to the conventional precipitation heat treatment, as well as to a novel thermomechanical processing technique. The process consists of cryogenic rolling of the solutionized alloy followed by precipitation heat treatment above the δ' solvus. The process results in the formation of homogeneously distributed fine δ particles, rather than δ' particles which are produced by conventional strengthening techniques. The formability, ductility and toughness of the alloy is greatly improved by the cryogenic process. A paper based on this

work, see Appendix C, is to be published by TMS-AIME in the Proceedings of the Symposium on Mechanical Behavior of Rapidly Solidified Materials.

VI. Refining of Niobium by Levitation Melting Technique

In this project, conducted in cooperation with Cabot Corporation, the refining behavior of niobium, produced by an aluminothermic reduction reaction of Nb_2O_5, was studied using the electromagnetic levitation and melting technique. The purification of niobium thermite takes place by the vaporization of impurity, the extent of which depends on the residence time at the levitated state. For example, the purity of the material was improved from 93-95% to 99.96% after melting for about 7 minutes in high purity argon. A paper based on this paper, see Appendix D, was published in the Journal of Metals.

VII. References

1. H. W. Kerr, J. Cisse and G. F. Bolling, Acta Metall., Vol. 22, 1974, 667-686.

2. Metals Handbook, Volume 8, 8th edition, American Society for Metals, 1973, 262.

3. G. J. Abbaschian, Technical Report No. 1, Contract N00014-81-K-0730, Office of Naval Research, October, 1982.

4. J. S. Sarreal, Masters Thesis, University of Florida, May 1985.

5. C. S. Brooks, F. D. Lemkey and G. S. Golden, "In Rapidly Solidified Amorphous and Crystalline Alloys," B. H. Kear, B. C. Giessen and M. Cohen, Eds., Elsevier Press, New York, 1982, 397-407.

6. E. C. Ethridge, P. A. Curreri, and M. Kelly, NASA Technical Memorandum, TM-86473, October, 1984.

7. P. Nash, "The Cr-Ni (Chromium-Nickel) System," Submitted for publication to The Bulletin of Alloy Phase Diagrams.

8. N. Yukawa, M. Hida, T. Imura, M. Kawamura and Y. Mizuno, "Structure of Chromium-Rich Cr-Ni, Cr-Fe, Cr-Co, and Cr-Ni-Fe Alloy Particles Made by Evaporation in Argon," Met. Trans., April, 1972, Vol. 3, p. 887-895.

9. A. T. Grigor'ev, E. M. Sokolovskaya, N. A. Nedumov, M. V. Maskimova, L. G. Sokolova, and Yeh Yu-pu, "Polymorphic Changes in Chromium: The Phase Diagram of the Chromium-Nickel System in the Chromium-Rich Region," Russian J. of Inorganic Chemistry, Sept. 1960, Vol. 5, No. 9, p. 1036.

Table 1

Thermal Arrest Data

wt.% Cr	# of Samples	Liquidus	Additional Arrests		
90	1	1754 ± 0	-----		
80	1	1664 ± 0	-----		
75	2	1608 ± 6	1448(1)	1375(1)	
67.5	2	1523 ± 0	1488±8(2)	1436±4(2)	1358±9(2)
65	2	1499 ± 10	1416±8(2)	1380±4(2)	1350±5(2)
62	3	1458 ± 3	1391 (1)	1360±0(2)	
60	2	1445 ± 0	1345 (1)		
51	1	1375	1345 (1)		

( ) - Numbers in parentheses represent the number of samples which exhibited that particular arrest.

Note: All temperatures are in degrees C.

Table 2

X-Ray Data for 51 Wt.% Cr, Compared With Those of Yukawa [8] and Grigor'ev [9]*

51 wt.% Cr Room Temperature	51 wt.% Cr after 20 Minutes at 1300°C	Yukawa[8] σ-Phase	Grigor'ev[9] β-Phase
	2.366		
2.259**	2.269**	2.29	
	2.168	2.152	2.177
2.057 γ(111)	2.084 γ(111)	2.090	
		2.047	
2.020 α(110)	2.043 α(110)	2.037	
1.963**	1.977**	1.984	
		1.945	
		1.897	
	1.879	1.870	1.886
1.792 γ(200)	1.812 γ(200)		
	1.800		
	1.775	1.774	

* All d-spacings are in Angstroms

** Platinum substrate peaks

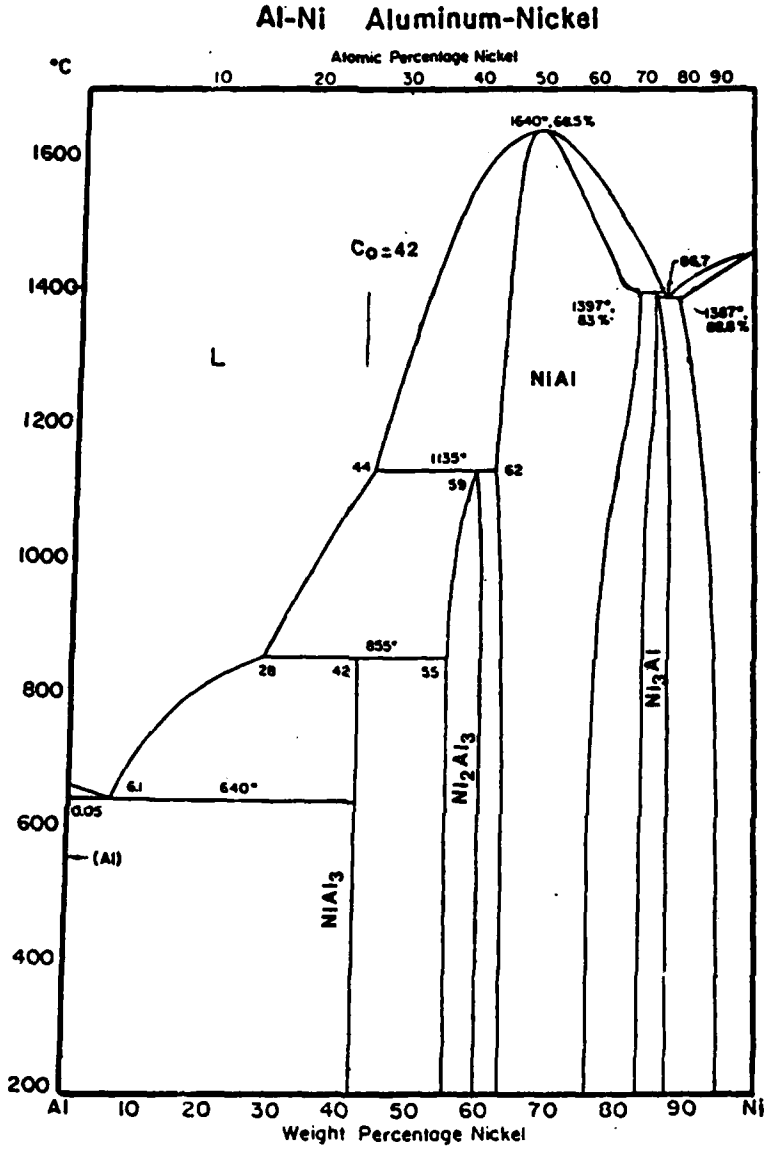

Figure 1. Aluminum-Nickel phase diagram [2].

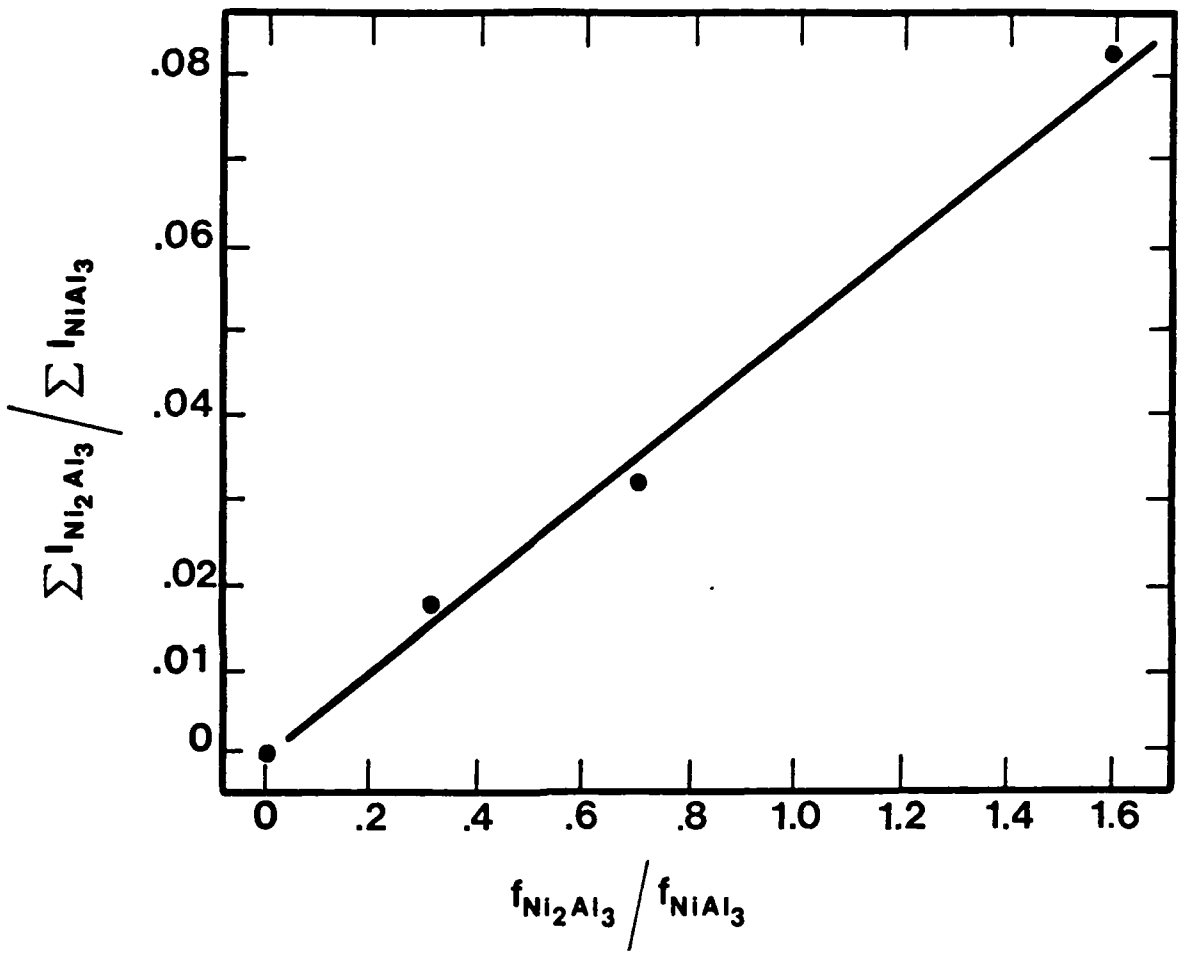

Figure 2. Standard curve relating the measured ratio of the integrated intensities to the ratio of volume fractions of Ni_2Al_3 and $NiAl_3$.

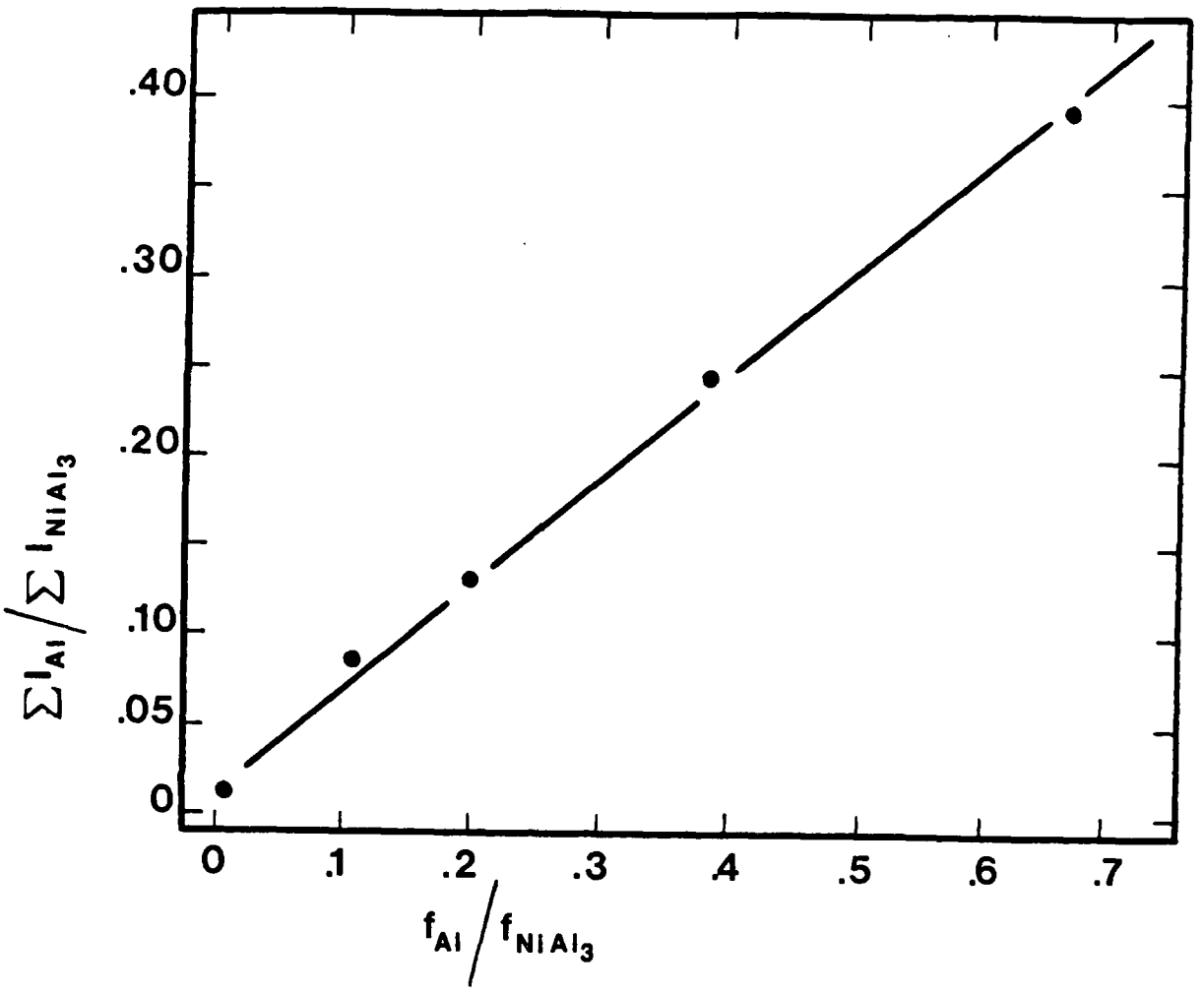

Figure 3. Standard curve relating the measured ratio of integrated intensities to the calculated ratio of volume fractions for Al-$NiAl_3$.

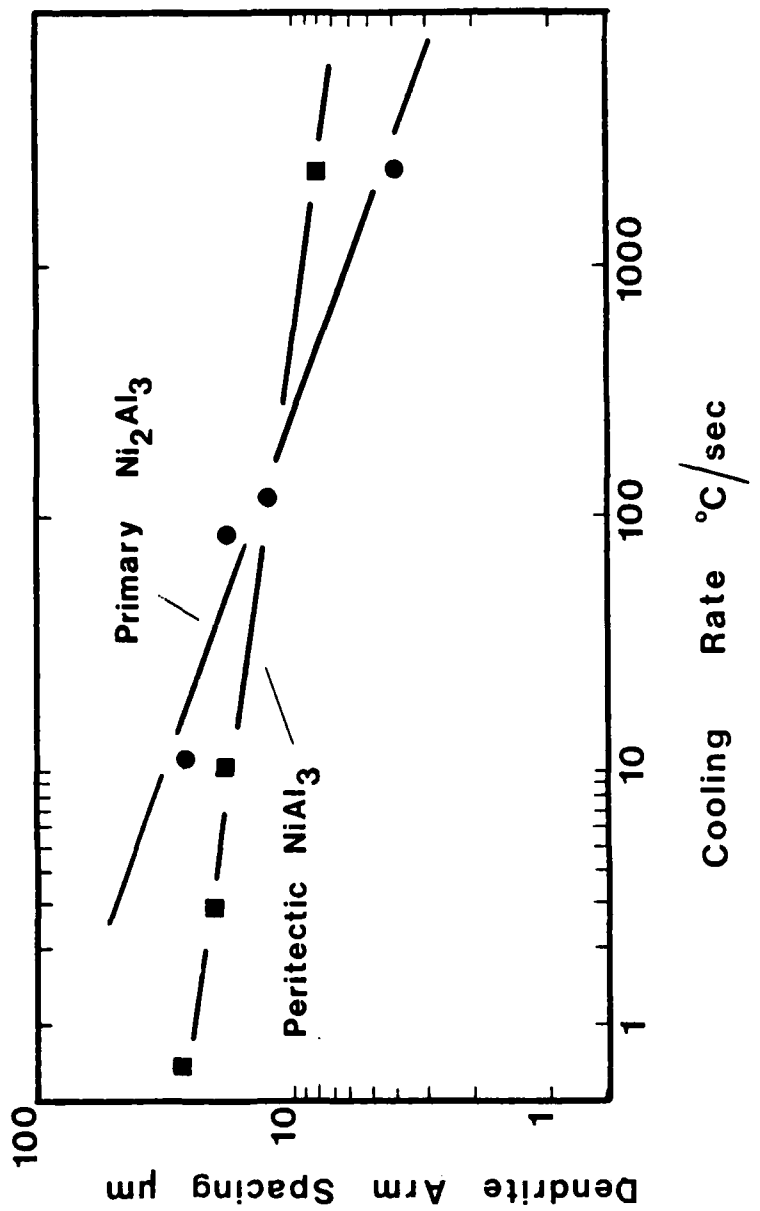

Figure 4. Dendrite arm spacing versus cooling rate.

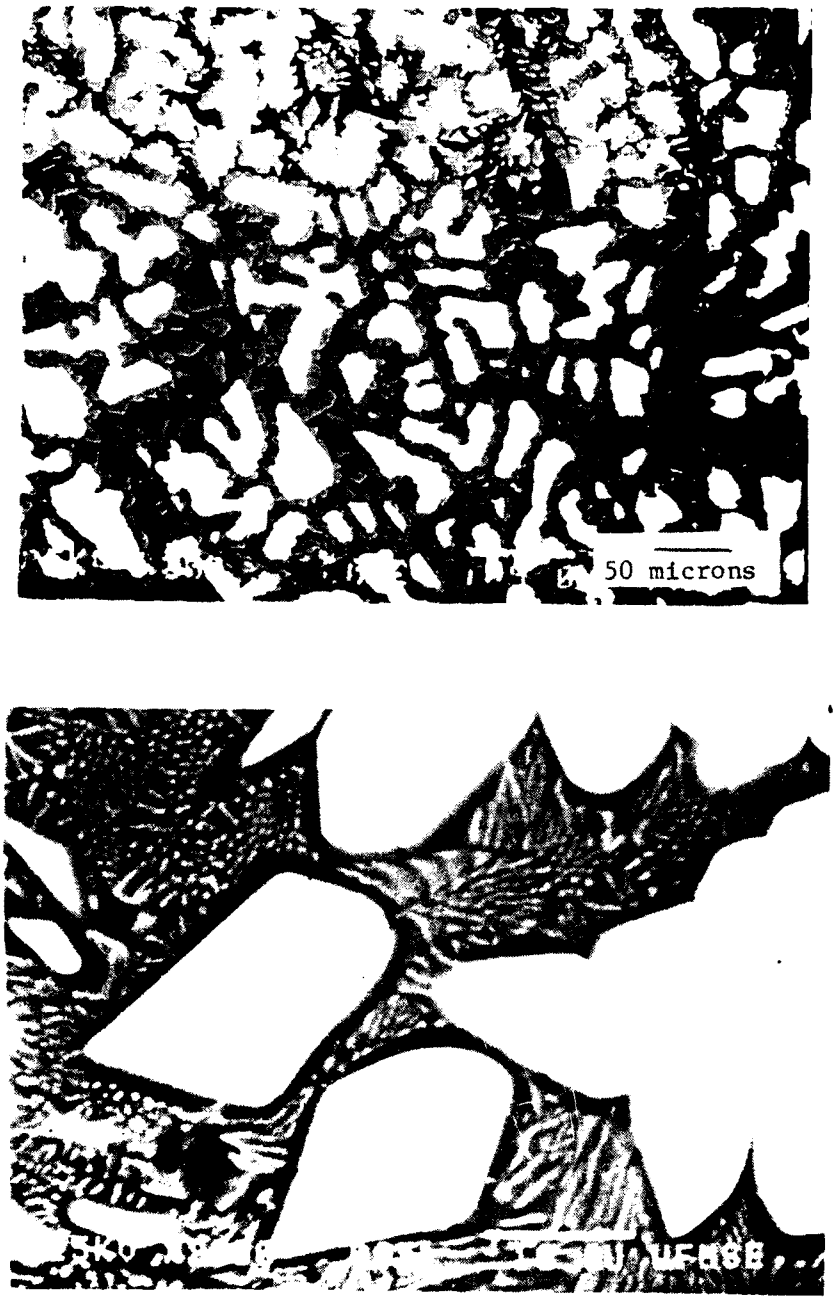

Figure 5. A typical microstructure of Al-42 wt.% Ni, showing Al_2Ni_3, Al_3Ni and eutectic.

Figure 6. Microstructure of Al-42 wt.% Ni water quenched from liquid.

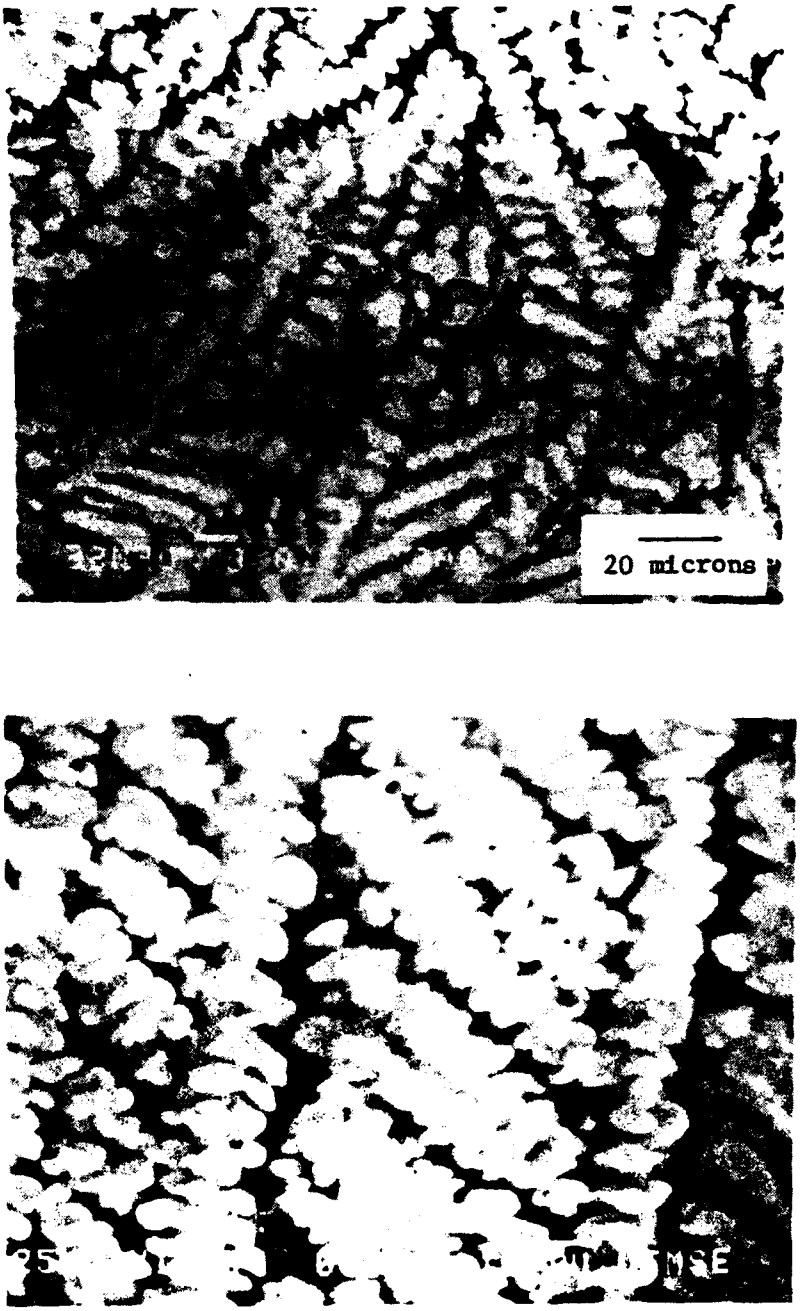

Figure 7. Microstructure of Al-42 wt.% Ni quenched into molten Pb-Sn-Bi eutectic from liquid.

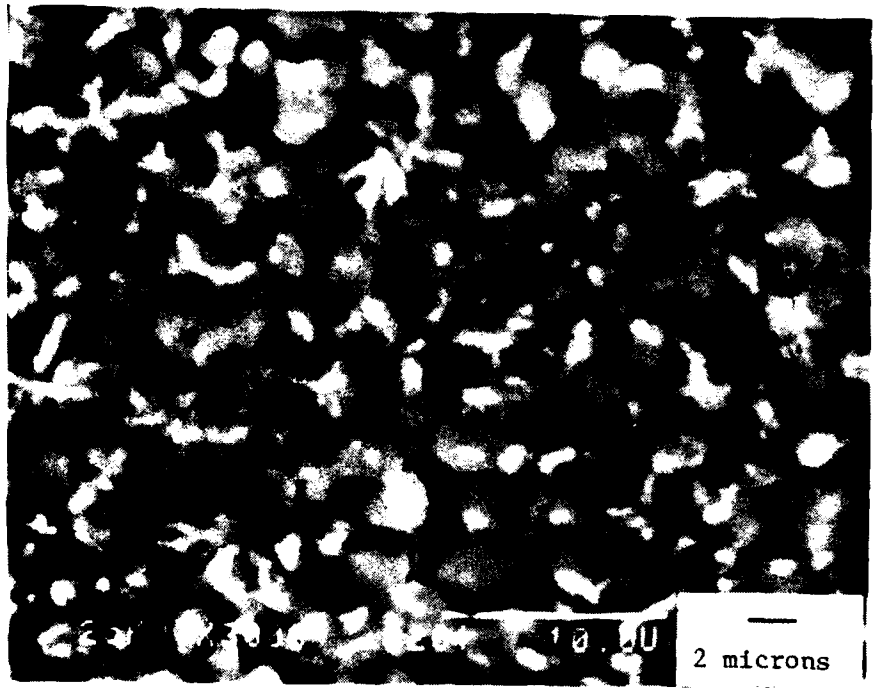

Figure 8. Microstructure of Al-42 wt.% Ni splat cooled from liquid.

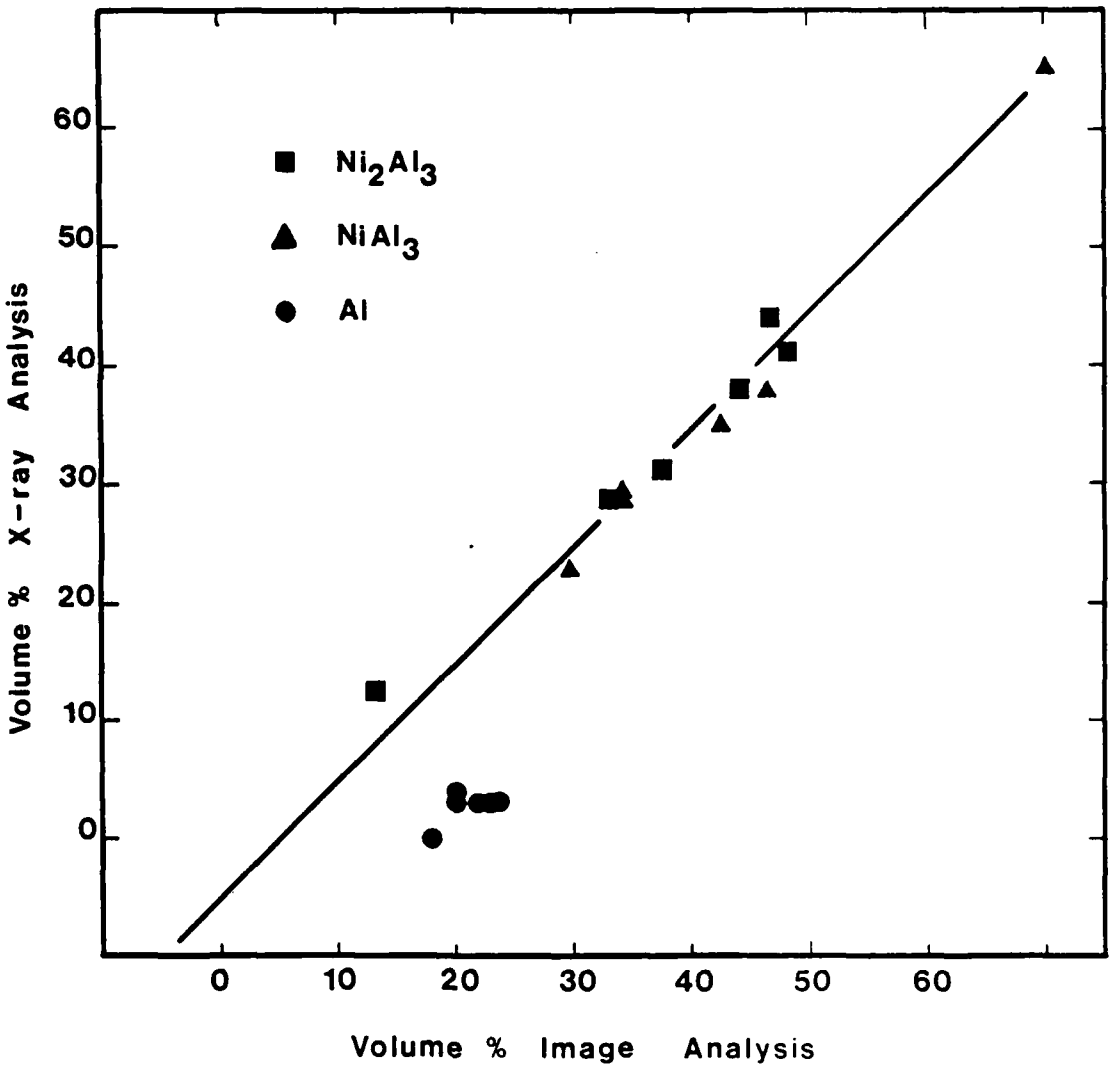

Figure 9. The correlation between the volume fractions determined by the x-ray and image analysis.

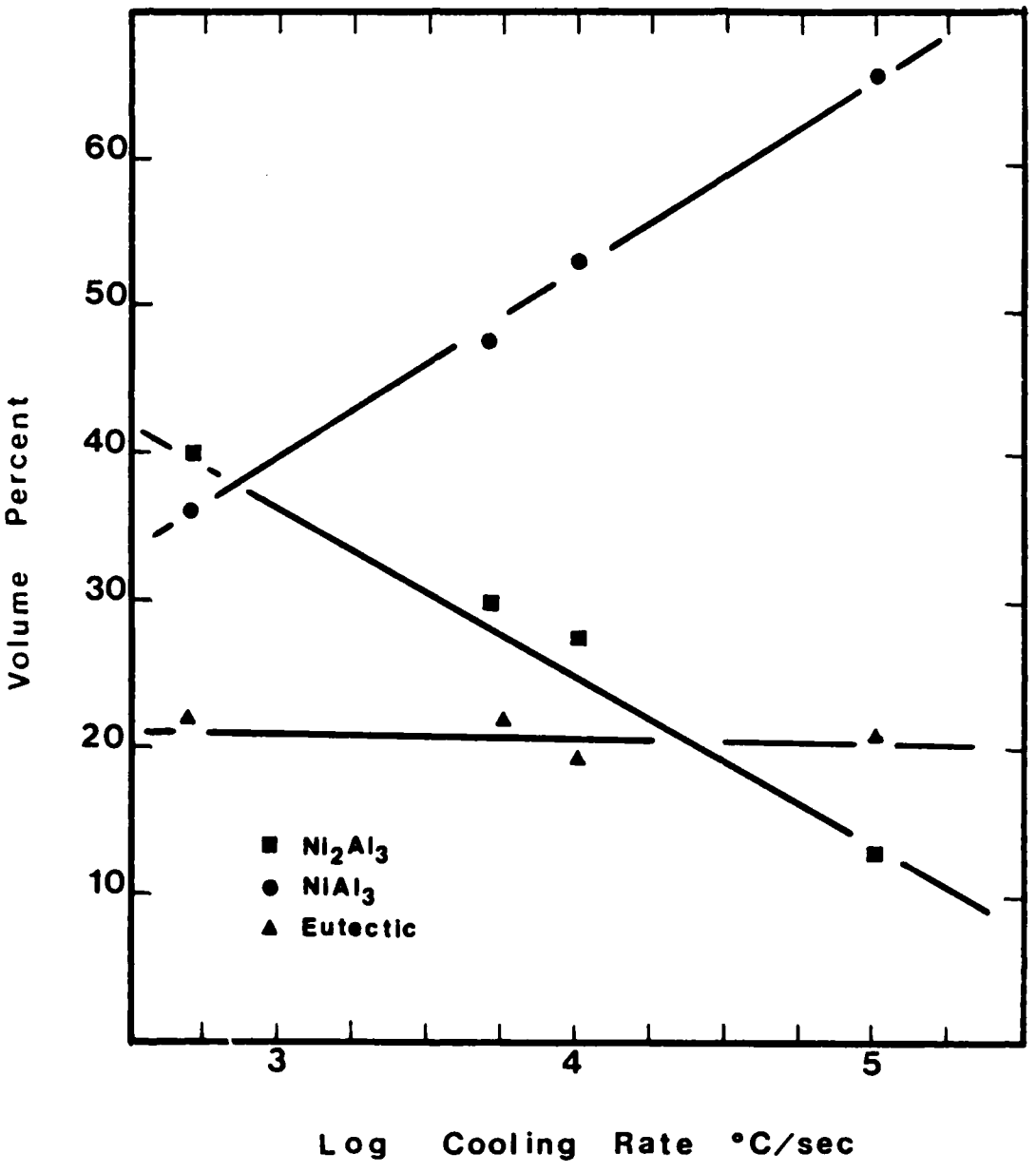

Figure 10. Volume fractions of Ni_2Al_3, $NiAl_3$ and eutectic versus cooling rate for samples quenched from completely liquid.

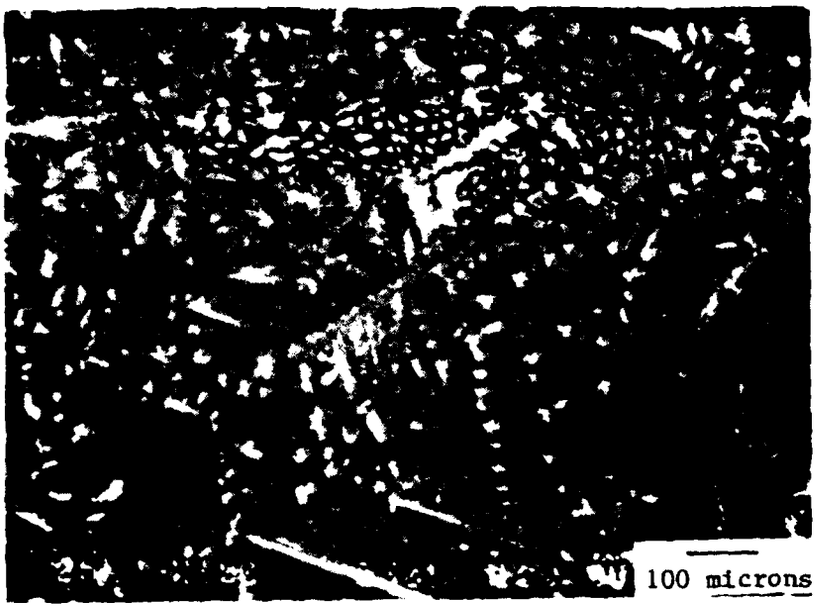

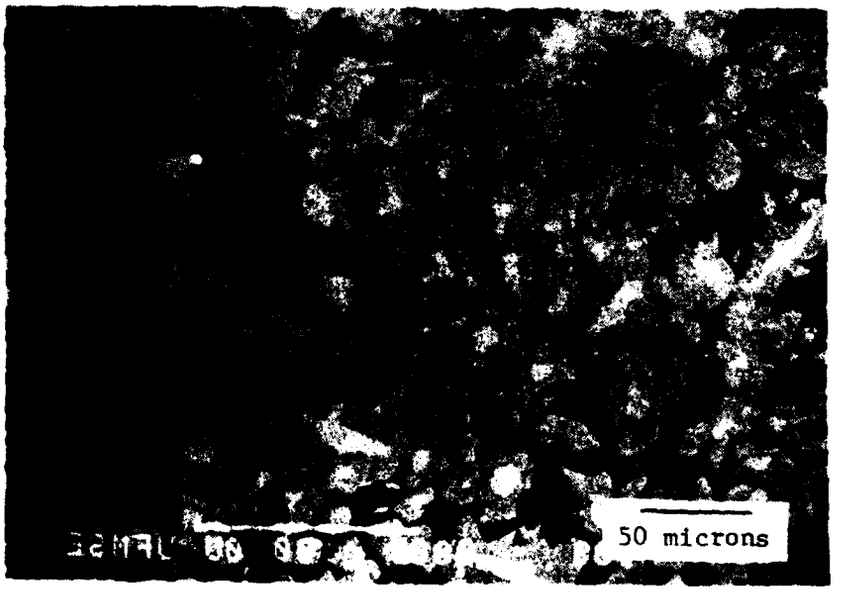

Figure 11. Microstructure of Al-30 wt.% Ni solidified in the levitated state.

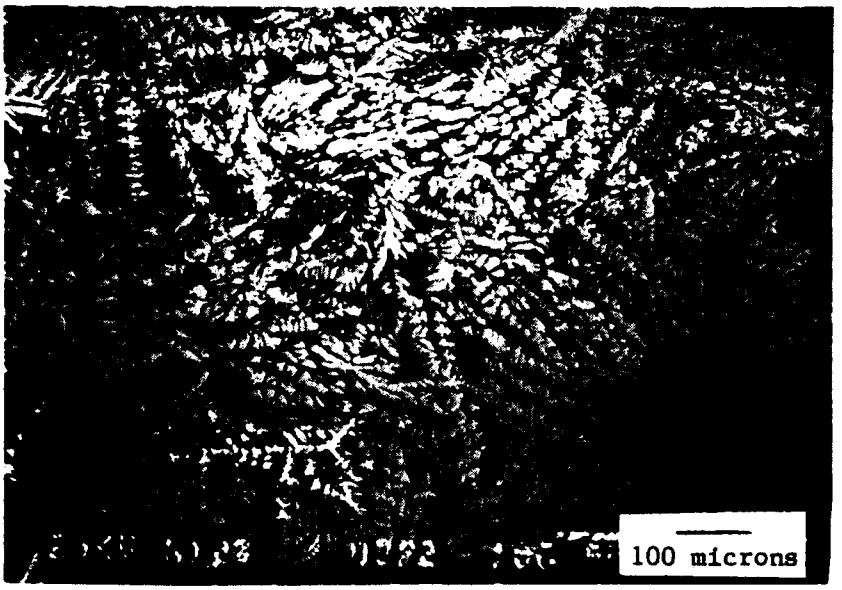

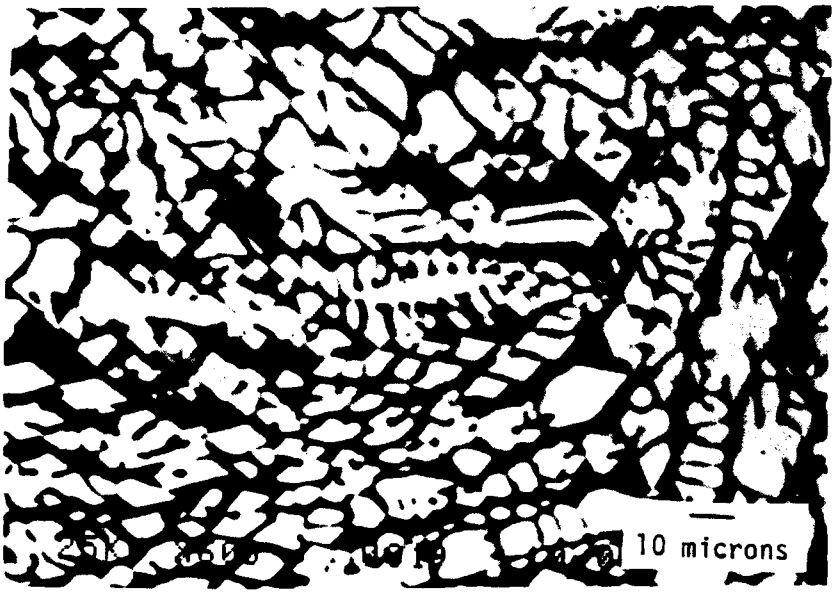

Figure 12. Microstructure of Al-30 wt.% Ni quenched in water from liquid.

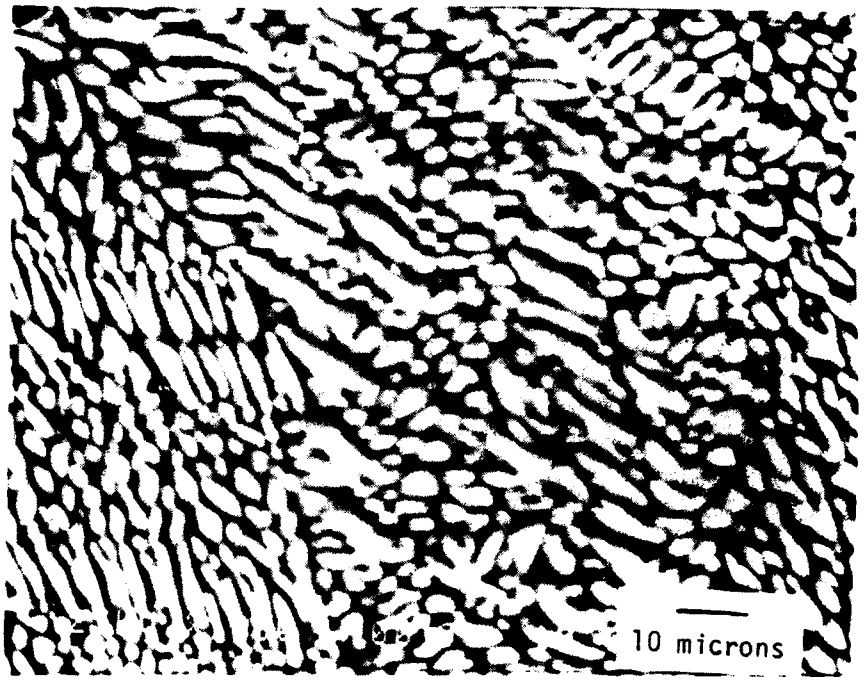

Figure 13. Microstructure of Al-30 wt.% Ni quenched in molten Pb-Sn-Bi eutectic; note the absence of Ni_2Al_3.

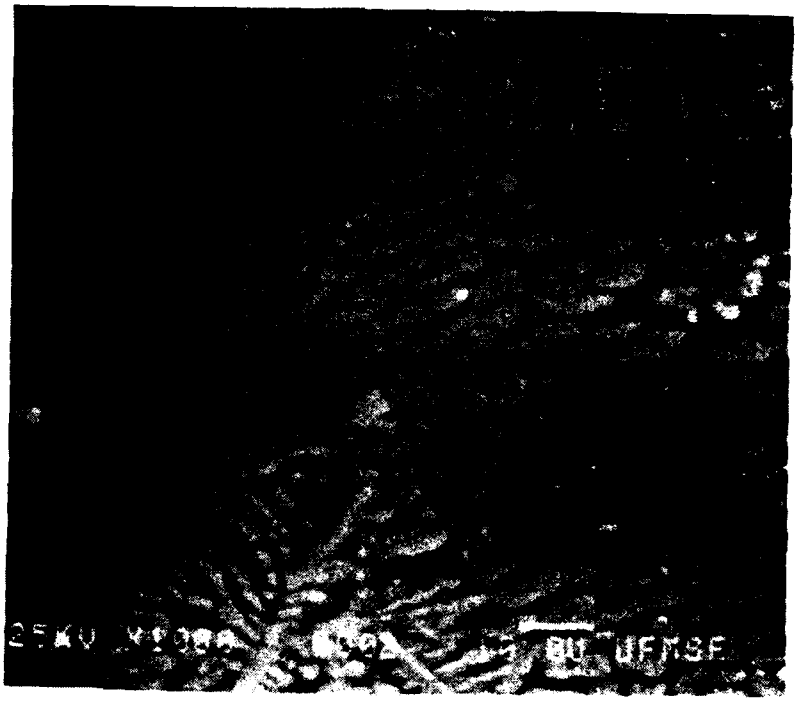

Figure 14. Microstructure of Al-35.4 wt.% Ni quenched in a rotating copper cup taken near the quenched surface. Note separate crystallization of Ni_2Al_3 and $NiAl_3$ phases.

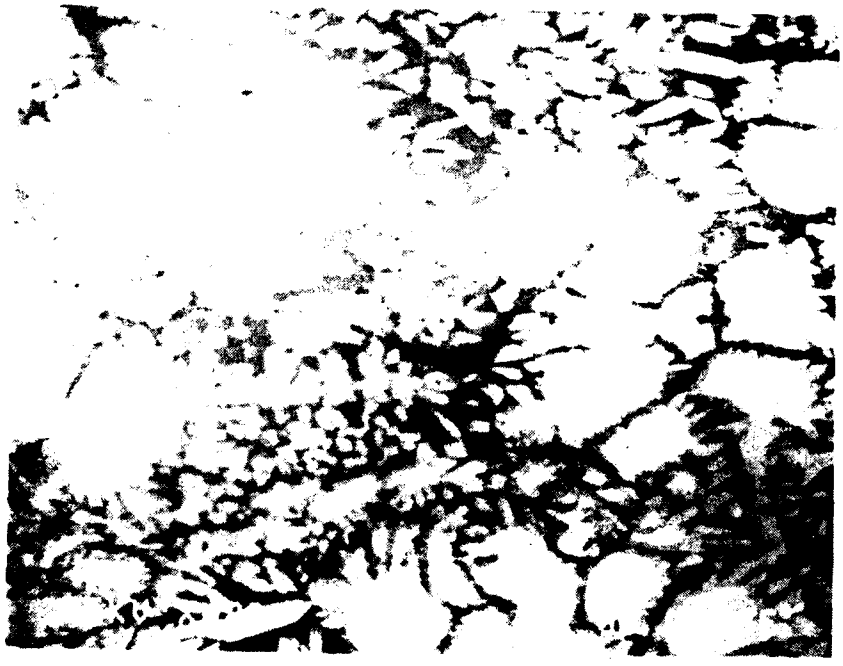

Figure 15. Microstructure of Al-42 wt.% Ni held in the Ni_2Al_3 + liquid region for approximately 1 minute and quenched in Pb-Sn-Bi.

Figure 16. Microstructure of Al-42 wt.% Ni held in the Ni_2Al_3 + liquid region for approximately 7 minutes and quenched in Pb-Sn-Bi.

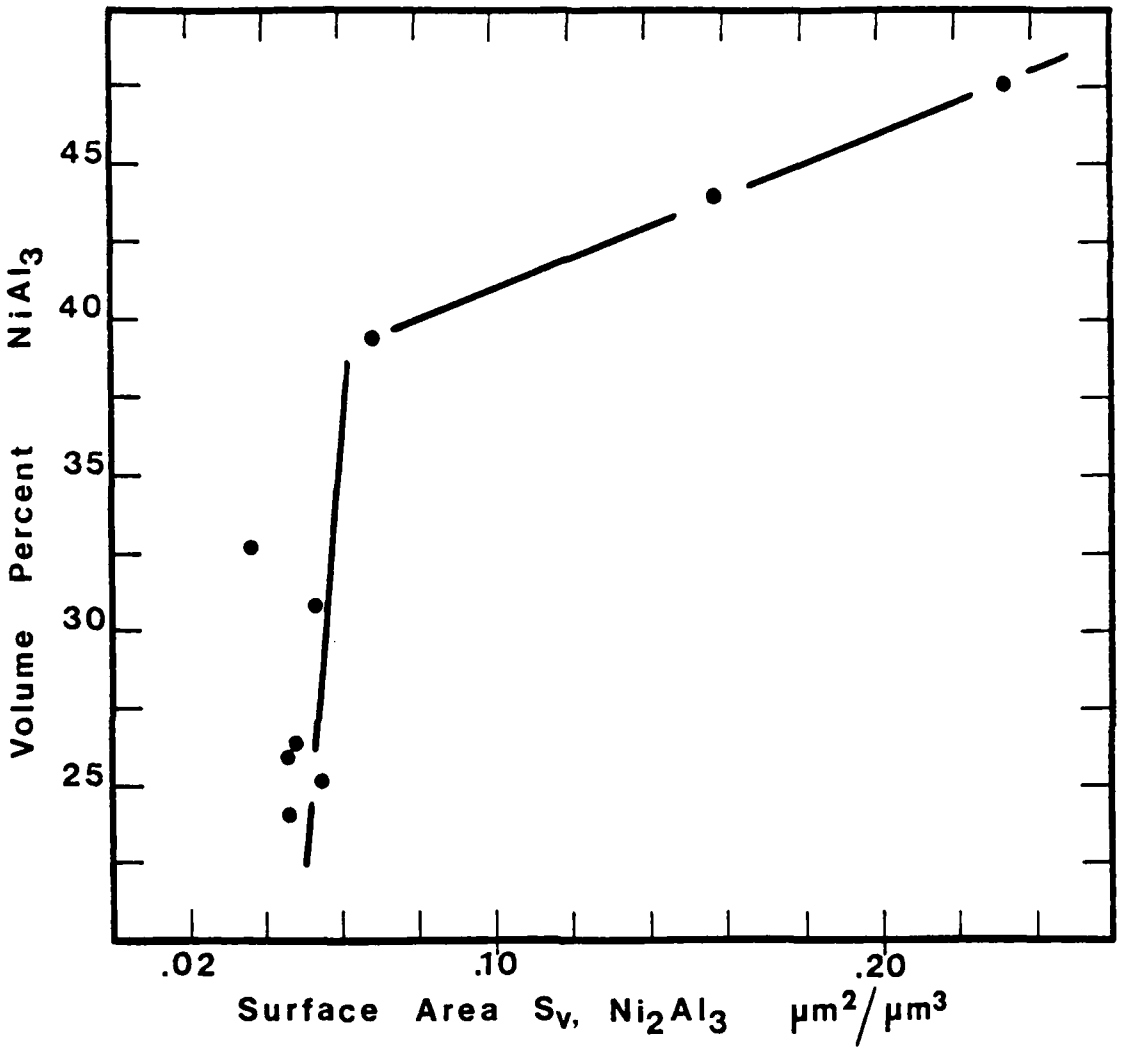

Figure 17. The volume fraction of peritectically formed $NiAl_3$ versus the surface area of the primary phase for samples quenched in Pb-Sn-Bi eutectic.

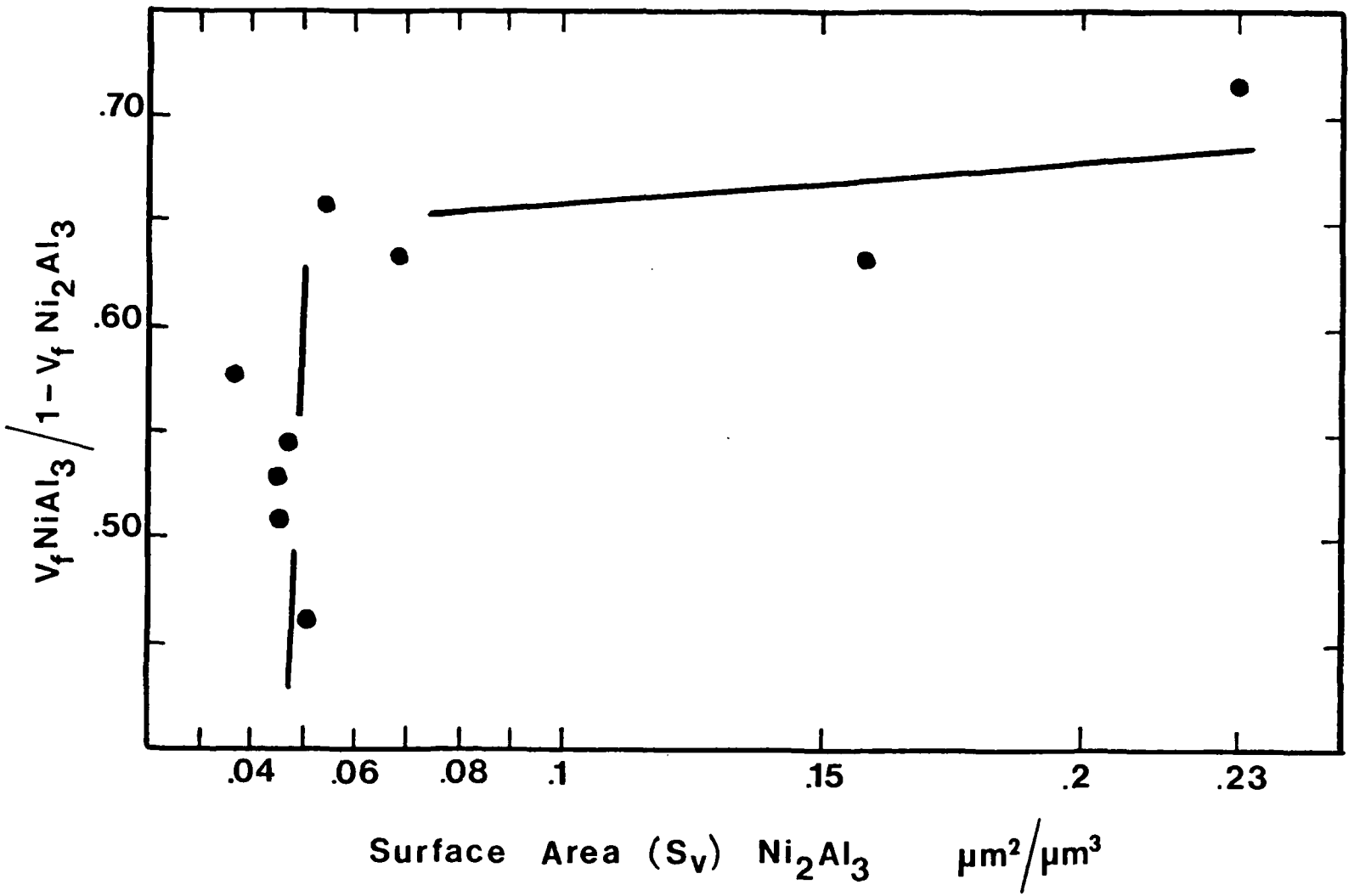

Figure 18. The normalized volume fraction of peritectically formed $NiAl_3$ versus the surface area of the primary phase for samples quenched in Pb-Sn-Bi eutectic.

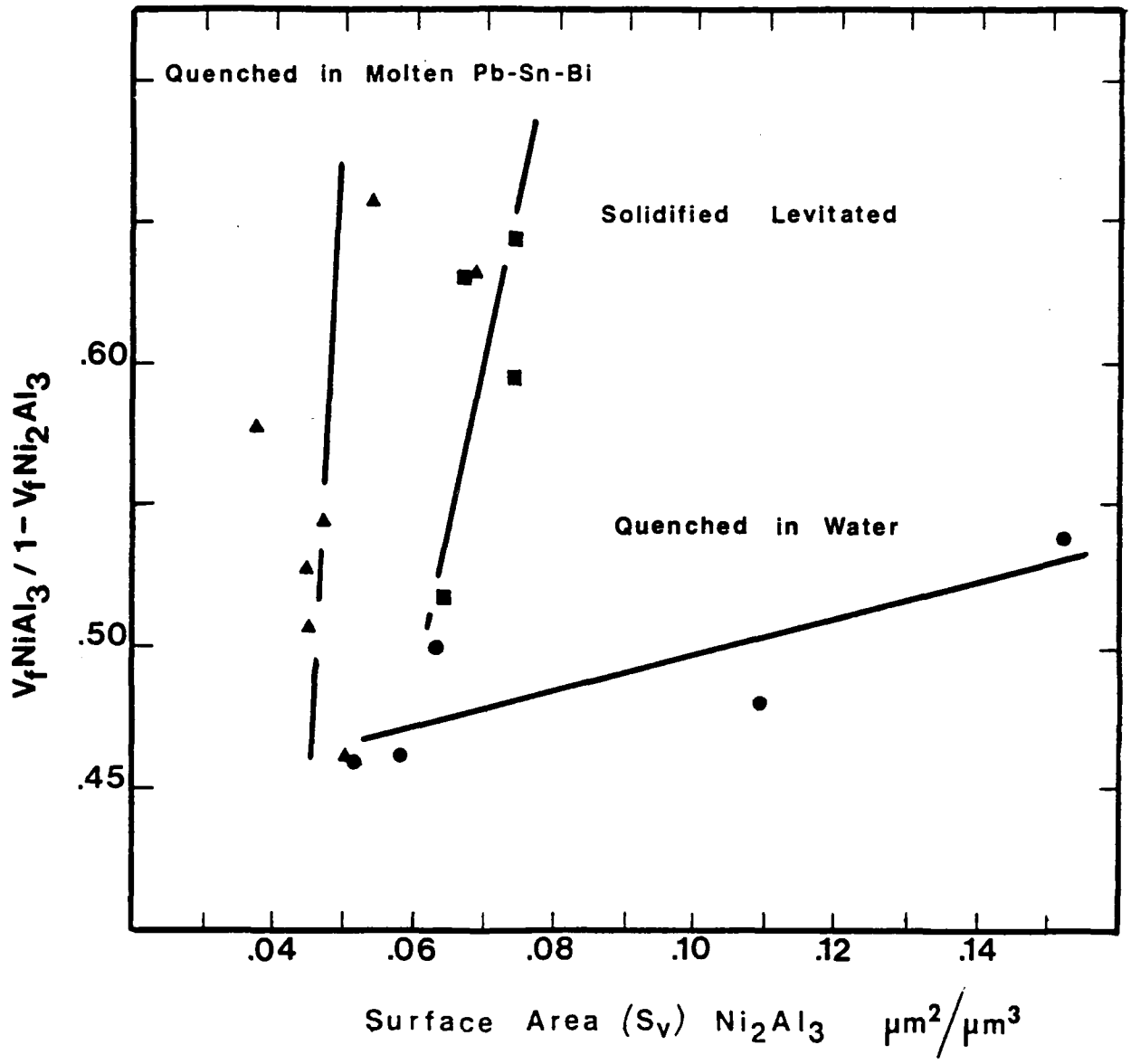

Figure 19. The normalized volume fraction of the peritectically formed $NiAl_3$ versus the surface area of the primary phase for samples quenched from S+L using He gas, water and Pb-Sn-Bi.

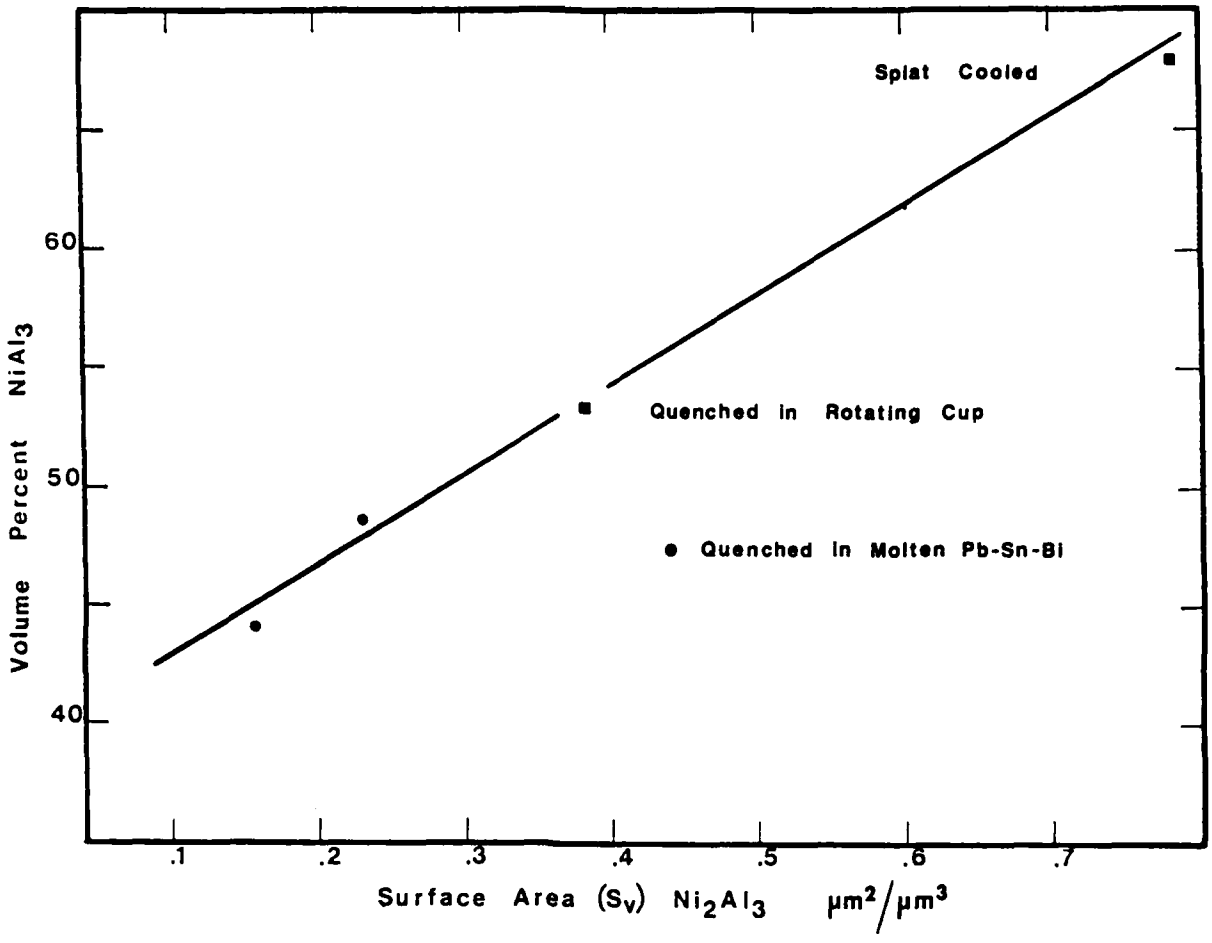

Figure 20. The volume fraction of the peritectically formed $NiAl_3$ versus the surface area of Ni_2Al_3 for samples quenched at 5×10^3, 10^4 and 10^5 °C/sec.

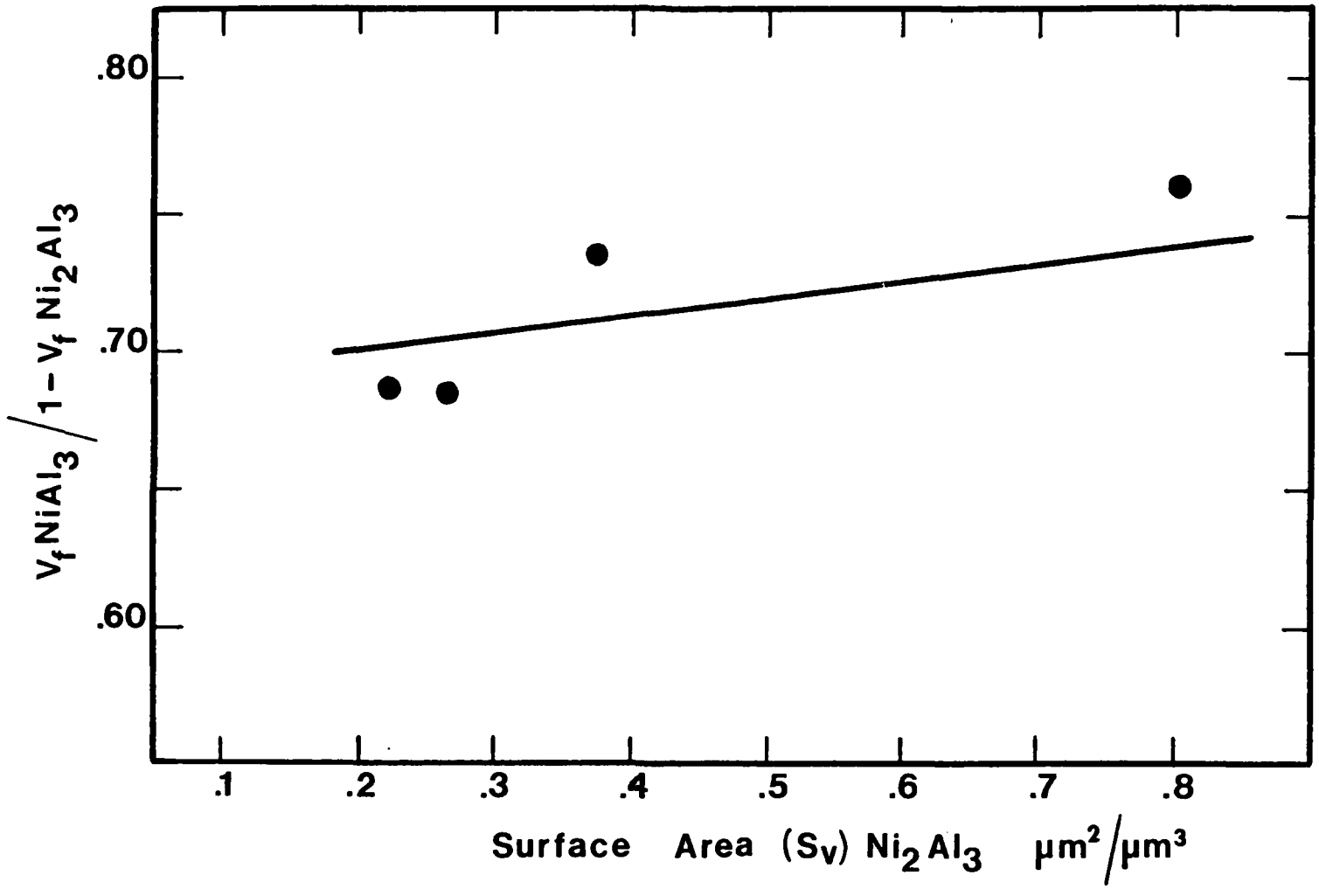

Figure 21. The normalized volume fraction of the peritectically formed $NiAl_3$ versus the surface area of Ni_2Al_3 for samples quenched at 5×10^3, 10^4 and 10^5 °C/sec.

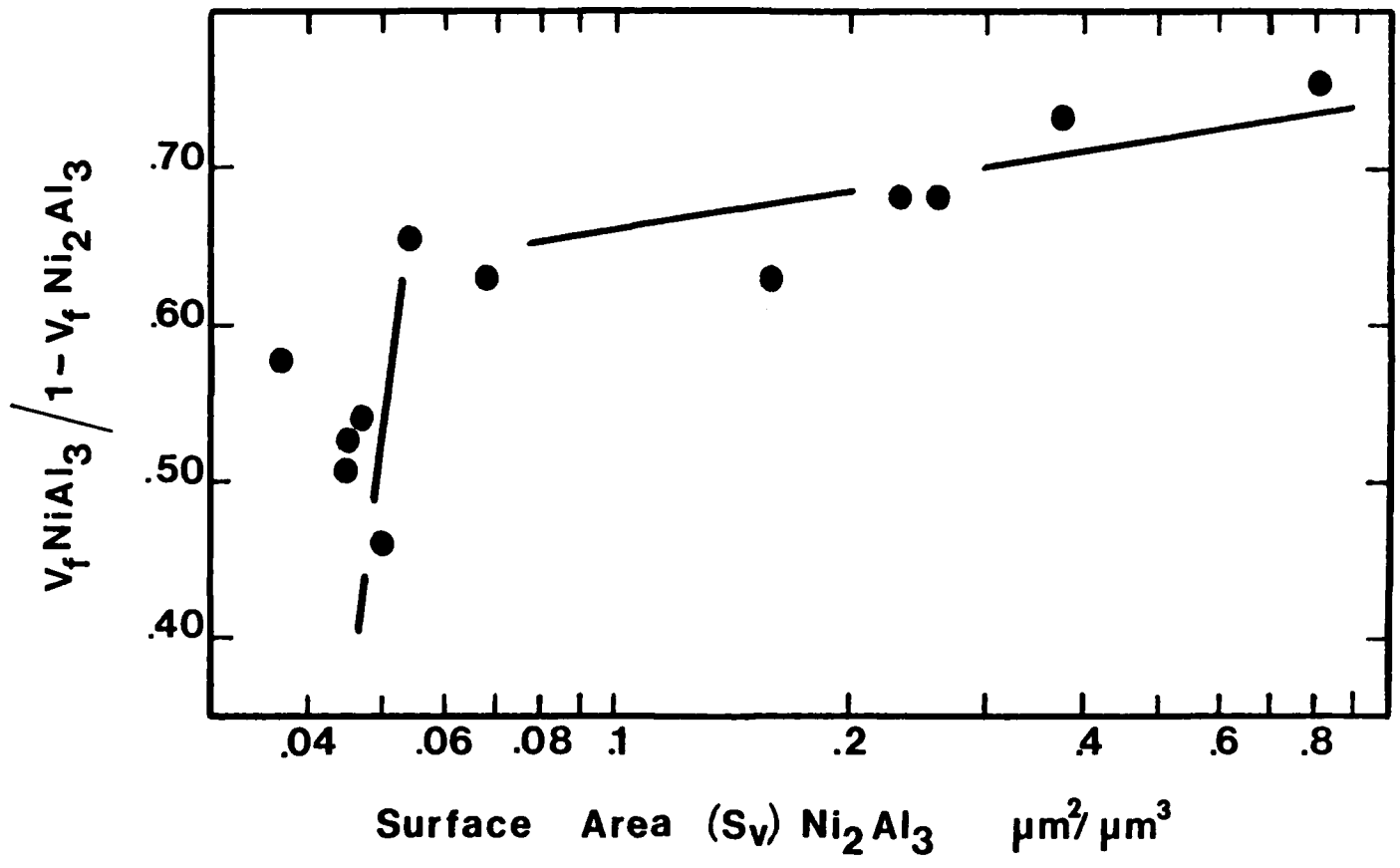

Figure 22. The normalized volume fraction versus surface area of Ni_2Al_3 for samples quenched at 5×10^3, 10^4 and 10^5 °C/sec, and those from S+L into Pb-Sn-Bi.

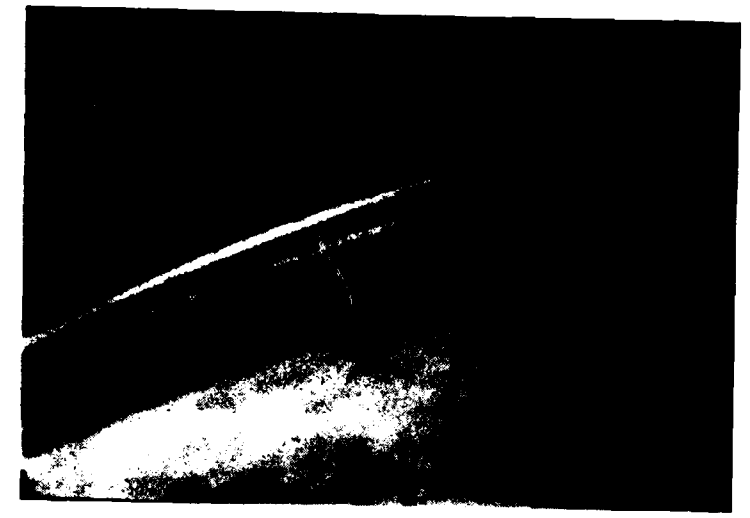

Dark Field

Bright Field

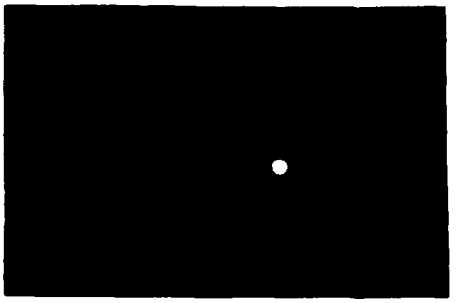

Figure 23. Interference fringes occurring at the $NiAl_3/Ni_2Al_3$ interface. The spot pattern shows the diffracting conditions used to form the image.

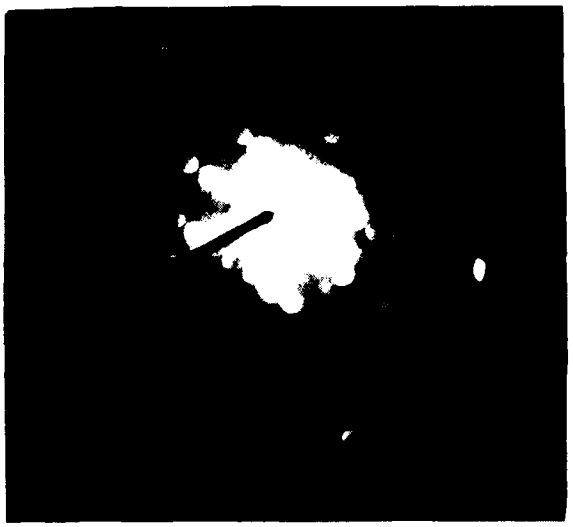

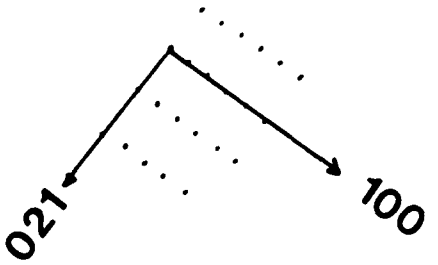

$NiAl_3$

$[0\bar{1}2]$

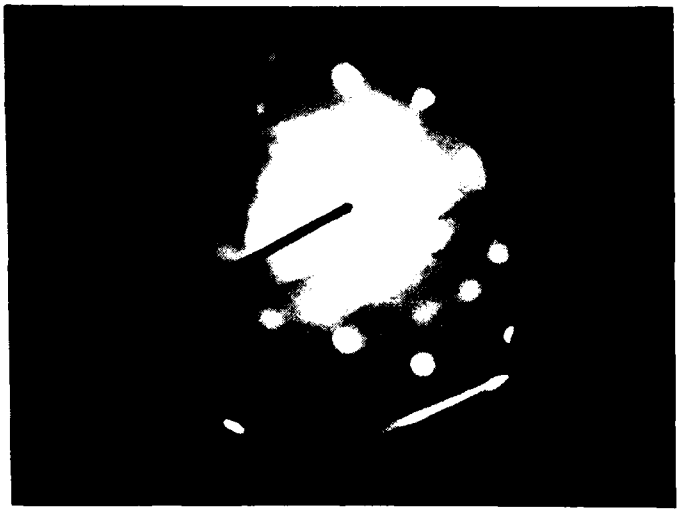

Ni_2Al_3

Figure 24. Diffraction pattern obtained from the $[0\bar{1}2]$ zone axis of $NiAl_3$ and the corresponding diffraction pattern of Ni_2Al_3.

$NiAl_3$

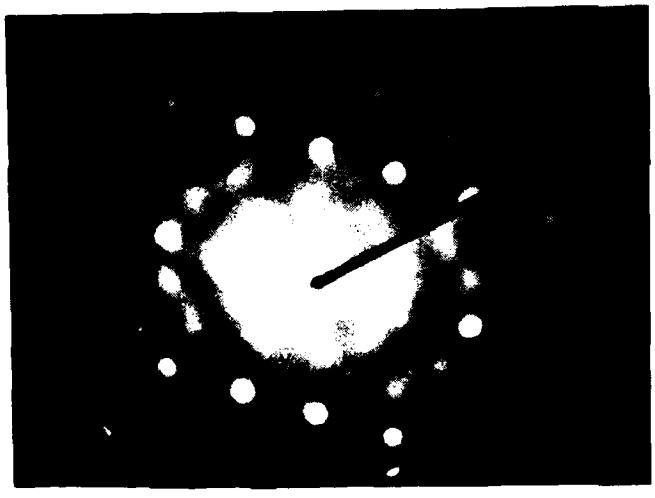

Ni_2Al_3

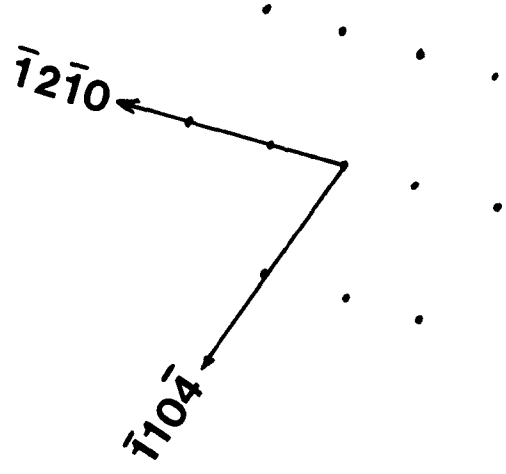

Figure 25. $NiAl_3$ and Ni_2Al_3 diffraction patterns taken along the [4041] zone axis of Ni_2Al_3.

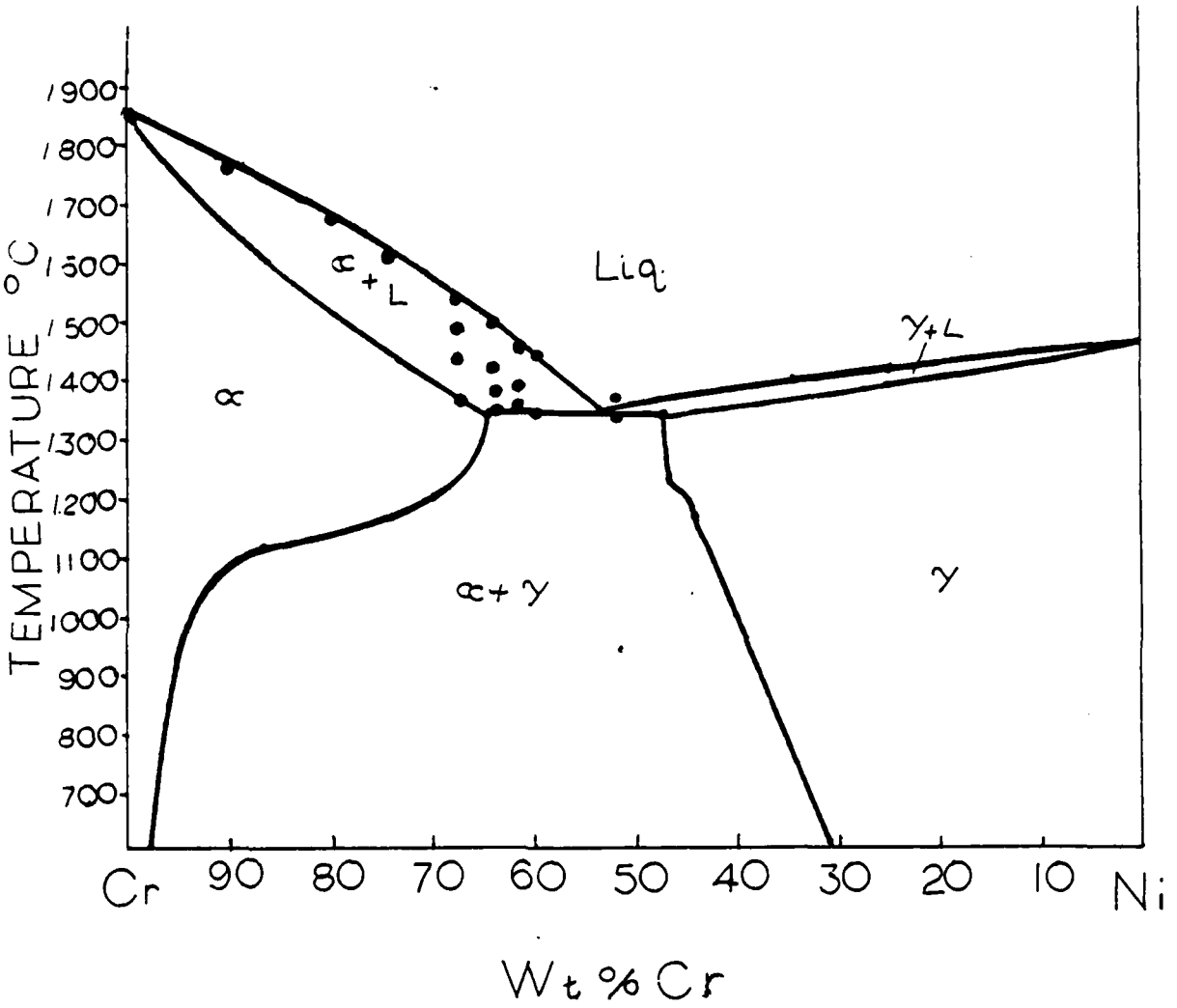

Figure 26. Thermal arrest data superimposed on the currently accepted simple eutectic diagram [7].

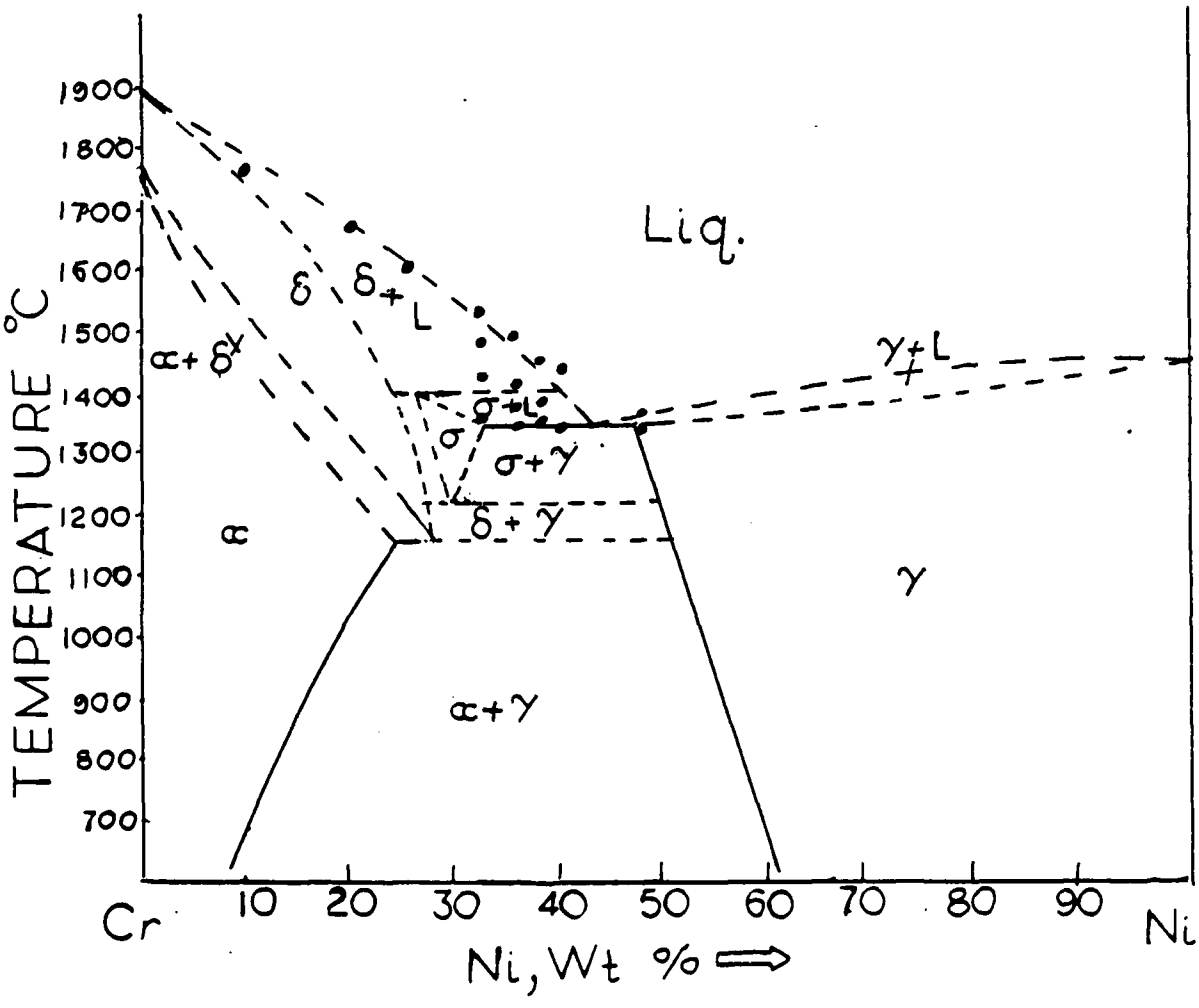

Figure 27. Thermal arrest data superimposed on the diagram proposed by Yukawa [8].

Figure 28. Photomicrograph showing structure of a 67.5 at.% Cr alloy quenched from 1450°C. 200X magnification.

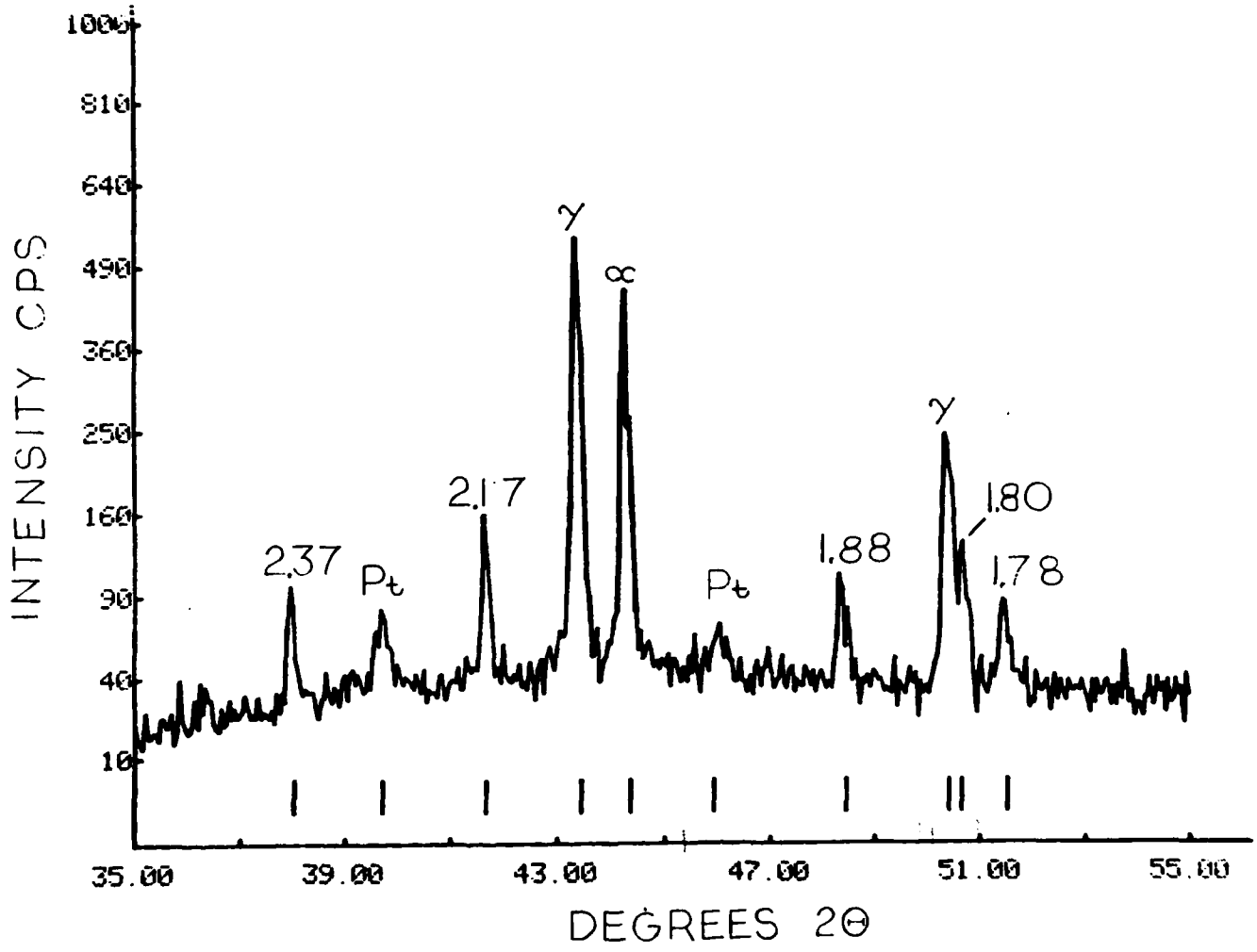

Figure 29. X-ray diffraction scan of a 51 wt.% Cr alloy after being held at 1300 C for 20 minutes.

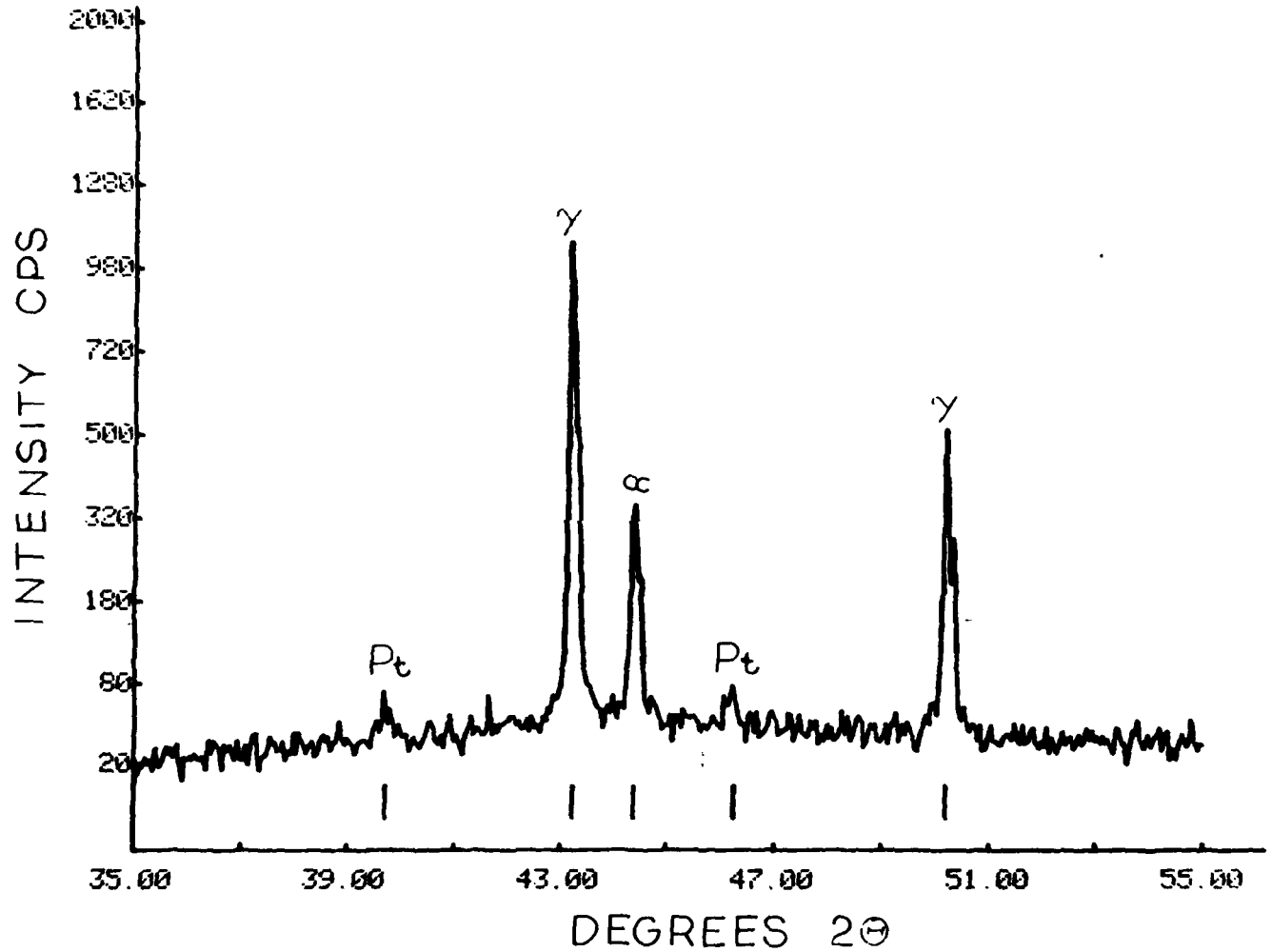

Figure 30. X-ray diffraction scan of a 51 at.% Cr alloy after being held at 1300°C for two hours.

Appendices

A. "Chromium - Nickel Phase Diagram", Alloys Phase Diagrams, Extended Abstracts, Edited by L. H. Bennett, B. C. Geissen and T. B. Massalski, MRS, November, 1984, pp.71-73.

B. "Grain Refinement of Copper by the Addition of Iron and by Electromagnetic Stirring," Met. Trans. B, Vol. 16B, September, 1985, pp.505-511.

C. "Structure and Tensile Properties of A Rapidly Solidified Hot Extruded Al-Li-Mg-Zr Alloy," to be published in the proceeding of the Symposium on Mechanical Behavior of Rapidly Solidified Materials, Edited by B. A. MacDonald et al, TMS Publications.

D. "Refining of Niobium by Levitation Melting Technique", Journal of Metals, Vol. 37, No. 4, April 1985, pp.22-26.

APPENDIX A

CHROMIUM - NICKEL PHASE DIAGRAM, R. M. Schmees* and G. J. Abbaschian**, *Government Products Division, Pratt & Whitney Aircraft, P. O. Box 2691, West Palm Beach, FL 33402. **Department of Materials Science and Engineering, University of Florida, Gainesville, FL 32611

The commonly accepted Cr-Ni diagram at high temperatures consists of a simple eutectic at 1345°C and about 51 wt.% chromimum. Notwithstanding, there are at present three other proposed diagrams that include, in addition to the eutectic, either a eutectoid [1], a peritectic plus two eutectoids [2], or four eutectoid tranformations [3]. The center of controversy in the phase diagram lies in whether or not chromimum undergoes any allotropic transformation that would cause eutectoid transformations in the binary alloys. The existence of a Cr-Ni sigma phase, formed by the peritectic transformation, is also another source of controversy. The major difficulties in studying Cr-Ni phase diagram are due to intense volatilization of Cr at high temperatures, the high affinity of chromimum with oxygen, solid state precipitations which may obscure phase transformations, and effects due to impurities.

In the present study, electromagnetic levitation was used to study the nature of solid-liquid phase transformations in the chromimum-rich side of the diagram.The levitation apparatus used in this study has been described previously [4]. The samples, each weighing about one gram, were prepared from high purity nickel (99.99 and 99.999%) and chromimum (99.95 and 99.9999%). The alloys were prepared in a vacuum arc melting furnace partially backfilled with high purity argon. A titanium "getter" was melted prior to melting of the samples. A sample as prepared was lowered into the levitation coil using a nickel wire which was pulled out of the field as soon as the sample levitated. High purity helium or argon was continuously passed through the glass tube surrounding the sample in order to control its temperature and to prevent oxidation. The inert gases were purified by passing them through a gas purifier, which utilized titanium at 800°C as a getter. The oxygen content of the purified gas was continuously monitored to be in the range $1x10^{-15}$ ppm. After melting the sample, the flow of gas and the power input into the coil were adjusted so that the temperature of the sample decreased at a rate of about 30°C per second, while its temperature was continuously monitored by a two-color pyrometer with an accuracy of ±10°C at temperatures below 1700°C. The thermal arrest points during normal (non-equilibrium) cooling of each sample was obtained several times by repeatedly melting and solidiying it. The sample was finally quenched in water from a desired temperature, and its room temperature characteristics were examined using metallography, TEM and X-ray.

The metallagraphic examination of the 55 wt.% chromium alloys quenched at various temperatures indicated that they generally contained chromium dendrites, surrounded by a divorced eutectic. The chromium dendrites had gone through a solid-state transformation into a Widmanstätten type structure. At 62 wt.% chromium, a central region was observed inside the dendrite, similar to those observed during peritectic transformations. The central region became more extensive as the chromium content of the alloys increased, as shown in Figures 1a and 1b. There was a clear and distinct boundary between the two regions within the chromium phase, ruling out simple coring due to the compositional variation. There was also a difference in the decomposition morphology of the two regions; fine precipitates were observed by TEM in the central region, as opposed to the Widmanstätten type structure in the outer part. Furthermore, the Widmanstätten plates stopped at the boundary between the two regions, possibly indicating a difference in the crystal structure of the two regions. The structure, similar to those observed by Amaya [5], is believed to have formed by a peritectic reaction, and might be the sigma phase reported by Yukawa et al. [2].

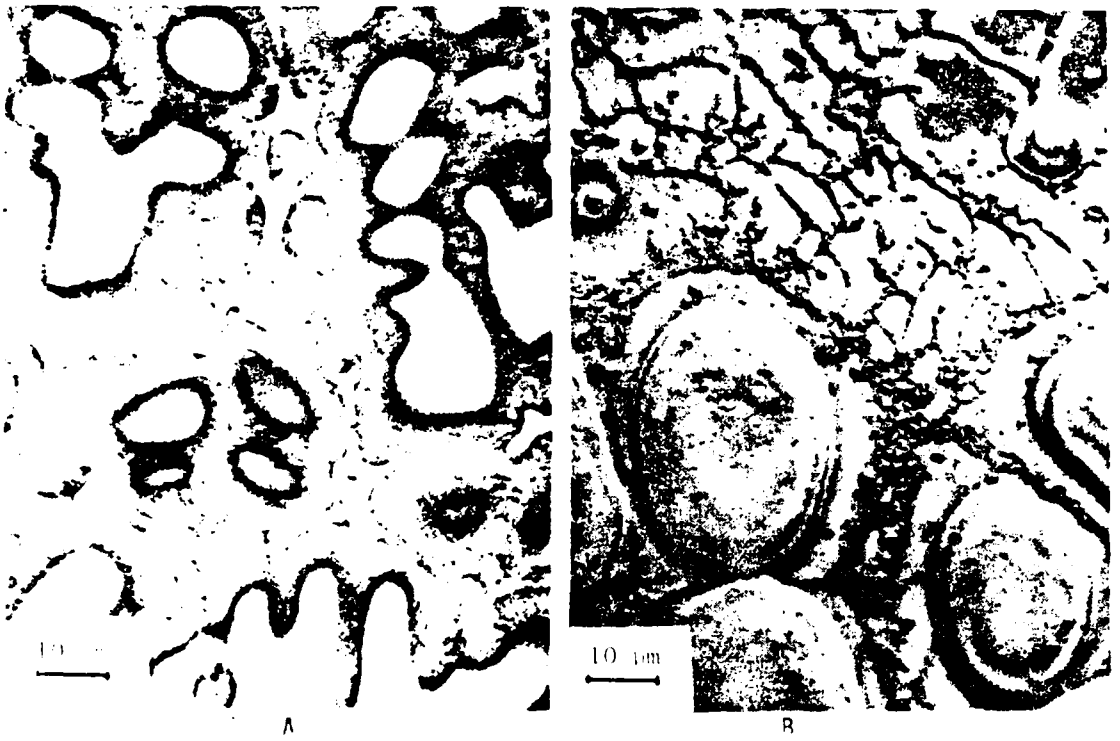

Figure 1 - Microstructures of two 71 wt.% Cr samples quenched at (a) 1490, and (b) 1380°C.

STEM analysis indicated that for the 71 wt.% chromium samples, the composition of the pro-peritectic phase ranged from 72 to 77 wt.% Cr, and that of the peritectic phase from 60 to 70 wt.%. The composition of the nickel phase in the interdendritic region which contained small precipitates ranged from 51 to 53 wt.% chromium. The TEM and x-ray diffraction patterns indicated that room temperature crystallagraphic structures were those of the BCC chromium and the FCC nickel. However, in one sample extra peaks at 77.4° and 86.6° were noted by the x-ray diffraction. It should be noted that the fact that only the BCC and FCC phases were found at room temperature does not necessarily mean that other structures do not exist at high temperatures.

The thermal arrest points obtained during normal cooling of the levitated alloys are given in Table I. The highest thermal arrest point for each sample corresponds to the liquidus temperature. This is also the temperature at which the first solid was visually observed to form on the surface of the levitated sample. The other thermal arrest points represent some form of phase transformation or precipitation during normal solidification and cooling of the samples. For the alloys containing 55 wt.% Cr, the liquidus temperature was found to be between 1375 and 1380°C. In addition a second thermal arrest corresponding to the eutectic was observed at 1345°C, in agreement with that of Amaya [5] and the accepted diagram. However, the other thermal arrest points above the eutectic temperature that occur in the alloys containing more than 62 wt.% chromium indicate that reactions occur that are not consistent with the commonly accepted eutectic diagram. The thermal arrest point around 1442±26°C in these alloys seems to be independent of the composition. This monovariant temperature most likely belongs to the peritectic transformation. The nature of the thermal arrest point around 1510°C for the 78 wt.% chromium samples and one 71 wt.% sample is not clear yet.

When the samples were levitated in the as received inert gases which contained about 6ppm oxygen, there was a decrease in the liquidus temperature. The number of thermal arrest points, and the relative amount of the peritectic phase also decreased.

Acknowledgements

The financial assistance of the office of Naval Research, under contract number N00014-81-K-0730, is appreciated. The scientific officer of the project was Dr. Bruce A. MacDonald.

Table I - Thermal arrest points during non-equilibrium cooling of samples levitated in purified inert gas.

wt.% Cr	Liquidus, °C	Additional Arrest Points, °C			
55	1375			1345	
55	1380				
Average	1377				
62	1452		1421	1366	(1335)
62	1447				(1335)
Average	1449				
65	1500		1423	1359	
65	1511		1430	1382	
65	1534		1474	1405	1350
Average	1515				
71	1552				
71	1570		1460		
71	1585	1513	1438		
Average	1577				
78	1641		1458		
78	1610	1504	1435		
78	1633	1533			
78	1627	1501	1447	1385	
Average	1628				
90	1760		1435		
90	1755		1444		
Average	1757				

( ) - Temperatures in parentheses represent small slope change in the thermal data, rather than clear recalescence.

References

1) D. S. Bloom and N. J. Grant: "Chromium-Nickel Phase Diagram," J. Metals, Nov. 1951, vol. 3, p. 1009.

2) N. Yukawa, M. Hida, T. Imura, M. Kawamura, and Y. Mizuno: "Structure of Chromium-Rich Cr-Ni, Cr-Fe, Cr-Co, and Cr-Ni-Fe Alloy Particles Made by Evaporation in Argon," Met. Trans., April 1972, vol. 3, p. 887.

3) A. T. Grigor'ev, E. M. Sokolvskaya, N. A. Nedumov, M. V. Maksimova, L. G. Sokolova, and Yeh Yu-pu: "Polymorphic Changes in Chromium: The Phase Diagram of the Chromium-Nickel System in the Chromium-Rich Region," Russian J. of Inorganic Chemistry, May 1961, vol. 6, no. 5, p. 639.

4) G. E. Amaya, J. A. Patchett, and G. J. Abbaschian, "Grain Refining in Cr, Ni and Cr-Ni Alloys," in Grain Refinement in Castings and Welds, p.51, edited by G. J. Abbaschian and S. A. David, Conference Proceedings, TMS-AIME, 1982.

5) G. E. Amaya: "Solidification of Levitation Melted Ni and Ni-Cr Alloys," Master Thesis, University of Florida (1984).

APPENDIX B

Grain Refinement of Copper by the Addition of Iron and by Electromagnetic Stirring

J. A. PATCHETT and G. J. ABBASCHIAN

The effect of iron additions in the range of 0.57 to 7.5 wt pct on the grain size of electromagnetically levitated copper-iron alloys was investigated. The samples were solidified while levitated or quenched in water from the molten state. The addition of iron was found to be effective in reducing the grain size of copper, and the average grain size decreased as the iron content was increased up to the peritectic liquid composition of about 2.8 wt pct Fe. Beyond this composition, the grain size of the samples solidified in the levitated state was insensitive to the iron content, whereas that of the quenched samples continuously decreased with increasing iron content. The results indicate that electromagnetic stirring causes fragmentation of copper dendrites in the hypoperitectic region, and hence enhances grain refinement. In the hyperperitectic region, on the other hand, the stirring has a detrimental effect on the grain refinement by agglomerating the primary iron particles which act as heterogeneous nucleation sites for the copper matrix.

I. INTRODUCTION

THE importance of fine equiaxed grains as opposed to columnar grains has long been recognized in a casting. Among various enhanced properties associated with a fine grain structure are improved low-temperature strength, reduced anisotropy, formability, and reduced segregation scale. The latter is especially important in castings that have to undergo homogenization; in a fine grain structure the characteristic diffusion distance and hence the homogenization time is reduced compared to a coarse grain structure. A number of techniques have been developed to produce fine grain structures during solidification.[1] The most common method is to add small amounts of grain refining agents, inoculants, to the melt just prior to casting. The additions either go into solution or remain as solids that act as heterogeneous nucleation catalysts during solidification. Examples of grain refining agents employed commercially for various alloys have been given in a recent review article by Mondolfo.[2]

It is commonly accepted that the effectiveness of a grain refining agent is either due to enhanced heterogeneous nucleation rate or due to a reduction in the growth rate of the existing grains, thus allowing for further nucleation. However, the actual mechanism of grain refinement and hence the criteria which determine the effectiveness of one addition *vs* another are not fully understood. In general, the requirements for a good nucleating agent are higher interfacial energy between the inoculant and the melt, compared to that between the nucleated solid and the melt, and a good epitaxial fit between low index planes of the inoculant and the solid.[3] In addition, the inoculant particles should be stable at the melt temperature, and should not agglomerate or float. A lower degree of lattice mismatch between the nucleant and the solid has been suggested as a possible criterion to determine grain refining potency of an inoculant.[4] In the absence of accurate surface energy data, Youdelis[5] has suggested the use of the "nucleation entropy" as a criterion for grain refining effectiveness. Based on this criterion, the larger the nucleation entropy, the more effective is the grain refiner. The solute build-up ahead of the solid-liquid interface, proposed by Tarshis *et al.*,[6] is another criterion for evaluating effectiveness of alloy additions. According to this criterion, the greater the solute build-up ahead of the interface, the more effective is the alloy addition in promoting grain refinement. Grain refining *via* peritectic reactions is another well known technique that is commercially employed in various alloys, especially in aluminum based alloys.[7,8]

The grain refining techniques discussed above involve the deliberate addition of alloying elements or compounds to the melt. Equally important factors in determining the microstructure are the fluid flow and thermal conditions during solidification. The fluid flow can cause dendrite fragmentation by bringing hotter liquid to the root of the dendrite arms. The fragments, when carried away, can serve as growth sites for new grains. Improved fluid flow can come from a number of sources such as ultrasonic vibrations,[9] mechanical stirring,[10,11] or electromagnetic stirring.[12] The latter is being used extensively in casting industries, particularly for alloy compositions that have a strong tendency for centerline segregation and shrinkage porosity.

The present experiments were conducted to establish the role of the peritectic reaction and electromagnetic stirring in the grain refinement of copper-iron alloys. The effects of cooling rate and alloy compositions were also studied.

II. EXPERIMENTAL PROCEDURE

The experimental apparatus consisted of an electromagnetic levitation chamber, an inert gas purifying system, and a temperature monitoring device. Details of the apparatus can be found in an earlier paper.[13] The temperature of the levitated sample was measured and continuously monitored by a two-color pyrometer connected to a strip chart recorder. The pyrometer was calibrated against the melting points of pure iron, nickel, and copper to an accuracy of ±5 °C. High purity helium, argon, and/or helium -2.0 pct hydrogen were continuously passed through the glass tube surrounding the

J. A. PATCHETT, a Graduate Research Assistant, and G. J. ABBASCHIAN, Professor, are with the Department of Materials Science and Engineering, University of Florida, Gainesville, FL 32611.

Manuscript submitted November 29, 1984.

sample to provide cooling and to protect the sample from oxidation. The oxygen content of the purified gas, continuously monitored using a solid state electrolyte, was in the range of 10^{-15} ppm.

The samples, each weighing about one gram, were prepared from 99.999 pct copper and 99.98 pct iron. The constituents for each sample, weighed to an accuracy of ±0.0001 g, were arc melted in a titanium "gettered" helium atmosphere. The arc-melted sample was lowered into the levitation coil, and the power to the coil was adjusted to levitate, melt, and superheat the sample by approximately 300 °C. The gas flow was then increased to solidify the sample at a rate of about 10 to 20 °C per second. The thermal arrest points corresponding to liquidus and peritectic temperatures were recorded during repeated heating and cooling cycles of the levitated sample.

After determining the thermal arrest points, two different processing procedures were used to solidify the sample. One involved cooling the sample in the levitated state to 1000 °C, at a rate of 10 to 20 °C per second, then quenching the solid sample in water from this temperature. The other involved quenching the sample from a temperature slightly above its liquidus temperature in water. The cooling rate of the water quenched samples is estimated to be approximately 500 °C per second.[14] The samples were sectioned, mounted, polished, and their average grain sizes were determined using a standard intercept technique.[15]

III. RESULTS

The compositions, thermal arrest points, and the average grain sizes of the as-quenched samples are summarized in Table I. The liquidus points and the peritectic temperature, as shown in Figure 1, were found to be in good agreement,

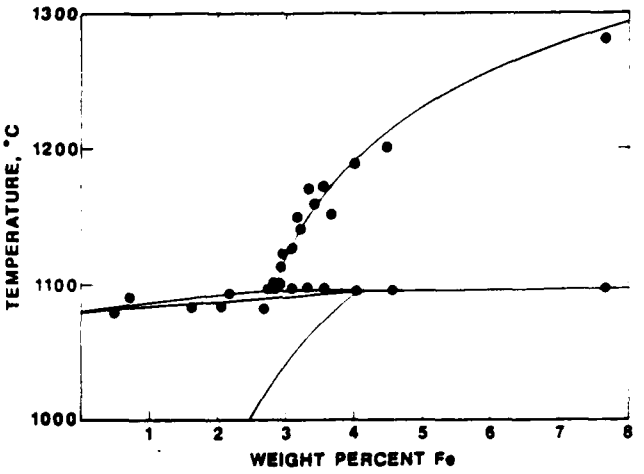

Fig. 1 — The copper-iron phase diagram on the copper rich side, with the measured liquidus and peritectic temperatures.

within the experimental errors, with the commonly accepted phase diagram.[15] Because of the oscillation of the sample in the levitated state, the temperatures could be measured with accuracy of ±10 °C. The minimum concentration of iron required to have an iron rich primary phase, as detected by metallography and SEM, was found to be 2.8 wt pct. Following an earlier convention,[16] alloys containing iron less than this value are termed "hypoperitectic", whereas those containing more iron are called "hyperperitectic".

The average grain size of samples quenched from their corresponding liquidus temperatures as a function of the iron content is shown in Figure 2. The error bars in this figure show the statistical variation of the mean. The average grain size of the pure copper when quenched from its melting point, not shown on this graph, corresponded to roughly

Table I. Thermal Arrest Points and Grain Size Measurements for Copper-Iron Alloys

Wt Pct Fe	Liquidus, °C	Peritectic, °C	Quenching Temp., °C	Grain Size, mm
		Quenched in Water		
0.57	1080	—	1085	0.330 ±0.170
2.05	1080	—	1090	0.130 ±0.050
2.80	1094	1094	1100	0.070 ±0.020
2.84	1100	1100	1115	0.035 ±0.008
3.08	1124	1100	1140	0.032 ±0.010
3.12	1150	1094	1160	0.021 ±0.004
3.20	1140	1090	1150	0.032 ±0.007
3.42	1170	1100	1185	0.037 ±0.007
3.67	1150	1094	1260	0.030 ±0.008
4.06	1190	1090	1265	0.022 ±0.008
		Solidified in the Levitated State		
0.72	1090	—	1000	0.210 ±0.090
1.65	1080	—	1000	0.200 ±0.040
2.14	1090	—	1000	0.110 ±0.040
2.67	1080	—	1000	0.120 ±0.040
2.72	1094	—	1050	0.052 ±0.008
2.80	1100	—	1000	0.220 ±0.080
2.81	1094	—	1000	0.110 ±0.040
2.86	1110	1094	1000	0.042 ±0.010
3.27	1170	1100	900	0.073 ±0.026
3.35	1160	1090	1000	0.071 ±0.020
7.46	1280	1094	1000	0.072 ±0.015

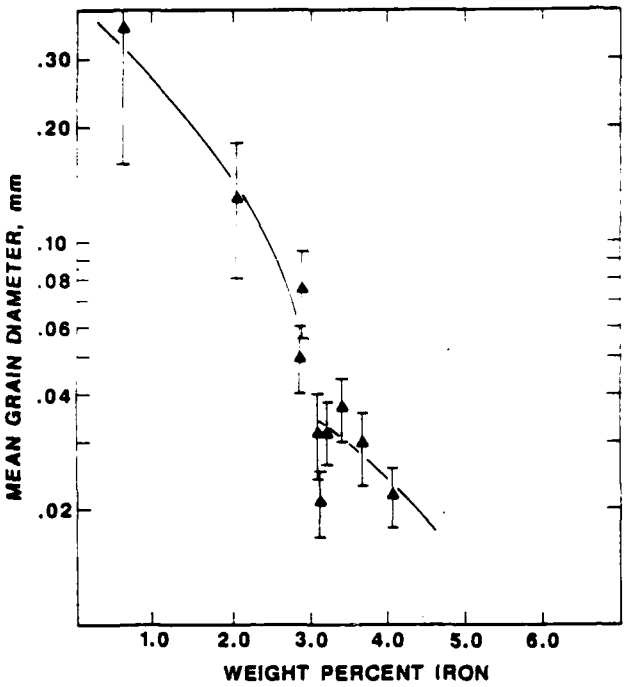

Fig. 2—Mean grain size *vs* iron content for samples quenched in water from their liquidus.

3 mm. The results indicate that the addition of iron causes considerable grain refinement in copper, and the refinement increases with the iron content, as shown in Figure 3 for two samples containing 0.57 and 2.05 pct Fe.

The effectiveness of iron as a grain refiner was further evidenced by the amount of bulk supercooling of the levitated melt. Although it was possible to supercool pure copper in excess of 400 °C,* the addition of iron reduced this supercooling drastically. For example, when the alloy contained about 1 pct iron, the maximum supercooling was reduced to 100 °C. At iron concentrations near the peritectic liquid and beyond, no appreciable supercooling was observed. A similar trend in the reduction of supercooling by the addition of iron was also noted by Southin and Weston.[7]

*In several occasions, pure copper samples were supercooled considerably below the lower limit of pyrometer detection which was 700 °C.

In the composition range immediately surrounding 2.8 wt pct iron, from approximately 2.75 to 2.9 wt pct, the grain size showed considerable scatter. The variations in grain size can be seen in Figure 4 for two samples containing 2.80 and 2.84 pct Fe. Over this rather narrow composition range, the scatter of the mean grain size of individual samples fell outside the confidence intervals of each sample. The scatter appears to be due to the possible alternative nucleation sequences, caused by supercooling, and suppression of the primary phase formation or the peritectic reaction.

When the concentration of iron exceeded 2.9 wt pct, the grain size showed a continued decrease with increasing iron concentration. The microstructures encountered in this region are shown in Figure 5, where the primary gamma iron appears as dark particles scattered uniformly throughout the sample. The data points in this region, however, do not

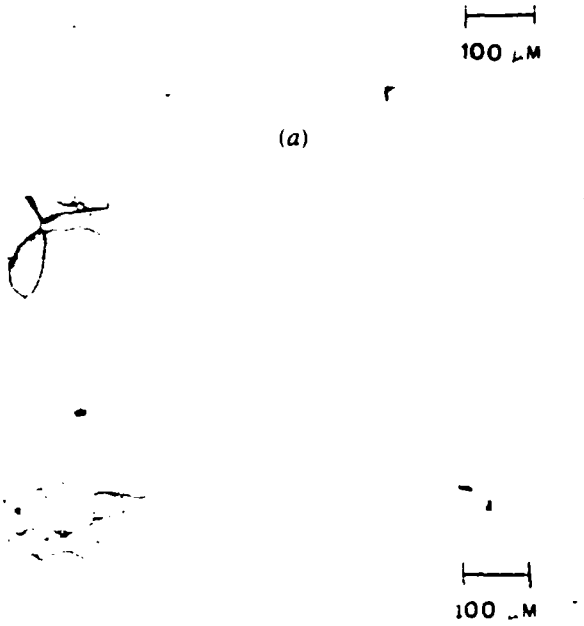

Fig. 3—Grain size of water quenched hypoperitectic alloys: (*a*) 0.57 and (*b*) 2.05 pct Fe.

seem to follow the continuation of the curve for the hypoperitectic region. This trend will become more obvious when the results of the samples solidified while levitated are considered later. In addition, the grain size of the hyperperitectic samples had greater uniformity as compared to the hypoperitectic samples.

The effect of iron content on the mean grain size of the alloys solidified in the levitated state is shown in Figure 6. For the hypoperitectic alloys, the grain size showed the same trend as the water quenched samples. It should be noted that the cooling rate during solidification of the levitated samples was around 20 °C per second, as compared with about 500 °C per second for the water quenched samples.

In alloys containing greater than 2.8 pct Fe, the grain size of the samples solidified in the levitated state was found to be insensitive to the iron concentration, as indicated in Figure 6. This can also be seen from the photomicrographs shown in Figure 7 for two samples containing 3.27 pct and 7.46 wt pct iron—in spite of the large difference in iron concentrations, the average grain size is the same in both

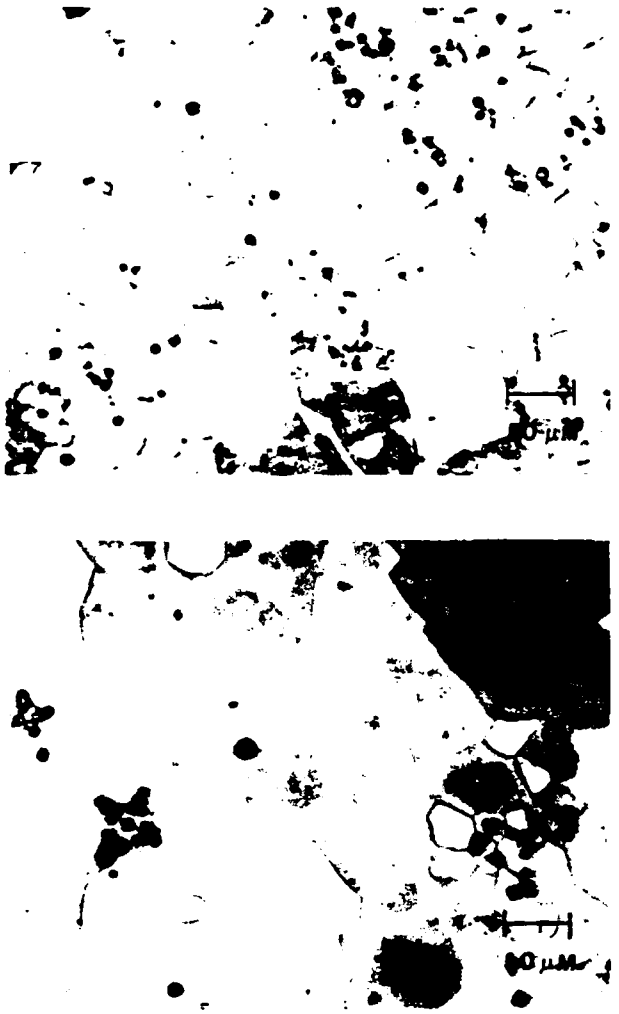

Fig. 4 — Microstructures of two samples with 2.8 pct Fe solidified in levitated state — note the difference in the grain size.

samples. At lower iron concentrations, the iron dendrites are small with only a few side branches. At larger concentrations, however, the dendrites have a well-developed dendritic structure consisting of numerous secondary, and in some cases, tertiary arms. It was also noted that primary dendrites had accumulated mostly near the surface of the samples. Solid state precipitates of iron, approximately 0.4 microns in diameter, were also seen in the copper matrix by SEM analysis. This is in contrast with the water quenched samples which showed no iron precipitates, indicating that the copper matrix was a supersaturated alpha solid solution.

IV. DISCUSSION

The results of the present investigation indicate that the addition of iron causes considerable grain refinement in copper, in agreement qualitatively with earlier studies.[18,19,20] In the earlier studies the effect of iron was studied on either multi-component commercial alloys or elements such as phosphorus were used to deoxidize the melt. In the present research, high purity materials were used, and the samples were levitation melted in an essentially oxygen-free atmosphere. The inherent advantages of this technique include noncontamination, melt homogeneity, and precise temperature, time, and atmospheric control. Because of these features, the present results most likely show the grain refining effects due to the iron additions only.

In the hypoperitectic region, the grain size in both sets of samples, quenched in water or solidified in the levitated state, decreased as the iron concentration was increased. In the hyperperitectic region, however, the grain size of the alloys solidified in the levitated state showed no dependence on the iron content, whereas those quenched from their liquidus showed a continued decrease as the iron content was increased. The two sets of data are compared in Figure 8.

In the hypoperitectic region, the grain refinement mechanism by the addition of iron can be discussed based on the amount of solute build-up ahead of the interface criterion, denoted as the "P" factor,[6] or the nucleation entropy criterion.[5] The calculated values of the nucleation entropy and the P factor at 1 wt pct Fe are $-4.322\ J \cdot mole^{-1} \cdot K^{-1}$ and 1.30, respectively. The thermodynamic values necessary for the calculations were obtained from the JANAF tables[21] and the phase diagram. Since these quantities increase with increasing the iron content, both criteria qualitatively explain the enhanced grain refinement with increased iron content. However, neither criterion can be used *a priori* to predict grain refinement capability of iron. This is due to the fact that the minimum value of the P factor or the nucleation entropy necessary for effective grain refinement is not yet well established. For aluminum binary alloys, it was shown that a P factor larger than about 20 was necessary to cause 80 pct reduction in the grain size.[6] At lower values, the grain size reduction was considerably lower. For the Cu-Fe system, even though the P factor is small, less than 2, the grain size reduction is larger than 90 pct.

As indicated earlier, the effectiveness of iron additions on the nucleation of the copper in the hyperperitectic region can be judged based on the amount of bulk supercooling attainable in the samples. Similar to other experiments,[17] it was observed that the bulk supercooling reduced drastically as iron concentration was increased. Youdelis[5] has attributed the reduction in the supercooling to the increased nucleation entropy with solute concentration.

In the hyperperitectic region, the grain refinement could possibly be due to either the growth restrictive nature of the peritectic reaction or the presence of iron primaries acting as heterogeneous nucleation sites. The disregistry between γ-iron and copper at the peritectic temperature is only 0.8 pct, indicating the potency of iron primaries in nucleating the copper phase. It was noted that no appreciable supercooling at the peritectic temperature was observed in the hyperperitectic alloys, which again indicates the effectiveness of iron in nucleating copper. This can be compared with the results of our experiments with Cu-Nb alloys where a supercooling of approximately 10 °C was observed at the peritectic temperature.[22] For Cu-Nb system, the overall lattice mismatch between (111) planes of copper and (110) planes of niobium is around 14.5 pct.

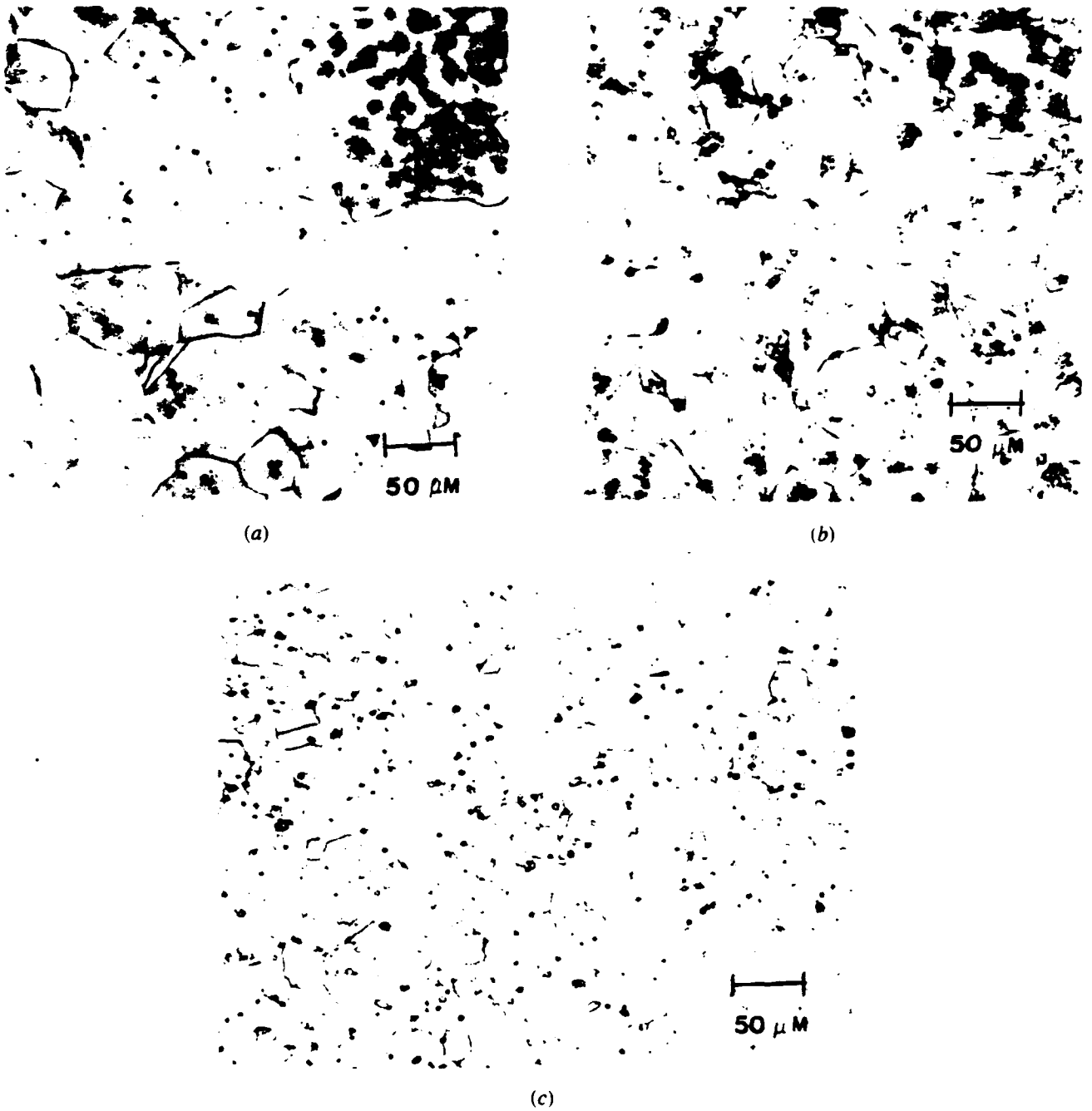

(a) (b) (c)

Fig. 5 — Effect of iron additions on the grain size of copper in water quenched hyperperitectic alloys: (*a*) 2.84, (*b*) 3.12, and (*c*) 4.06 wt pct Fe.

To compare the results of the water quenched samples with those solidified in the levitated state, two points must be taken into consideration: (1) the latter samples were solidified at a much lower cooling rate than the former ones (20 °C per second compared with 500 °C per second, respectively), and (2) the latter samples were solidified while being stirred by the electromagnetic field. Despite the lower cooling rates, the average grain size of the latter samples in the hypoperitectic region was comparable to that of the water quenched samples. The results indicate the beneficial effect of fluid flow on grain refinement in this region. In the hyperperitectic region, however, the grain size of the samples solidified in the levitated state was considerably larger than that of the water quenched samples. In fact, the grain size became insensitive to the iron content, indicating the detrimental effect of electromagnetic stirring. This is due to the fact that while stirring can cause dendrite fragmentation or remelting, it can also enhance coarsening and agglomeration of the nucleating particles. The first effect will result in grain refinement *via* grain multiplication, whereas the

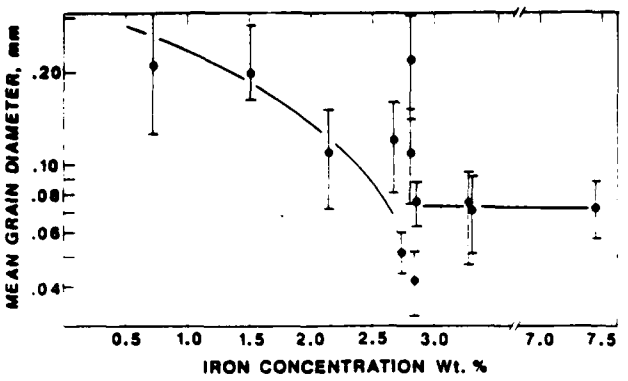

Fig. 6—Mean grain size as a function of iron content for copper-iron alloys quenched in water from 1000 °C.

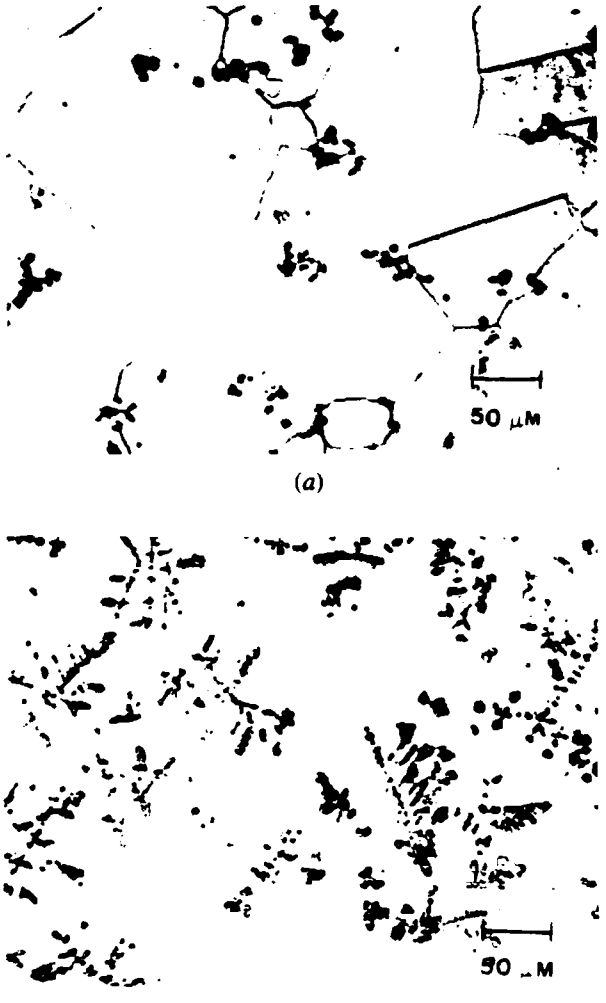

Fig. 7—The effect of iron addition on the grain size of hyperperitectic alloys solidified in the levitated state: (*a*) 3.27 and (*b*) 7.46 pct Fe.

second will reduce the number of heterogeneous nucleation sites. The relative importance of the two would depend on the alloy composition and cooling rate, as well as the flow conditions.

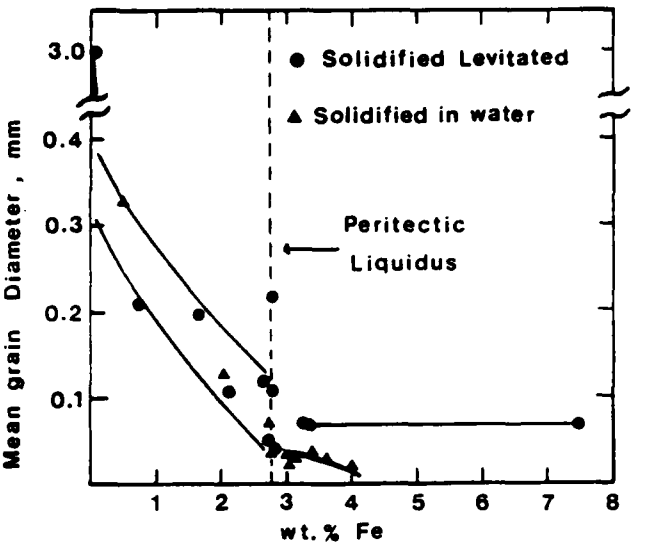

Fig. 8—The effects of cooling rate, stirring, and iron concentration on the mean grain size of copper iron alloys.

It is believed that in the hypoperitectic region, the grain multiplication mechanism has augmented the effect of iron in promoting grain refinement such that the grain size of the slowly-cooled samples were the same as the rapidly-cooled ones. In the hyperperitectic region, on the other hand, the increased fluid flow has caused appreciable coarsening and agglomeration of the primary iron phase, diminishing their effectiveness to nucleate the copper. The stirring also caused preferential accumulation of the iron primaries on the surface of the samples. The agglomeration phenomenon is similar to the commonly observed fading process, as a result of which the effectiveness of the inoculants is found to diminish as the metal is held in the liquid state. For conventional casting processes, the fading process occurs over a period of minutes. In the case of electromagnetic levitation, the increased fluid flow enhances the process appreciably.

V. CONCLUSIONS

The addition of iron in the range of 0.57 to 7.5 wt pct has been found to cause appreciable grain refinement in copper. In the hypoperitectic alloys, electromagnetic stirring enhances the grain refinement *via* the grain multiplication mechanism. In the hyperperitectic alloys, on the other hand, the stirring reduces the grain refining capability of iron by agglomerating the primary iron particles which act as heterogeneous nucleation sites for copper.

ACKNOWLEDGMENTS

The support of the Office of Naval Research (Contract No. N00014-81-k-0730), monitored by Dr. Bruce A. MacDonald, is gratefully acknowledged.

REFERENCES

1. G. J. Abbaschian and S. A. David: "Grain Refinement in Castings and Welds," Conf. Proceedings, St. Louis, Oct. 25-26, 1982, Pub. Met. Soc. AIME, 1983.
2. L. F. Mondolfo: in Reference 1, pp. 3-50.
3. P. B. Crosley, A. W. Douglas, and L. F. Mondolfo: Iron and Steel Inst. Pub. 119, 1967, pp. 10-17.
4. D. Turnbull and B. Vonnegut: *Ind. and Eng. Chem.*, 1952, vol. 44, pp. 1292-98.
5. W. V. Voudelis, *Metal Sci.*, Sept. 1979, pp. 540-43.
6. L. A. Tarshis, J. L. Walker, and J. W. Rutter: *Metall. Trans.*, 1971, vol. 2, pp. 2589-97.
7. F. A. Crossley and L. F. Mondolfo: *J. Metals*, 1951, vol. 3, pp. 1143-48.
8. L. Arnberg, L. Backerad, and H. Klang: in Reference 1, pp. 165-81.
9. A. H. Freeman and J. F. Wallace: *J. Metals*, Trans. AFS, 1957, vol. 65, pp. 578-89.
10. D. Spencer, R. Mehrabian, and M. C. Flemings: *Metall. Trans.*, 1972, vol. 3, p. 1925-32.
11. S. D. E. Ramati, G. J. Abbaschian, and R. Mehrabian: *Metall. Trans. B*, 1978, vol. 9B, pp. 241-45.
12. M. Gray, A. McLean, G. Weatherly, R. J. Simcoe, R. Hadden, and L. Beitelman: *ISSM*, April 1982, pp. 20-25.
13. G. Amaya, J. A. Patchett, and G. J. Abbaschian, In Reference 1, pp. 51-65.
14. G. J. Abbaschian and M. C. Flemings: *Metall. Trans. A*, 1983, vol. 14A, pp. 1147-57.
15. *Metals Handbook*, ASM, 1973, vol. 8, p. 293.
16. R. M. Kotschi and C. R. Loper Jr.: *AFS Trans.*, 1977, vol. 85, pp. 425-30.
17. R. J. Southin and G. M. Weston: *J. Aust. Inst. Metals*, 1973, vol. 18, pp. 74-81.
18. K. Iwase, J. Asato, and N. Nasu, Science Report Tohoku Imp. Univ., Honda Anniv. vol., 1936, pp. 652-69.
19. A. Cibula: *J. Inst. Metals*, 1953-54, vol. 82, pp. 513-24.
20. G. C. Gould, G. W. Form, and J. F. Wallace: *Modern Castings*, 1960, vol. 37, no. 5, pp. 144-52.
21. *JANAF Thermochemical Tables*, 2nd ed., National Standard Reference Edition, 1971.
22. G. J. Abbaschian: ONR Technical Report 2, Office of Naval Research, Contract N00014-81-K-0730, NR031-836, Oct. 1983.
23. El-Kaddah and J. Szekely: *Metall. Trans. B*, 1983, vol. 14B, pp. 401-10.

APPENDIX C

STRUCTURE AND TENSILE PROPERTIES OF A RAPIDLY SOLIDIFIED-HOT EXTRUDED Al-Li-Mg-Zr ALLOY

S. P. Abeln* and G. J. Abbaschian

Department of Materials Science and Engineering
University of Florida
Gainesville, Florida 32611

* presently at Rockwell International
Golden, Colorado 80401

ABSTRACT

Rapidly solidified Al-3%Li-5.5%Mg-0.2%Zr powder was hot extruded, and subjected to conventional precipitation heat treatment and thermomechanical processing. The tensile properties and microstructures resulting from different processes are contrasted. The material exhibited low ductility because of the shearable coherent strengthering phase, δ', and/or the presence of the precipitate free zones. It is shown that the ductility and toughness of the alloy can be significantly increased with the use of a cryogenic deformation process followed by a dispersion heat treatment. This new process completely changes the strengthening phase from δ' to finely dispersed Al_2LiMg and hence eliminates the inhomogeneous deformation associated with the conventional δ' strengthened material.

Introduction

Metallurgists have long been taxed with the problem of developing lighter and stronger alloys. One particular alloy system which has received much attention is the Al-Li system. Predictions by Materials and Marketing Specialists indicate that Al-Li alloys could replace all of the present 7xxx and 2xxx wrought aluminum alloys in aircraft structures by the 1990's (1). Lithium has been identified as the only alloying element (besides beryllium) which improves both the elastic modulus and density. The improvements are progressive and increase with increasing addditions of lithium up to 4 wt% (2). Concomitant with the property improvements with Li additions is a degredation of the ductility and toughness. The poor ductility has been attributed to strain localization caused by the precipitate free zones (PFZ) and/or shearable precipitates. Hence, recent alloy development programs have concentrated on modifying the structure of the alloy in order to change its deformation mechanism. Examples of this development include: 1) grain refinement, 2) the addition of solid solution strengtheners and co-precipitates, and 3) the addition of dispersoid forming elements (3-4). To date, only small improvements in ductility have been recognized, and it appears the trend is to reduce the amount of Li addition to improve the ductility, as evidenced by recent alloys introduced to the market. It is the purpose of this paper to present a novel thermomechanical process which would allow for increasing additions of Lithium, and yet improve the ductility and toughness significantly.

Experimental Procedure

Rapidly solidified powder of composition Al-3%Li-5.5%Mg-0.2%Zr, produced by the inert centrifugal gas atomization process, was characterized and subsequently consolidated in vacuum by hot extrusion. The extrusion process was accomplished by transferring the as-received material, packed in an inert atmosphere, into a 5cm diameter aluminum can in an argon atmosphere dry box. The can was then welded shut under vacuum, and the entire container was extruded at 400°C with an extrusion ratio of 24. The hot extruded material was then hot rolled under various conditions, as discussed later. Tensile specimens were machined to 1 inch gage length and 0.25 inch wide, and subsequentlly pulled with an Instron testing machine. The specimen thickness, depending on the thermomechanical processing, ranged from 0.08 to 0.15 in. The modulus of elasticity was determined by an ultrasonic technique. The microstructural response to heat treatment and deformation was examined using light microscopy, scanning electron microscopy (SEM), and transmission electron microscopy (TEM). Etchants used to reveal the grain structure and second phases were an anodic etch consisting of 34.6 ml HF, 13.6 gms boric acid, and water to make 1 litre (operated at 20 volts), and Keller's reagent, respectively. Thin films were prepared using a double jet polishing machine (Tenupol). The electrolyte for thinning, 25% HNO_3 and 75% methonal, was cooled to -20°C, and thinning was conducted at a potential difference of 15 volts.

Experimental Results

Microstructures

The general size and shape of the as received powder are shown by the SEM photomicrographs in Figure 1. Particles were predominantly spherical with an average size of approxiamtely 100 μm. Microexamination of sections through the powder revealed a uniform dendritic structure throughout with some interdendritic shrinkage. The average secondary dendrite arm spacing

was approximately 1.5μm. This extrapolated on a DAS vs. cooling rate plot for Al(4) to 10^5 -10^6°C/sec as the effective cooling rate. A substantial fraction of the particles also contained smaller imbedded particles and exhibited extensive interdendritic cracking, Figure 1c. In each instance of extensive interdendritic cracking, deformation of the powder particle was evident, possibly as a result of the droplet impact with the outer wall of the atomization unit during solidification. Other larger particles, which showed no deformation, exhibited some interdendritic cracking, caused by the solidification shrinkage or hot tears.

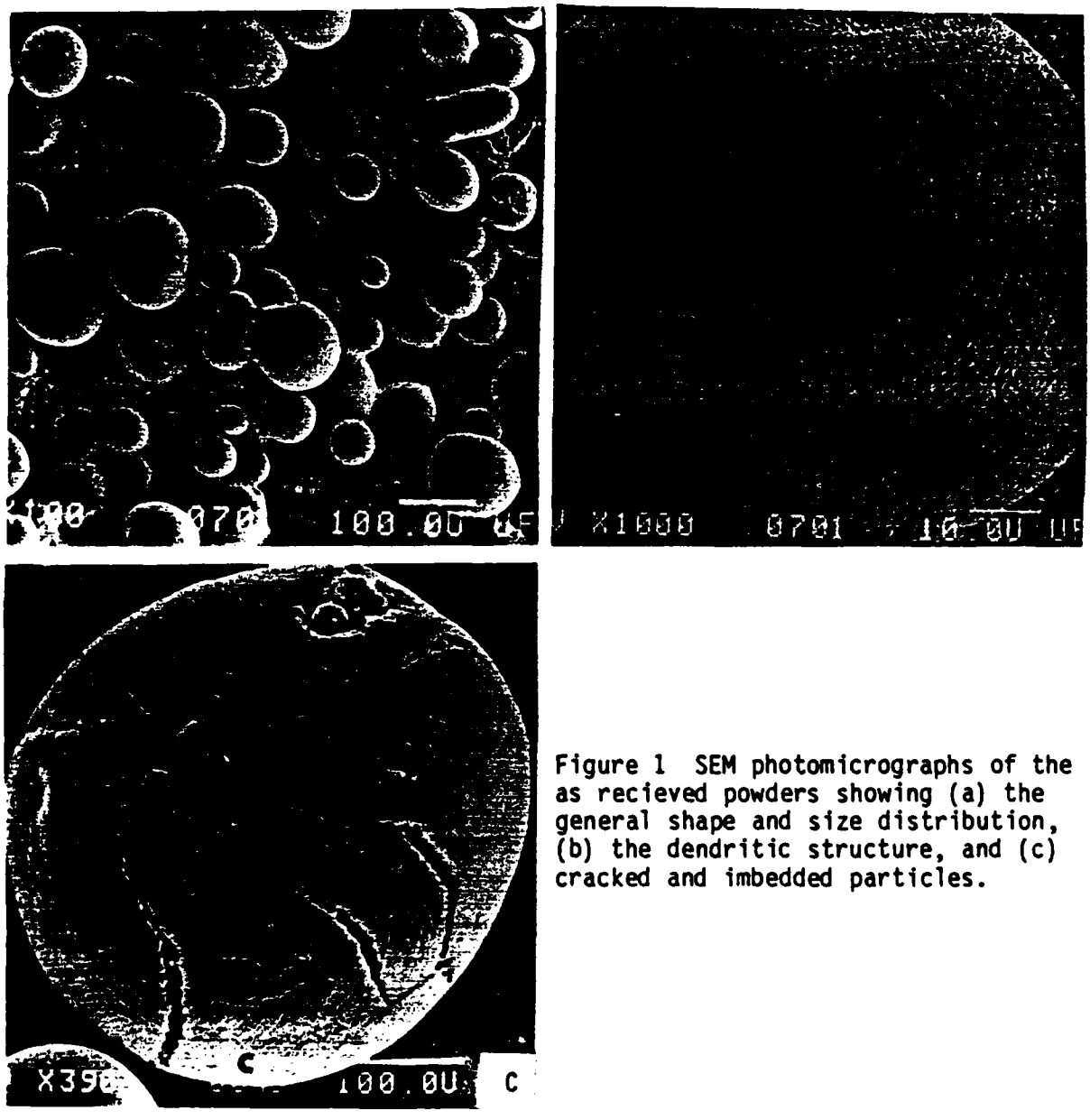

Figure 1 SEM photomicrographs of the as recieved powders showing (a) the general shape and size distribution, (b) the dendritic structure, and (c) cracked and imbedded particles.

An SEM photomicrograph of a polished and etched cross section of the as-extruded structure is shown in Figure 2a, where pitting caused by the Keller's reagent which attacks the Al_2LiMg phase can also be seen. The structure consists of a uniform dispersion of Al_2LiMg in an α-matrix. The effect of solution heat treatment at 450, 500, 525, and 535°C on the structure of the extruded material is shown in Figures 2b-2d. It was found that solutionizing at 450°C for 1/2 hour had little effect on the as-extruded structure (Figure 2b). Increasing the solutionizing temperature to 500°C resulted in the dissolution of Al_2LiMg and noticeable preferential retainment of Al_2LiMg precipitates at the prior particle boundaries (Figure 2c).

Nevertheless, appreciable grain growth was still not evident, possibly owing to the extensive amount of Al_2LiMg remaining. Solutionizing the material at 525°C for 1/2 hour, on the other hand, resulted in appreciable grain growth, where each grain contained numerous powder particles (Figure 2d). The powders apparently retained a subgrain structure within the coarsened grains, as evidenced by their contrast differences under polarized light. The maximum solution temperature was determined to be 525°C. Material solutionized above this temperature exhibited extensive incipient melting of the second phase constituents at the grain boundaries. For example, at 535°C the powder structure was completely annihilated in 1/2 hour and large recrystallized grains in the range of 100-500μm had formed.

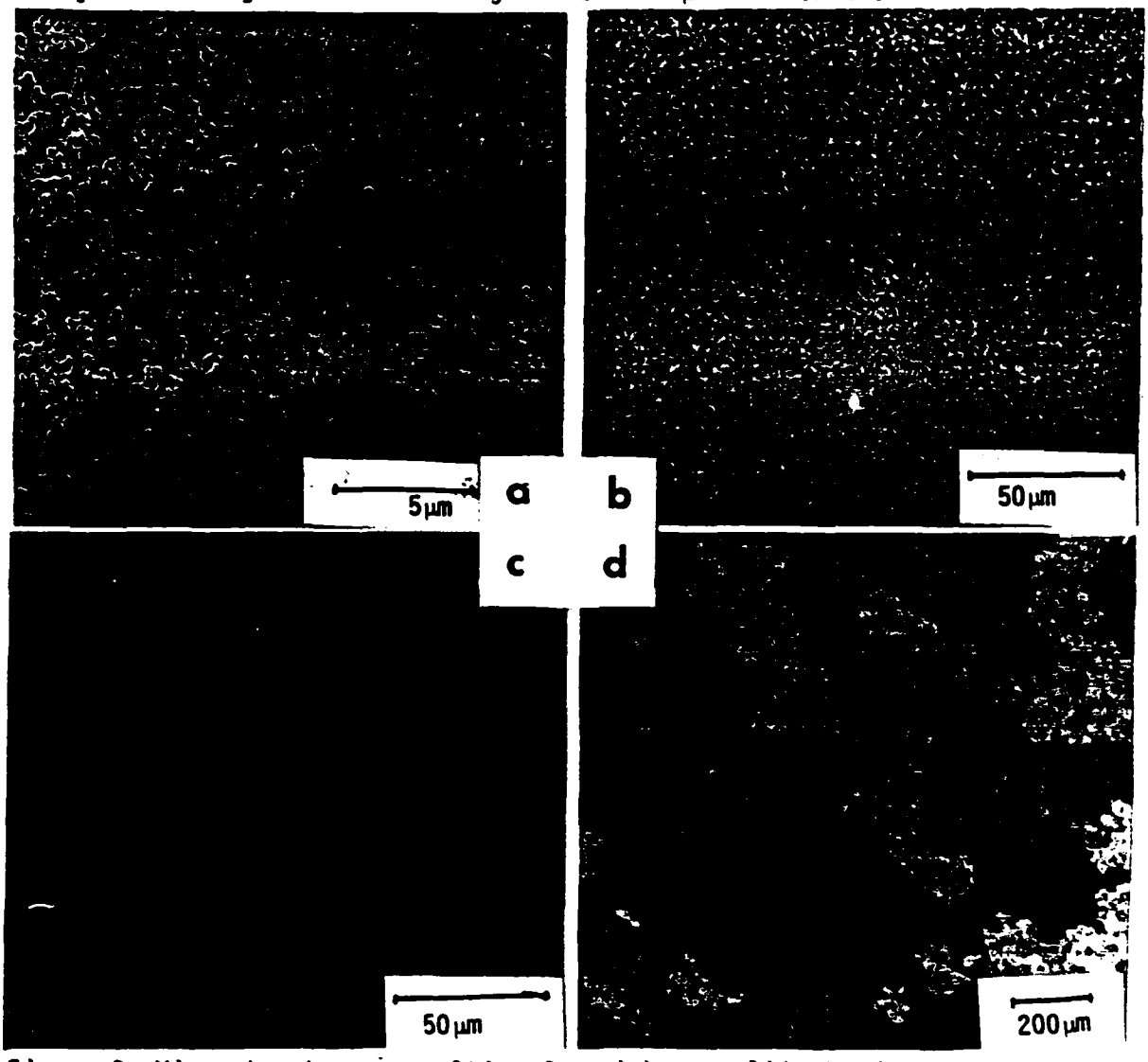

Figure 2 Microstructures resulting from (a) consolidation by hot extrusion, (b) solutionizing for 1/2 hour at 450°C, (c) at 500°C, and (d) at 525°C.

The solutionized and water quenched samples were aged at 200°C for various times until overaging. The precipitation and coarsening behavior of the metastable $Al_3Li(\delta')$ was documented with TEM and hardness measurements. A composite of TEM Photomicrographs showing δ' after various aging times is shown in Figure 3. The photomicrographs were taken in dark field while imaging the superlattice reflections. The solutionized and water quenched samples showed a high volume fraction of δ' (see Figure 3a) indicating that the formation of δ' was not completely supressed by water quenching. The presence of numerous antiphase boundaries or stacking faults was also evident. As aging began, coarsening of δ' took place. In some

cases the coarsening was found to be by link-up or coalescence of δ′ which resulted in irregularly shaped zones (see Figures 3b, c, & d). The stacking faults associated with δ′ were also annihilated, which might partially account for the increase in hardness during aging. Beyond the peak aged condition, the δ′ became larger and more spherical as shown in Figures 3d and 3e for 30 to 50 hours of aging, respectively. The volume fraction also decreased with overaging, owing to the nucleation and growth of the

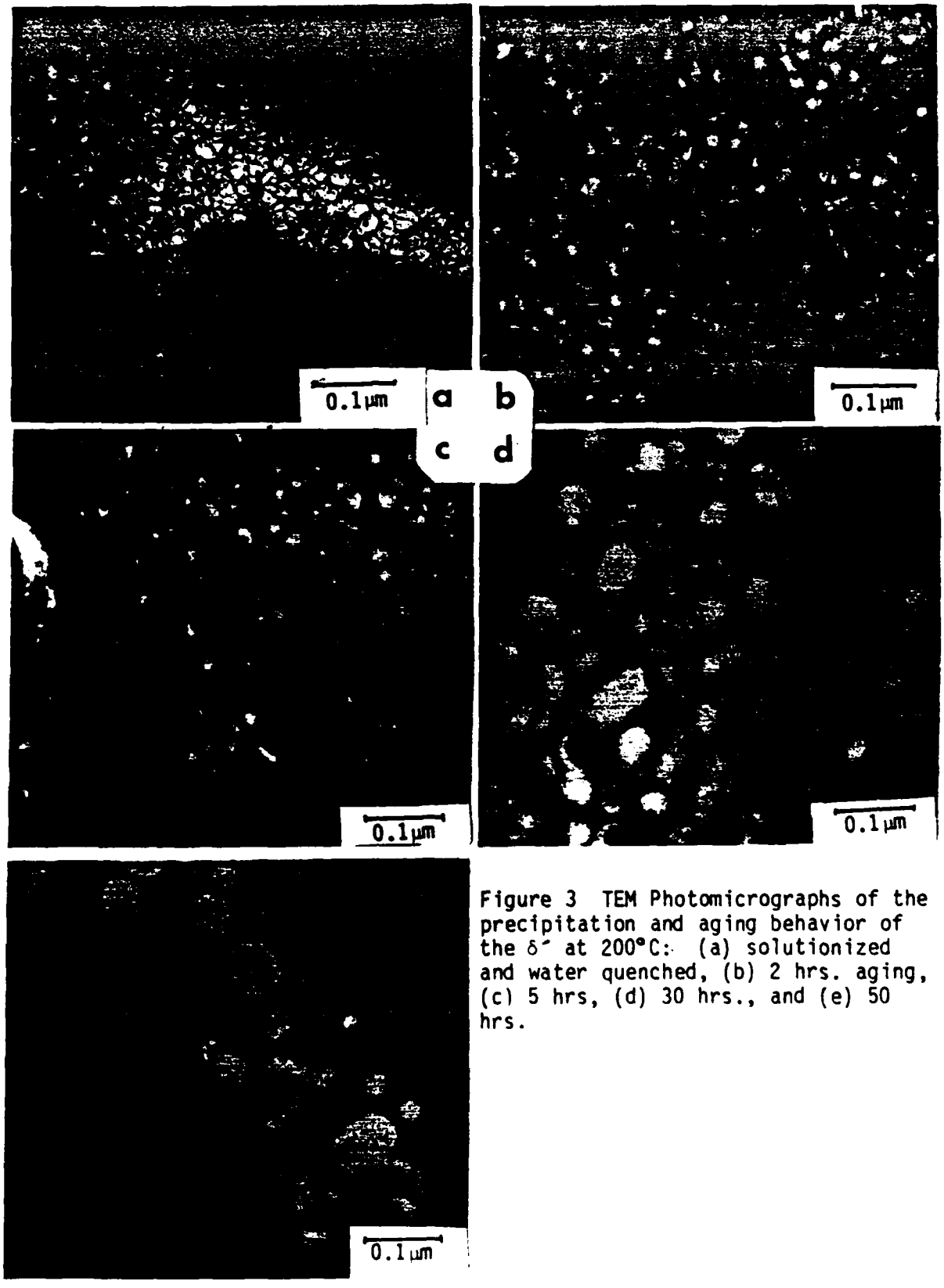

Figure 3 TEM Photomicrographs of the precipitation and aging behavior of the δ′ at 200°C: (a) solutionized and water quenched, (b) 2 hrs. aging, (c) 5 hrs, (d) 30 hrs., and (e) 50 hrs.

intermediate Al_2LiMg phase. THe Al_2LiMg was observed to preside nonuniformly within the matrix or at the grain boundaries, indicating heterogeneous nucleation of the phase.

Rolling

The response of the solutionized and water quenched material to rolling was examined at room temperature, 300 and 450°C. The maximum reduction at room temperature was approximately 15% before fracturing occurred. Fracturing occurred at 45° to the principal stress axis, typical of materials deforming by planar slip. When the material was rolled at 300°C, within the δ' precipitation field, only approximately 5% R.A. was possible before fracturing occurred by alligatoring and/or axial splitting. It is believed that the very low ductility associated with rolling at this temperature range could be attributed to dynamic strain aging (6) or a mechanism involving the cross slip of the leading partial dislocations and subsequent pinning of the two separated partial dislocations on different planes(7). Samples rolled at 450°C were able to be substantially reduced without fracturing if large single pass reductions and excessive exposure to the high temperature were avoided.

Cryogenic Processing

In the course of processing this alloy, a number of problems associated with rolling of the material were encountered. These included surface and edge cracking, and microcracking which drastically deteriorated the mechanical properties of the final product. The problems existed even when the solutionized and water quenched samples were rolled at room temperature by less than 15% RA. These problems, however, were eliminated when the material was rolled at a cryogenic temperature. To achieve this, the solutionized-water quenched material was submerged in liquid nitrogen, and subsequently rolled. Samples rolled at cryogenic temperatures exhibited excellent ductility and were capable of at least 35% RA prior to fracturing. The microstructure of the cryo-rolled material is contrasted with that of the hot rolled material in Figures 4a and b, respectively.

In addition to the enhanced formability, the cryo-rolled material exhibited a unique microstructural feature of what appears to be deformation bands or twins. At this time conclusive x-ray diffraction evidence is not

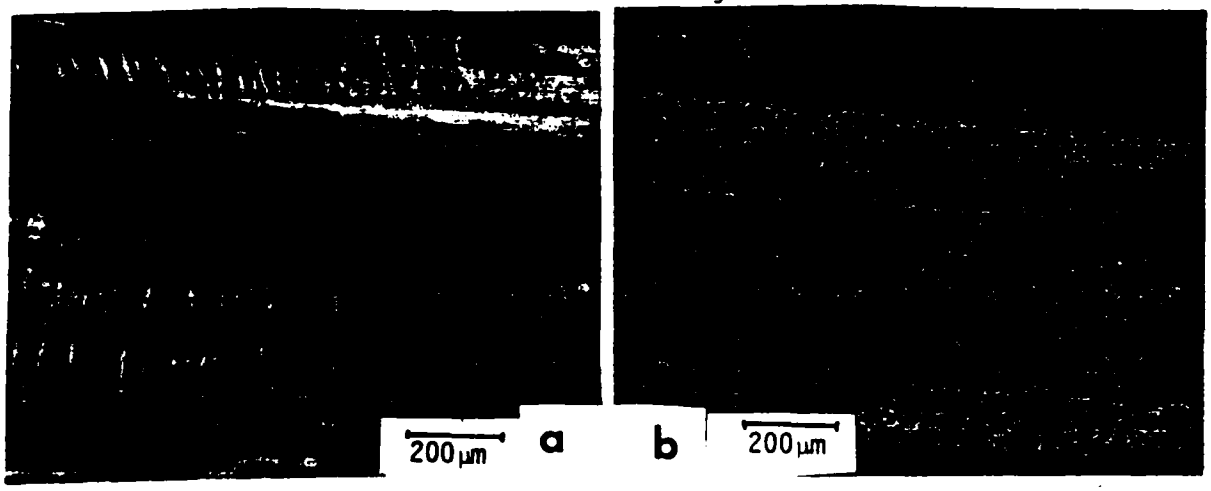

Figure 4 Optical Photomicrographs using polarized light, showing (a) the cryogenically rolled structure, and (b) the as hot rolled structure. Note the evidence of possible twins in the cryo-rolled material.

available to determine whether the microstructural feature is due to twinning or deformation bands. Nevertheless, three observations, in addition to the metallographic evidence, were made which support twinning over deformation bands. First, the degree of disorder in the δ' precipitate state was critical to the occurrence of the microstructural feature. Any material which was aged, resulting in a significant ordering of the $L1_2$ material, did not twin and fractured early. The destruction of the A-B type bonds during twin formation apparently presents an insurmountable energy barrier thus causing fracture. A similar structural dependence or degree of ordering on the formation of twins has also been observed in FeAl alloys (9). Second, there was a critical strain required for the onset of the microstructural feature, generally 15% RA. Third, reductions in excess of about 15% caused the distinctive ping normally associated with twin formation. Because of the above reasons, we believe the microstructural feature of the cryo-rolled material is due most likely to twinning. It should be noted it is commonly believed that deformation twinning does not occur in FCC materials. Notwithstanding, twinning has been clearly documented in several FCC materials under various conditions (10-13).

The twinning also provides a rationale for the extended ductility because the twinned or reoriented structure can provide new orientations favorable for continued slip, and hence more uniform deformation. Also twinning would effectively decrease the grain size resulting in an increased work hardening rate and therefore a higher uniform strain before instability.

When the cryo-rolled material was aged below the δ' solvus, its precipitation morphology was similar to that of the conventionally rolled materials. On the other hand, in contrast with the latter samples, precipitation heat treatment of the cryo-rolled samples at slightly above the δ' solvus resulted in the formation of fine and homogeneously distributed Al_2LiMg precipitates. TEM photomicrographs of the structures generated by cryo-rolling, followed by precipitation at 325°C for 30 minutes, and at 350°C for 10 minutes are shown in Figure 5a and b, respectively. The samples were reduced 35% at the cryogenic temperature. The uniform and high density of the Al_2LiMg can be clearly seen in these figures. The Al_2LiMg precipitates were generally irregular in shape, and had an average diameter less than 1 μm. A similar treatment was done on samples with 50%RA. The results indicated that there was little difference between the size and distribution of Al_2LiMg between 35% and 50% RA. Therefore, 35% RA was considered sufficient to produce a uniform defect structure and hence uniform distribution of Al_2LiMg. Also evident, as shown in Figure 5c, was a polygonized dislocation substructure between the Al_2LiMg precipitates.

Mechanical Properties

The elastic modulus (E), shear modules (G), and poison's ratio ν of the as extruded structure, as determined by an ultrasonic technique, were:

$$G = 4.45 \times 10^6 \text{ psi}$$
$$E = 11.4 \times 10^6 \text{ psi}$$
$$\upsilon = 0.278$$

The hardness vs aging time data, determined upon aging at 175, 200, 225, 250, and 275°C, are shown in Figure 6. Table I lists the average yield strength (YS), ultimate tensile strength (UTS) and elongation to fracture of the samples processed under the specified techniques. Initially, a baseline for the standard precipitation heat treatment was conducted for aging times of 5, 24, 50, and 72 hours at 200°C. Examination of the tensile results

showed that the strength values varied considerably from underaged through overaged, but the ductility remained consistently low. The maximum average ductility was about 2.8% when the material was overaged at 200°C for 50 hours. It was also noted that the peak hardness aging time did not correspond to the peak tensile strength aging time. This may be due to the difference in the amount of strain for the two testing techniques (the hardness indentation puts a high amount of local strain, whereas the tensile tests are limited in the amount of strain).

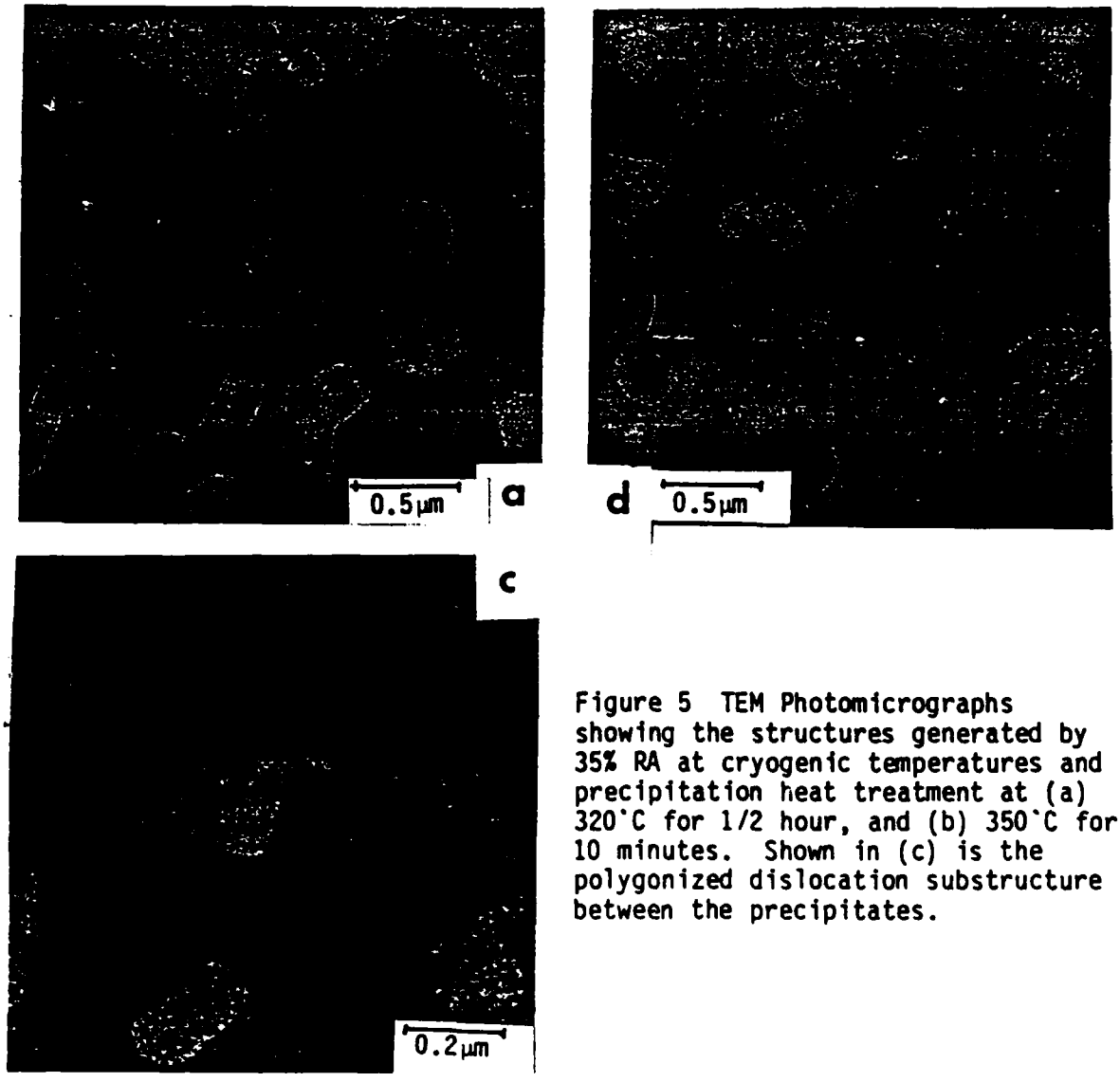

Figure 5 TEM Photomicrographs showing the structures generated by 35% RA at cryogenic temperatures and precipitation heat treatment at (a) 320°C for 1/2 hour, and (b) 350°C for 10 minutes. Shown in (c) is the polygonized dislocation substructure between the precipitates.

The effects of different cyro-mechanical processes and dispersion strengthening with the equilibrium Al_2LiMg phase on the mechanical properties are also shown in Table I. Among the cryo-rolled samples, the effect of the amount of the cyro-rolling on the properties is very small. This can be seen by comparing sample F and G which show only an approximate 2 ksi drop in YS and UTS for 20% RA as opposed to 35% RA. The elongation to fracture is also similar for the two samples. The effect of time at the precipitation temperature is also minor, with only a slight variance in elongation (compare samples F and H, or G and I). However, the precipitation temperature has a pronounced effect on the properties (compare sample K to samples F-J). The results of sample K show that the yield strength and UTS of the cryo-rolled material can be improved significantly by precipitation hardening below the δ' solvus. However, the process reduces the ductility to that of the peak-aged samples.

Comparison of mechanical properties of the Cryo-mechanically processed samples to the conventionally peak aged samples shows comparable UTS and a better than 2x improvement in elongation to fracture or ductility. The yield strength of the cryo-rolled samples is lower than that of the samples aged 24 hours, but higher than that of the samples aged 50 hours. All cryo-mechanically processed samples, except J and K, show the considerable improvement in ductility.

To further examine the effect of deformation at cryogenic temperatures, the material was rolled at room temperature to 10% RA and dispersion heat treated at 350°C for 10 minutes. The tensile results (Sample E) show a decrease in Y.S. (8 ksi), UTS (4 ksi) and a slight increase in elongation when compared to the cryo-mechanically rolled material.

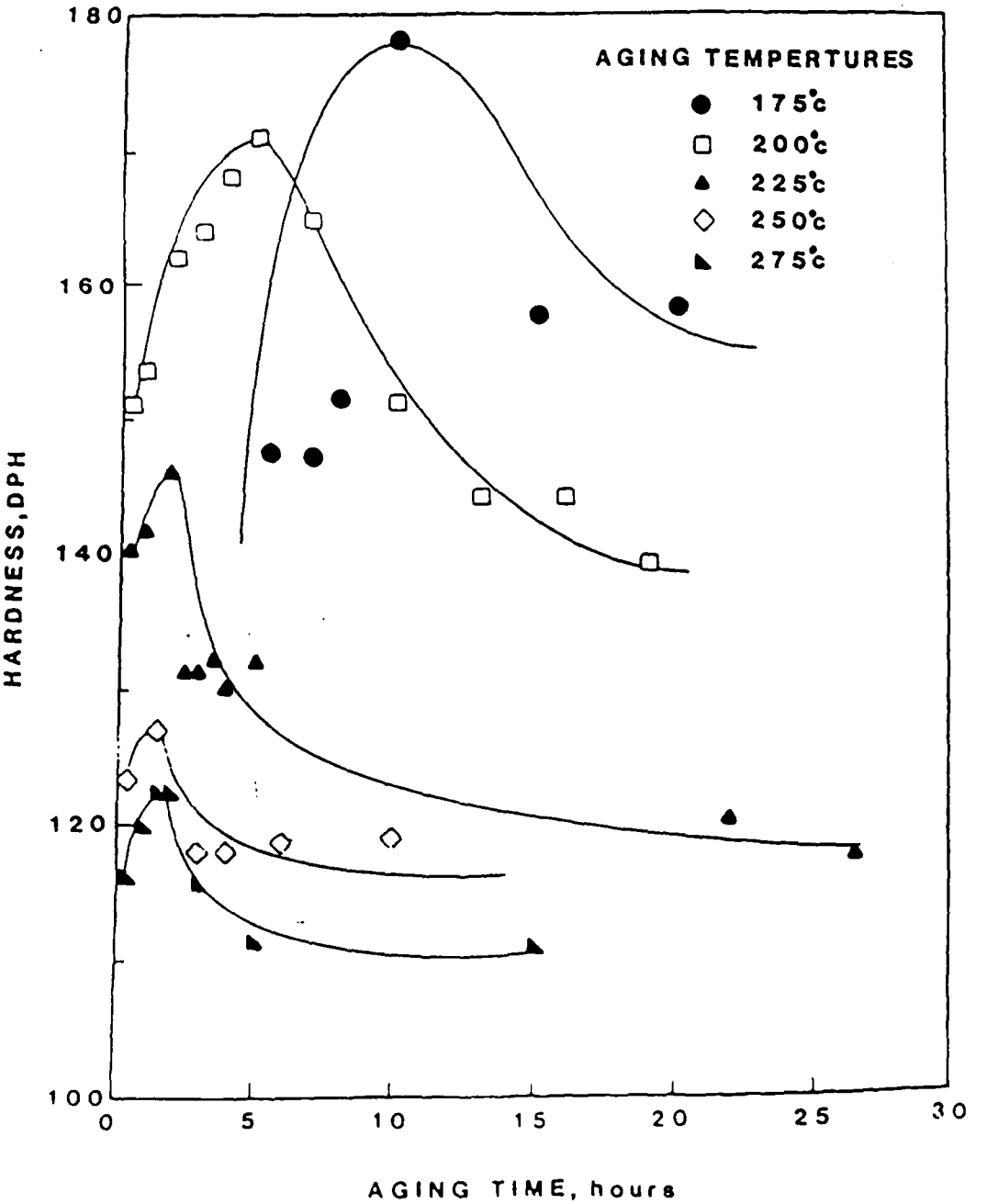

Figure 6 Hardness vs aging time at 175, 200, 225, 250 and 275°C.

Discussion

The cryo-mechanical processing examined in the course of this research has drastically changed the microstructure from that of the conventional δ' precipitation strengthened processes to a dispersion and dislocation sub-structure strengthened microstructure. The manifestations of this new microstructure will be discussed and contrasted with the conventional process.

The microstructural results of the δ' strengthened alloy presented earlier indicated that the δ' remains coherent during aging and the Al_2LiMg nucleates heterogeneously and nonuniformly upon overaging. All structures which contained δ', whether underaged or overaged, possessed brittle characteristics. These results again confirm early reports that the coherent and shearable nature of the δ' precipitate promotes heterogeneous planar slip, and hence low ductility and toughness. In the overaged condition, the problem is compounded by the existance of PFZ near the grain boundaries.

An alternative method of strengthening is to use the Al_2LiMg phase particles as a dispersion strenthener. The semicoherent nature of the Al_2LiMg phase should render it impenetrable to dislocations and therefore, provide for homogeneous deformation and enhanced ductility. Conventional processing (i.e., solution and precipitation heat treatment) produces a nonuniform distribution of Al_2LiMg, due to its heterogeneous nucleation. On the other hand, the high defect density associated with uniform deformation at cryogenic temperatures provided extensive sites for the nucleation of Al_2LiMg.

The most significant benefit resulting from the cyro-processing is the better than 2x improvement in ductility, with comparable UTS and a slight loss of Y.S. The extensive increase in ductility more than offsets the decrease in Y.S., and provides improved toughness also. Figure 7 shows a comparison of the toughness of samples B and F. The area under the σ-E curve shows the improvement in toughness for the Cryo-mechanical process.

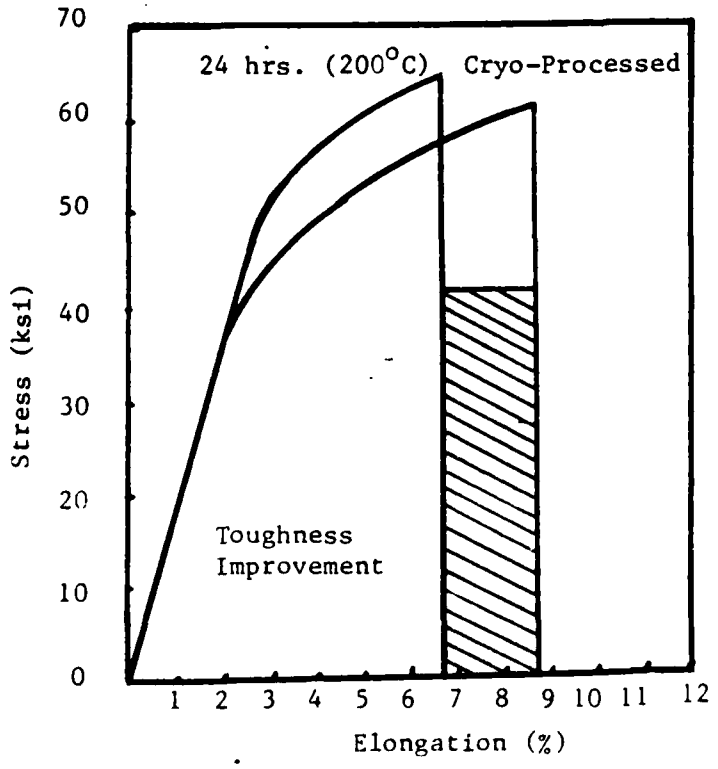

Figure 7 Stress-strain curves showing the toughness improvement by the cryo-mechanical processing compared to the conventional precipitation heat treatment.

The increased ductility associated with cryo-deformation might be due to twinning. However, more experiments are necessary to verify this. It is believed that the reduction in temperature may have caused a reduction in stacking fault energy (SFE) since twin formation requires a low SFE, or possibly raised the flow stress for slip such that the critical twinning stress was reached.

It should be noted that the alloy studied in this research was designed for δ' strengthening. It is believed that the alloy composition can be modified to improve the results of the cryo-processing. For example, the Li content can be further increased, which would result in (1) an increase in the volume fraction of Al_2LiMg leading to an increase in strength, (2) density reduction, and (3) modulus increase. In addition, if Li decreases the stacking fault energy of Al, increased additions of Li could result in a further reduction in SFE and increased twinning, thereby providing greater enhancement of the uniform elongation. Other alloying elements may be added to possibly co-precipitate with Al_2LiMg.

When material requirements for aircraft structures are considered, it is necessary to optimize strength along with toughness, FCP, and SCC. Generally, improvements in ductility and toughness, when using second phases, require a compromise in strength. The principle controlling parameters are particle size, shape, and deformability (14). Hence, it is the properties of the second phase chosen which will give the optimum strength and ductility. As such, there are two limits between which second phases should be chosen in order to avoid: 1) brittle particles and cracking during deformation, and 2) easy shearing of particles and the resultant heterogeneous planar slip. The cryo-mechanical process eliminates the problem of particle cutting and heterogeneous planar slip. Although the ductility of the Al_2LiMg is unknown, cracking was not observed in any of the SEM examinations of the fractures, and it may be inferred that the second phase (Al_2LiMg) does not have brittle characteristics.

Conclusions

Rapidly solidified powder of composition Al-3%Li-5.5%Mg-0.2%Zr, made by an inert centrifugal gas atomization process, was characterized and subsequently consolidated by hot extrusion. The response of the consolidated material to solution and precipitation heat treatments, and rolling deformation was examined using light, scanning electron, and transmission electron microscopy. The results indicated that the material exhibited low ductility, caused by the shearable nature of the coherent strengthening phase, δ' (Al_3Li). In the course of this study, a unique process for dispersion strengthening of the alloy by Al_2LiMg precipitates was utilized to improve the ductility and toughness. The technique involved cryogenic forming of the solutionized material, followed by a precipitation heat treatment above the δ' solvus. The tensile properties resulting from this process when compared with those of the conventional age hardening process showed a 2x improvement in ductility, comparable UTS, and a slight reduction in YS.

Acknowledgment

Partial support of this research by the Office of Naval Research, under project No. N00014-81-K-0730, is gratefully acknowledged. The Scientific Officer of the project was Dr. Bruce A. MacDonald. The authors also acknowledge the cooperation of Art Cox and Jim Simon of Pratt and Whitney for donating the powder and some of the extrusions.

References:

1. Chandler H. E., "New Aluminum Alloys Sighted on the Horizon", Materials Engineering, June 1984, pp. 32-35.

2. T. H. Sanders Jr., E. A. Starke Jr., "New Approaches to Alloy Development in the Al-Li System", J. Metals, Aug. 1981, pp. 24-33.

3. A. Gysler, R. Crooks, E. A. Starke Jr., "A Comparison of Microstructure and Tensile Properties of P/M and I/M Al-Li-X Alloys" in Aluminum-Lithium Alloys", Conf. Proc. TMS-AIME, Warrendale Pennsylvania, May, 1981, pp. 263-291.

4. F. W. Gayle, "Alloying Additions and Property Modification in Al-Li-X Alloys", ibid, pp. 119-139.

5. M. C. Flemings, Solidification Processing, McGraw-Hill, New York, N. Y., 1974, p. 150.

6. R. E. Reed-Hill, Tuling Zhu, "A Model for the Flow Stress and Strain Rate Sensitivity in a Refractory Metal", High Temp. Mats. and Processes, 6 (1 and 2) (1984) pp. 93-117.

7. M. Tamura, T. Mori, T. Nakamura, "Plastic Deformation of Al-Li Single Crystals Containing Al_3Li Particles", Trans. Jap. Insti. Met., 180 (1984) p. 245.

8. R. W. Cahn, J. A. Coll, "Twinning in Iron-Aluminum Alloys", ACTA Met. 9 (1961) pp 138-148.

9. J. A. Venables, "Deformation Twinning in FCC Metals", in Deformation Twinning, Met. Soc. Conf. Gainesville, Florida, March 1963, pp 77-111.

10. H. Zuzuki, C. J. Barrett, "Deformation Twinning in Metals and Alloys", ACTA Met., 6 (March 1958) pp. 156-164.

11. S. Mahajan, D. E. Williams, "Deformation Twinning in Metals and Alloys", INT. MET. Reviews, 18 (1973) pp. 43-61.

12. P. R. Thornton, T. E. Mitchell, "Deformation Twinning in Alloys at Low Temperature", Phil. Mag. 7 (1962) pp. 361-375.

13. S. Krishnamurthy, K. Qian, R. E. Reed-Hill, "Effects of Deformation Twinning on the Stress-Strain Curves of Low Stacking Fault Energy Face-Centered Cubic Alloys", in Pratical Applications of Quantitative Metallography, ASTM Pub. No. 839, pp. 41-64.

14. R. F. Decker, Alloy Design Using 2nd Phases, Met. Trans., 9 (1973) pp. 2495-2518.

Table I
Tensile properties of an Al-3%Li-5.5%Mg-0.2%Zr alloy processed by different techniques*

Sample Desig.	Conventional Process**	No. of Samples	Y.S. (Ksi) Average (Range)	T.S. (Ksi) Average (Range)	Elongation (%) Average (Range)
A	Aged at 200°C for 5 hours	2	34.5 (29.3-39.7)	48.5 (43.1-53.9)	2.7 (2.2-3.2)
B	Aged at 200°C for 24 hours	2	48.7 (40.0-57.4)	65.2 (59.1-71.3)	2.2 (2.0-2.4)
C	Aged at 200°C for 50 hours	3	32.5 (37.0-40.9)	71.4 (63.8-77.2)	2.8 (2.0-3.8)
D	Aged at 200°C for 72 hours	2	23.7 (20.8-26.7)	45.5 (41.6-49.4)	2.5 (2.2-2.8)
	Conventional Cold Rolling				
E	10% cold roll (R.T.) and precipitation heat treated at 350°C for 10 min.	3	29.2 (29.3-30.2)	57.1 (55.6-59.2)	6.0 (5.2-7.3)
	Cryo-Rolling ‡				
F	35% cryo-rolled and precipitation heat treated at 350°C for 10 min.	7	37.7 (35.6-40.0)	61.3 (59.4-64.1)	5.4 (4.0-6.2)
G	20% cryo-rolled and precipitation heat treated at 350°C for 10 min.	4	35.3 (34.8-55.5)	59.3 (54.8-61.7)	5.5 (3.5-6.5)
H	35% cryo-rolled and precipitation heat treated at 350°C for 5 min.	2	38.7 (38.1-39.4)	60.8 (60.4-61.2)	4.4 (4.0-4.9)
I	20% cryo-rolled and precipitation heat treated at 350°C for 5min.	2	35.3 (34.4-36.3)	58.8 (57.0-60.6)	4.9 (4.6-5.2)
J	20% cryo-rolled and precipitation heat treated at 350°C for 10 min plus 5 hrs at 200°C	3	33.8 (33.5-34.0)	56.2 (54.7-58.6)	3.2 (2.8-3.8)
K	35% cryo-rolled and precipitation heat treated at 200°C for 5 hours	3	53.8 (52.4-55.2)	67.5 (65.7-70.9)	1.7 (1.2-2.3)

* For samples with 1 in. gage length, and 0.11 x 0.255 in. cross section.
** The samples were hot extruded, hot rolled and solutionized prior to the specified processing.
‡ The as-extruded material was solutionized and water quenched prior to the specified processing.

APPENDIX D

Refining of Niobium by Levitation Melting Technique

R.I. Asfahani, D.S. Shahapurkar, Y.V. Murty, J.A. Patchett and G.J. Abbaschian

SUMMARY

The refining behavior of niobium, produced by an aluminothermic reduction reaction of Nb_2O_5, was studied using an electromagnetic levitation and melting technique. Under experimental conditions, significant refinement of niobium thermite occurred during levitation melting. Residence time plays a significant role in the refining process, and the refining kinetics, during levitation melting, correlate well with the approximate equations for desorption of nitrogen and carbon. The purity of the levitation-melted product is compared to that of niobium processed by the conventional EB drip-melting process.

INTRODUCTION

Although high-purity niobium (Nb) is available in commercial quantities for chemical, aerospace, and electronic applications, very little is known about its purification mechanisms during processing. Electron-beam remelting techniques,[1] including continuous drip melting and cold hearth melting (in water-cooled copper crucible), and zone refining,[2] are by far the well-established commercial techniques for processing Nb. The latter technique, however, is only used for very specific small-scale applications. A schematic of the EB drip melting process, most widely used in refining refractory metals, is shown in Figure 1, along with a commercial scale 1200 kW EB melting furnace used at KBI (a division of Cabot Corporation) in refining Ta, Nb, and their alloys containing Ti, W, Mo, and Hf.

During EB melting, refining occurs through vacuum evaporation of volatile metallic or non-metallic impurities. The initial refining starts with EB drip melting of a consolidated charge (fed either horizontally or vertically) at a pressure of roughly 10^{-2} Pa. The molten metal is solidified in a water-cooled crucible and the cast ingot is slowly withdrawn at a rate proportional to the melt rate. The final refining is achieved using single or multiple remelts by lowering the consumable ingot charge in the EB furnace to produce a homogeneous ingot with a smooth surface finish. The variables that control the refining characteristics include the vacuum level, the effective surface area exposed to the ambient furnace atmosphere, the melt superheat, and the fluid flow pattern within the melt pool.

In EB drip melting, the refining takes place by vacuum evaporation during: (a) melting, (b) dripping of the droplet, and (c) solidification. A similar mode of refining exists in the hearth melting process. One essential difference, however, is the presence of a hearth where the consumable electrode is melted to form a shallow melt pool which offers more surface area for evaporating volatile elements. It also gives more residence time for non-metallic impurities to reach the surface for subsequent removal by gravity separation.

Existing bulk electron-beam melting techniques do not allow precise control of residence time and temperature distribution within the molten pool to a degree where meaningful knowledge—the kinetics of refining as a function of the process variables—can be achieved. Much of the available information on the purification of Nb has been obtained by empirical methods.

The high-melting point of Nb (approx. 2473°C), together with its reactive characteristics, makes difficult the utilization of conventional experimental techniques for obtaining reliable information on the purification characteristics of impurities under controlled conditions.

Levitation melting, on the other hand, is a well-established technique.[3] It has been used in studying oxidation and carburization,[4-7] solidification,[8,9] and grain refining[10] of several alloy systems. This technique's inherent advantages include non-contamination due to its containerless feature, melt homogeneity due to effective magnetic stirring, precise temperature, time and atmospheric control during melting and melt holding. Although this technique has been known for some time, recent interest in materials

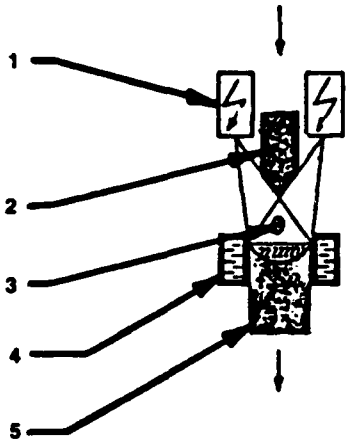

Figure 1 (a). Typical Arrangement for Drip Melting Used in EB Melting Unit.

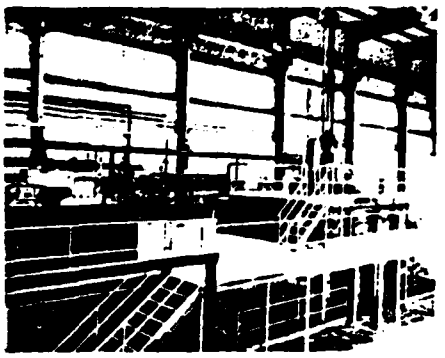

Figure 1 (b). A Commercial 1200-kW EB Melting Furnace Used at KBI—a Division of Cabot Corporation.

processing in space (low-gravity conditions) has rekindled several efforts to study refining and solidification characteristics in highly controlled and pure ambient conditions.

In this study, the levitation melting technique was employed in examining the refining behavior of Nb. The starting material used was impure niobium in the form of Nb-thermite produced by aluminothermic reduction of Nb_2O_5. Similar input charge is used in producing commercial-grade niobium by EB refining. A typical chemical analysis of the thermite is compared with commercial purity Nb in Table I. Note that the refining operation has improved the purity of the thermite from 93-95% to 99.96 w/o.

Table I: Analysis of Niobium

Element	Thermite (Typical)	EB Melting (Typical)	Levitation Melting 1 min.	Levitation Melting 7 min.
Al	3.6-4.3 wt.%	<10 ppm	NA	NA
B	30-80 ppm	<10 ppm		
C	700-800 ppm	<25 ppm	659	415
Cr	200-700 ppm	<10 ppm		
Fe	1000-4000 ppm	<10 ppm		
N	500-900 ppm	5-30 ppm	539	507
O	4000-5000 ppm	50-100 ppm	895	591
Si	700-1000 ppm	<10 ppm		
Sr	10-15 ppm	<10 ppm		
Ta	300-1200 ppm	<500 ppm		
Ti	10-20 ppm	<10 ppm		
W	100-200 ppm	<100 ppm		
Zr	<10 ppm	<10 ppm		
Nb	93.0-95.0 wt%	99.0-99.6 wt%		

EXPERIMENTAL PROCEDURE

The schematic of the levitation melting apparatus and the experimental setup with the levitation coil and the specimen-holding chamber are shown in Figure 2. The levitation coil incorporates two reverse-wound water-cooled copper coils. The lower coil is double-wound and slightly conical in shape, measuring about 16-mm inner diameter at the bottom winding of the cone. The gap between the upper and lower coil is about 5-mm and can be varied according to sample weight and geometry.

The sample chamber consists of a glass tube open at both ends and connected to a gas delivery system to allow control flow of high-purity argon. The argon was purified with a gas purifier utilizing titanium chips at 800°C as a "getter". The oxygen content of the purified gas was continuously monitored using a solid-state electrolyte and determined to be 10^{-15} ppm.

The thermite samples, weighing approximately 1 gm, were lowered into the levitation coil using a sample positioner. The sample positioner was removed from the electromagnetic field as soon as the solid sample was levitated. Each sample was melted under a continuous flow of argon at a partial pressure of 13.0 Pa and was held for a specific residence time. The temperature of the sample was monitored using a two-color pyrometer. After a specific holding time, the power to the coil was turned off and the liquid sample dropped onto a copper chill placed immediately below the levitation coil. The droplets, after solidification, took the shape of a round splat with a thickness of approximately 2-3 mm at the center.

RESULTS AND DISCUSSIONS

The microstructure of the initial Nb-thermite sample is shown in Figure 3. The elemental distribution within the matrix is more clearly seen from the X-ray maps shown in Figure 4. The microstructure of the Nb-thermite consists of a niobium-aluminum solid solution phase containing small amounts of iron and carbon, Al_2O_3 and Nb_2C inclusions.

The microstructures of two levitation-melted samples, held for 1 and 6 minutes of the melt residence time in liquid state, are shown in Figure 5. The corresponding X-ray energy dispersive spectra for these two residence times are shown in Figure 6. It is significant to note that considerable microstructural refinement has occurred even after one minute of the melt residence time. The heavy dendritic coring (solute segregation) seen in the starting material, Figure 3, has been reduced considerably, as revealed by the etched microstructures. The etchant used, consisting of 10% HNO_3,

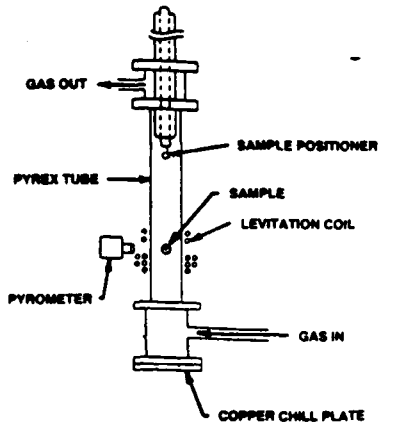

(a)

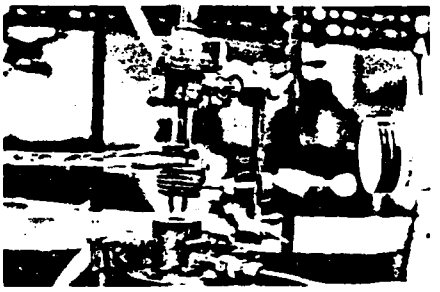

(b)

Figure 2. Levitation Melting Apparatus: (a) the schematic of the experimental setup; and (b) double-wound induction coil.

(a)

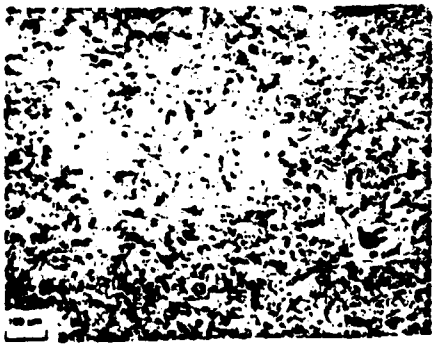

(b)

Figure 3. Photomicrographs of niobium thermite produce by Aluminothermic Reduction of Nb_2O_5 at (a) 500X, and (b) 100X.

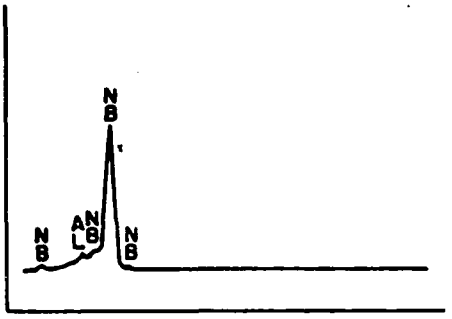

(a)

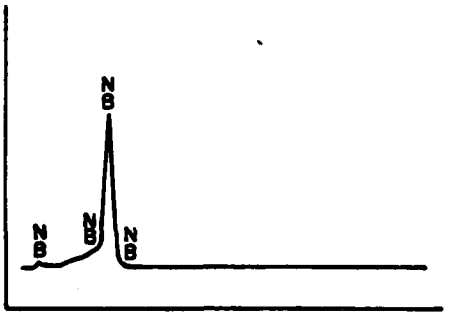

(b)

Figure 6. The x-ray energy spectra of niobium matrix with melt residence time of a (a) one minute, and (b) six minutes.

15% H_2SO_4, and 20% HF solution (balance H_2O), is especially sensitive to the compositional variations within Nb matrix. The X-ray energy spectra, Figure 6a, indicates the presence of some residual amount of aluminum in samples with one minute of the melt residence time. The residual aluminum had completely disappeared after 6 minutes of levitation, as evidenced by the X-ray spectra of Figure 6b, and by the absence of etching contrast in the microstructure, Figure 5d. Longer residence times, up to ten minutes, showed no measurable changes in microstructural features. It should be noted that the photomicrographs of the samples with 1 and 6 minutes of levitation, at higher magnifications (Figures 5b and 5d), exhibit some dark spots resembling second-phase particles. The spots are actually etch pits produced during electropolishing, as confirmed by SEM examination.

Examination of microstructures in Figures 3a, 5a, and 5c, indicates a gradual coarsening of dendritic structures associated with the refinement. This effect is particularly more pronounced in the zones near the metal-copper chill contact, as shown in Figures 5a and 5c. The columnar region (A) corresponds to the zone near the chill substrate contact where a relatively higher thermal gradient and hence higher cooling rate existed during solidification. The equiaxed region (B) corresponds to regions close to the free surface of the sample where a relatively lower thermal gradient and slower cooling rate existed. The removal of interstitual elements such as O, C, N, and H, in addition to the removal of Al and Fe, contributes to grain coarsening. This tendency is typical during solidification of pure materials, where the lack of constitutional supercooling effects and grain growth inhibitors promote the growth of larger crystals. This is one reason why pure metals exhibit larger grain sizes compared to alloys. Accordingly, the coarsening of the microstructure can be used as a qualitative measure of the degree of refinement that has taken place.

The chemical purity of the refractory metals is often monitored through the hardness measurements of the material. At small concentrations, the hardness is directly proportional to the total concentration of interstitial elements, such as O, N, C, and H. Thus, the hardness of the material provides an easily measurable parameter for assessing the overall purity. The variation in microhardness, measured on polished specimens, as a

Figure 4. Constituent phases in niobium thermite: (a) scanning electron micrograph; and x-ray topographical maps of (b) aluminum, (c) niobium, (d) oxygen, (e) carbon, and (f) iron.

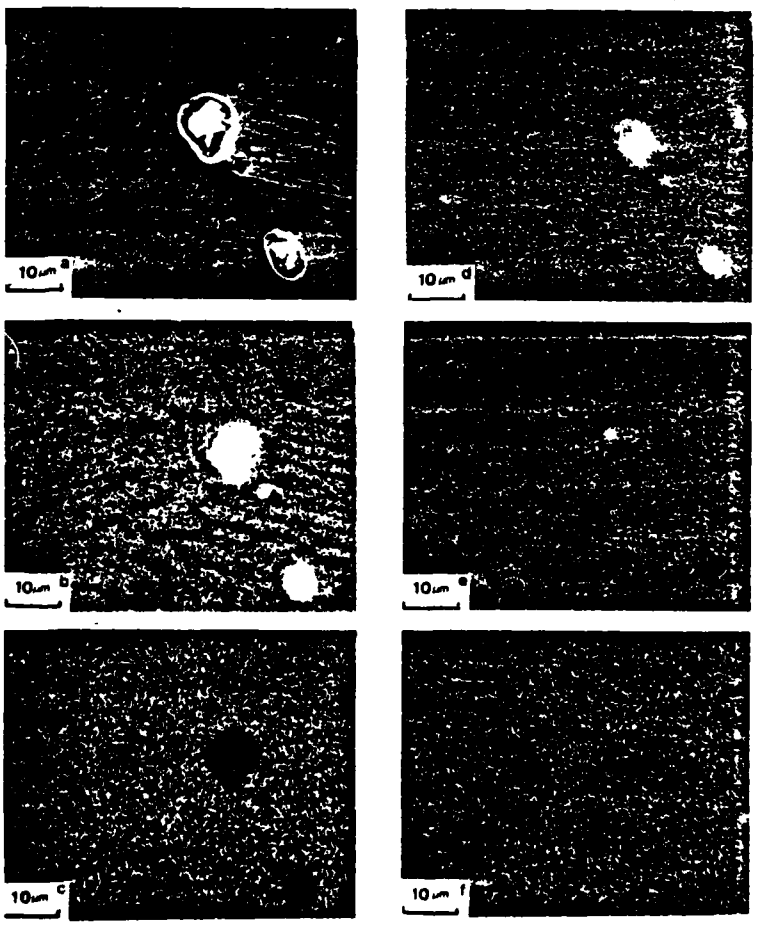

function the melt residence time is plotted in Figure 7. Also included in the plot is the typical microhardness of the commercial purity niobium produced by EB melting. Note that the microhardness has gradually decreased with the melt residence time, but levels off after about 300 seconds. This is further corroborated by the variation in the interstitial content (C+N+O) of the samples with various melt residence times, as shown in Figure 8.

During the initial stages of levitation melting, a white fume evolved from the sample at approximately 1800°C, which condensed onto the chamber walls. The initial melting of the sample took place around 2060°C, and the sample was completely molten by 2100°C. The emission of white fume ceased after about 4 minutes of holding time. The powdered deposit was collected and analyzed using X-ray diffraction technique in few cases. The analysis of the resulting diffraction pattern showed definite presence of Al_2O_3, NbN, Al, and Fe. Additional diffraction lines were also present which could not be indexed. It should be noted that no niobium oxide was detected in the deposit. The visual observations, coupled with the microstructural changes and the chemical analysis of the sample, indicate that the bulk of the thermite is purified in early stages of levitation up to 5 minutes, beyond which the rate of purification slows down. This suggests that the present levitation system can be safely employed to achieve only limited purification. A major difference between the EB melting and the present levitation experiments is that the refining takes place in a vacuum (0.1 Pa) in the former process, whereas, the refining in the latter process was in a continuous flow of argon gas. Another difference between the processes is the refining temperature. The temperature of the levitation melted samples was estimated to be in the range of 2000-2500°C during the course of the experiments. On the other hand, the temperature achieved during electron beam melting is believed to be in the range of 2800-3000°C. The difference in refining temperatures could account for the rapid purification rates observed during EB melting. The kinetics of the purification process are extremely complex regardless of electron beam or levitation melting techniques employed. The overall refining process, assuming no chemical reaction, consists of a number of elemental steps. These include the dissolution of inclusions, mass transport to the surface, the disorption

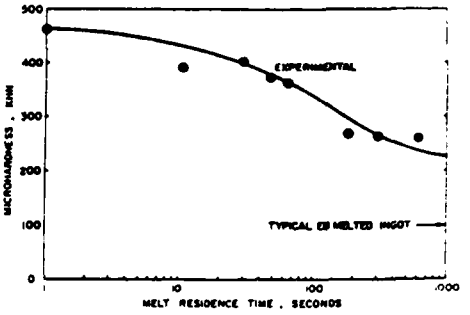

Figure 7. The variation of microhardness as a function of melt residence time.

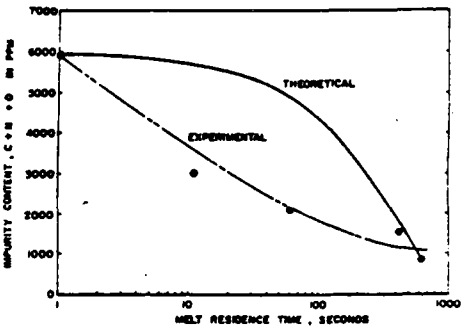

Figure 8. Change in the total impurity content (C+N+H) of niobium as a function of melt residence time.

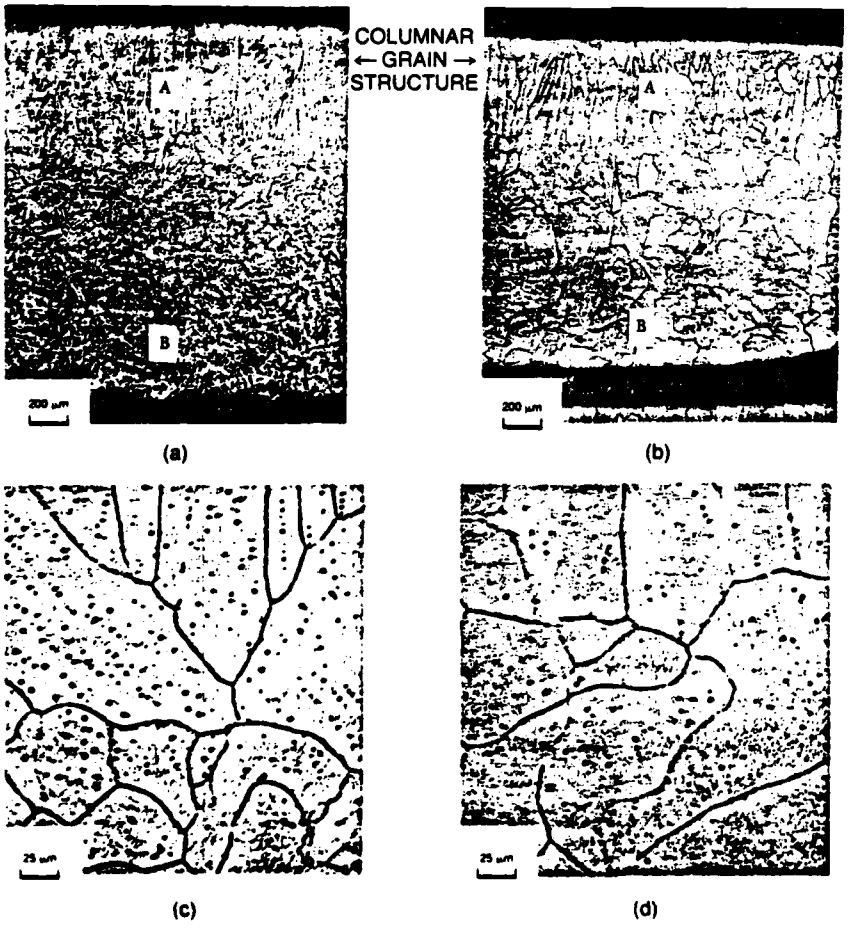

Figure 5. Photomicrographs of levitation melted niobium with melt residence time of one minute (a) 50X magnification, (b) 400X magnification, and with melt residence time of six minutes at (c) 50X magnification, and (d) 400X magnification.

If you want more information on this subject, please circle reader service card number 50.

ABOUT THE AUTHORS

Dr. Y. V. Murty received his Ph.D. from the University of Connecticut. He is currently Manager, Process Development Section, at Cabot's Engineered Products Technology Laboratories in Reading, Pennsylvania. Dr. Murty is also a member of TMS-AIME.

Dr. **Dayanand S. Shahapurkar** received his Ph.D. from Pennsylvania State University, University Park, Pennsylvania. He is currently a Senior Research Engineer at Cabot's Engineered Products Technology Laboratories in Reading, Pennsylvania. Dr. Shahapurkar is also a member of TMS-AIME.

Riad I. Asfahani received his M.S. in Metallurgical Engineering from the University of Notre Dame. He is currently a research engineer at Cabot's Engineered Products Technology Laboratories in Reading, Pennsylvania. Mr. Asfahani is also a member of TMS-AIME.

Dr. G. J. (Reza) Abbaschian received his Ph.D. in Materials Science and Engineering from the University of California, Berkeley in 1971. He is currently a professor of Metals Processing in the Materials Science and Engineering Department of the University of Florida.

Joseph A. Patchett received his M.S. in Metals Processing from the University of Florida in 1984. He is currently a Ph.D. candidate in the Materials Science and Engineering Department of the University of Florida.

of the molecular species from the surface, and the subsequent mass transfer through the vapor boundary layer surrounding the sample. It is also apparent from our work that the assumption of the absence of chemical reactions is incorrect. This introduces still further complications in determining the overall kinetics, and the large thermal gradient surrounding the sample complicates the problem further still. Nevertheless, in an effort to determine the kinetics of the refinement during levitation, the interstitial elemental concentrations can be estimated using the following equations:[11,12]

For oxygen,

(a) $\text{Log}(C_t/C_o) = -(F/M) \times t \times 5.87 \times 10^{10} \times \text{EXP}(-6.53 \times 10^4/T)$

For nitrogen,

(b) $\text{Log}(C_o/C_t) = 1+(F/M)C_o \times t \times 5.55 \times 10^{13} \times \text{EXP}(-6.25 \times 10^4/T)$

where C_o is initial concentration (grams/grams of samples), C_t is momentary concentration at time t, F is the surface area in cm^2, M is the mass of sample in grams, t is the time in minutes, and T is the absolute temperature in K. In Nb-O system, deoxidation can occur by volatalization of suboxides or desorption of elemental oxygen. These reactions take place concurrently with the volatilization of the base metal itself. Considering the kinetics of these reactions, it has been established that volatilization of the suboxides predominates in the removal of oxygen, which has been the basis for the rate equation for deoxidation. The equation describing the kinetics of denitrogenization has been derived assuming equilibrium conditions between gaseous phase (pure N_2) and the condensed phase (N_2 dissolved in Nb). The decarburization of Nb is considered to be due to the chemical reaction between oxygen and dissolved carbon forming carbon monoxide with kinetics similar to that of oxygen evolution.

The calculated concentration levels of the interstitial elements, viz., C, N, and O are compared with the experimental data of Table I in Figure 8. The calculated individual elemental concentration levels compare well with those of nitrogen and carbon with the exception of oxygen. As mentioned above, the deoxidation has been assumed to take place due to volatilization of suboxides, rather than desorption of elemental oxygen.

The usefulness of the levitation melting technique has been clearly demonstrated in studying the purification behavior of a high-melting point of material such as niobium. This technique can be used to study and understand the kinetics of purification of other refractory metals as well.

ACKNOWLEDGEMENTS

Two of the authors (J. A. Patchett and G. J. Abbaschian) would like to acknowledge partial support of this research by the Office of Naval Research, Contract Number N0-N00014-E1-K-0730.

References

1. R. Bakish, Editor, "Proceedings of the Conference on Electron Beam Melting and Refining—State-of-the-Art 1983", Reno, Nevada, November 6-8, 1983, published by Bakish Materials Corporation.
2. W. G. Pfann, "Principles of Zone Melting", *Trans. AIME*, Vol. 194, 1932, p. 747.
3. W. A. Peifer, *Journal of Metals*, Vol. 17, May 1965, pp. 487-493.
4. R. T. Begley, G. Comenetz, P. A. Flim, and J. W. Salatka, *Rev. Science Instr.*, 1959, Vol. 30, p. 38.
5. A. A. Fogel, T. A. Sidorova, V. V Simirnov, Z. A. Guts, and I. V. Korkin, "Optimum Parameters for Apparatus for Levitation Melting of Metals", *Russian Metallurgy*, (4), 1968, pp. 89-95.
6. L. A. Baker and R. G. Ward, *Journal of the Iron and Steel Institute*, Vol. 205, July 1967, pp. 714-717.
7. L. A. Baker, N. A. Warner, and A. E. Jenking, *Trans. Met. Soc. AIME*, Vol. 239, June 1967, pp. 857-864.
8. D. D McDevitt and G. J. Abbaschian, *Microstructural Science*, Vol. 11, 1983, p. 125.
9. Y. V. Murty, T. Z. Kattamis, and J. A. Reffner, *Journal of Crystal Growth*, Vol. 19, 1973, pp. 237-241.
10. G. E. Amaya, J. A. Patchett, and G. J. Abbaschian, In, "Grain Refinement in Castings and Welds", Ed. G J. Abbaschian and S. A. David. *Cont. Prof. Met. Soc. AIME*, October 1982, pp. 51-65.
11. Gerhard Horz, "Mechanisms and Kinetics of Absorption and Desorption Reactions in Systems of Refractory Metals with Nitrogen, Oxygen, and Carbon", *Met. Trans.*, Vol. 3, December 1972, pp. 3059-3076.
12. D. G. Pinatti, R. A. Conti, C. Takano, "Modified Electron Beam Refining Process for Niobium", XXXVI Annual Congress of the Brazilian Association of Metals—ABM), Recife, July 1981.

END

FILMED

2-86

DTIC